THE ω HADRONIZATION STUDIES IN THE NUCLEAR MEDIUM WITH THE CLAS SPECTROMETER

ANDRÉS BÓRQUEZ CÁRCAMO

MASTER THESIS

UNIVERSIDAD TÉCNICA FEDERICO SANTA MARÍA
DEPARTAMENTO DE FÍSICA

MAY 21, 2021

Andrés Bórquez Cárcamo: *The ω Hadronization Studies in the Nuclear Medium with the CLAS Spectrometer,* Master Thesis. May 21, 2021.

APPROVAL PAGE

Título de Tesis:

THE ω HADRONIZATION STUDIES IN THE NUCLEAR MEDIUM WITH THE CLAS SPECTROMETER

Autor:

ANDRÉS BÓRQUEZ CÁRCAMO

Trabajo de tesis presentado en cumplimiento parcial de los requisitos para el grado de Magister en Ciencias, mención Física, de la Universidad Técnica Federico Santa María.

Profesor Guía: _____

Hayk Hakobyan
(UTFSM, Chile)

Profesor Correferente: _____

Michael H. Wood
(Canisius College, EE.UU.)

Profesor Correferente: _____

Taisiya Mineeva
(UTFSM, Chile)

Valparaíso, Chile
May 21, 2021

Dedicated to my family.

ABSTRACT

A complete picture of the strong interaction must include hadronization, the dynamical process of a free quark forming a color-neutral hadron. To study the hadronization of the vector meson $\omega(782)$, we perform semi-inclusive deep-inelastic scattering measurements on deuterium, carbon, iron, and lead using data collected with the CLAS detector at Jefferson Lab employing a 5.014 GeV electron beam. To examine nuclear dependence on the hadron formation, we present ω multiplicities of the solid targets relative to those on deuterium as one-dimensional functions of the virtual-photon energy ν, the photon virtuality Q^2, the fractional hadron energy z_h, and the square of the hadron transverse momentum p_T^2. This analysis corresponds to the world's first hadronization studies of the ω meson and hints at a promising future for upcoming CLAS12 and EIC experiments, where more detailed investigations could be achieved.

RESUMEN

Un cuadro completo de la interacción fuerte debe incluir la hadronización, el proceso dinámico en el que un quark libre se transforma en un hadrón de color neutro. Para estudiar la hadronización del mesón vectorial $\omega(782)$, se realizan mediciones bajo el régimen llamado Semi-Inclusive Deep Inelastic Scattering en deuterio, carbono, hierro y plomo usando datos medidos por el detector CLAS en Jefferson Lab, empleando un haz de electrones de 5.014 GeV. Para examinar la dependencia nuclear en la formación del hadrón, presentamos multiplicidades de los blancos sólidos relativos a los del deuterio como funciones unidimensionales de la energía de los fotones virtuales ν, la virtualidad de los fotones Q^2, la energía fraccionaria del hadrón z_h y el cuadrado del momento transversal del hadrón p_T^2. Este análisis corresponde a los primeros estudios de hadronización del mesón ω en el mundo y da indicio de un futuro prometedor para los próximos experimentos de CLAS12 y EIC, donde se podrían lograr investigaciones más detalladas.

ACKNOWLEDGMENTS

The present work would not be possible without the help of outstanding people I was fortunate to meet. To begin with, I would like to thank Hayk: a brilliant scientist, but more importantly, a person with a big heart. I will be eternally grateful to him for inviting me to the experimental nuclear physics group of the university and for having unlimited energy to guide and support me whenever I needed it.

Although I have never met him in person, Mike has been an enormous source of inspiration due to his endless patience, goodwill, and kindness. I am very thankful to him for sharing exciting conversations and valuable insights about physics. I really hope that someday we can finally meet.

I would also like to return all the kind words I have received from Taya. I really admire her excellent work as a hostess in the countless meetings we have had. For her knowledge, her honesty, her trust, and for sharing with me all those little data analysis details that only experience can give.

I am also grateful to the group leader and excellent professor, Will, for welcoming and supporting every one of us, the students, always answering in the most clever way all the questions we may have. I admire him very much for sharing his immense knowledge and experience with us, not only in physics but also in how a professional scientist should work.

One of the people who laid the foundation for this analysis is Orlando S. He has been there since the beginning of this project and provided me with the necessary tools to develop the data analysis and solve any error I might find. From which I treasure all the discussions about programming and physics we have had.

At a later stage, I met Miguel A., who helped me to clarify my ideas to finish this project. And I also met Jorge L., who has taught me a lot about software development and version control. I am especially grateful to him for seeing potential in me and assisting me selflessly in the following path of my life, the doctorate.

I want to dedicate a paragraph to all the friends I have made along the way. Thanks to my roommates Benjamin H., Jeffries M., and Sergio S., with who I had the good fortune to live countless mornings, afternoons, and evenings of conversations, movies, music, and gatherings in the legendary apartment 507. I also want to thank the unparalleled Esteban M., "El Tata," who is like a brother to me and has always been in my highs and lows. To Antonio R., for his always pleasant company and for having survived with me that school we don't want to remember. To Sebastián M., for being an expert in cutting all kinds of grass. To David K., "The Experiment", to

whom I taught everything I know of tennis and who gave me a beautiful friendship in return.

I am very thankful to my family for all the support and unconditional love they have given me. Although I never call them by their names, I want to thank my dad Ramón, my mom Jeanette and my sister Dani. Despite the distance, they continue to believe in me, and despite the time, they always welcome me with open arms and fire lit on the stove every time I return home.

I want to dedicate a special paragraph to Coni, my new family, *my constant*. Thank you very much for coming to live and survive with me in these crazy times, where we have learned to take care of each other. Sincerely, without your support and cheering, this thesis would have taken so much longer to finish. Thank you so much for being my partner during all these beautiful years we have been together, and hopefully, many more, because everything I do is more fun if you are by my side.

The truth is that sometimes words are not enough to express the gratitude I feel to each and every one of the people I mentioned. Thank you for having accompanied me on this adventure, and I hope we will continue to meet again.

Look at me: still talking when there's science to do.

— Jonathan Coulton, "Still Alive"

CONTENTS

The whole material world seems to me like a newspaper headline
It explicitly demands your attention
And it may even contain some truth
But what's really going on here?

— mewithoutYou, "Wolf Am I! (and Shadow)"

1 INTRODUCTION

Particle physics, also known as High-Energy Physics (HEP), is the branch of physics that studies the most fundamental components of matter and their interactions. The current paradigm that explains the fundamental forces that govern the universe is the Standard Model of Particle Physics. This framework encapsulates the electromagnetic, weak, and strong interactions—being its latest and most notable achievement the prediction (in 1964 [1]) and subsequent discovery of the Higgs boson (in 2012 [2, 3]).

In the Standard Model, Quantum Chromodynamics (QCD) corresponds to the theory that describes the strong nuclear interaction in charge of binding protons and neutrons inside the atomic nucleus and binding its constituents, the *quarks*, through *gluons* that act as force-mediating gauge *bosons*. Any particle that is made up of quarks is called a *hadron*. And within the hadrons, two categories are distinguished: *baryons*, formed by three quarks, and *mesons*, formed by a quark-antiquark pair.

However, there are still some missing pieces to be explained to achieve a complete picture of the strong interaction. One of them is *confinement*, which states that color-charged particles, such as quarks and gluons, cannot be observed when isolated. This phenomenon is directly related to *hadronization*, the dynamical process of a free quark forming a color-neutral hadron. Several theoretical models have been proposed and diverse experiments have been performed to examine both phenomena. One of the most widely used experimental techniques is Deep-Inelastic Scattering (DIS), which consists of lepton-nucleon interactions to probe the nucleons' internal structure. Historically, this method provided the first experimental evidence for the existence of quarks.

To determine important information on the characteristic time-distance scales of hadronization, one can study the produced particles emerging from DIS on a diverse range of nuclei. Several HEP collaborations, such as SLAC [4], EMC [5], and Fermilab [6], performed these kinds of studies, observing that the hadron production depends on the nuclear size of the targets and certain kinematical variables. Later, the HERMES Collaboration would refine the method with more luminosity and an improved hadron separation, leading to the publication of various articles during the last two decades [7–11].

To measure the effect of different nuclear environments on the hadronization, the CLAS Collaboration [12] designed, built, and performed the EG2 experiment [13]. A double-target DIS experiment with an incident 5 GeV

electron beam colliding simultaneously with a liquid deuterium target and a solid nuclear target. The statistical analysis of the data collected by this experiment led to studies on the hadronization of neutral kaons [14], charged pions [15–18], neutral pions [19, 20], and the η meson [21].

To continue the research program of the EG2 experiment, the purpose of this work is to analyze the hadronization of the $\omega(782)$ meson [22] reconstructed through its $\pi^+\pi^-\pi^0$ decay channel. This analysis reports the ω Multiplicity Ratios for targets of carbon, iron, and lead relative to deuterium as a function of the scattered electron variables, Q^2 and ν, and the hadron variables, z_h and p_T^2. Although the most significant difficulty is the low statistics and signal-to-noise ratio, this analysis corresponds to the world's first study of the ω meson's hadronization.

This thesis is structured as follows. After this introduction, Chapter 2 elaborates a comprehensive overview of the advancements to this day on hadronization, both theoretical and experimental. Chapter 3 outlines the experimental apparatus used to produce, detect, measure and collect the physical events. A complete and sequential explanation of the data analysis is given in Chapter 4. The generation and reconstruction of Monte Carlo simulations are described in Chapter 5, where the Acceptance Corrections are detailed. Finally, this thesis concludes with the ω Multiplicity Ratio results, along with a brief discussion and an outlook on future experiments in Chapter 6.

2

PHYSICS MOTIVATION

This chapter is a review of the theoretical and experimental advancements for which the present analysis is motivated. Section 2.1 explains the notation and conventions used to write this document. Section 2.2 narrates a brief history of particle physics, which continues at Section 2.3 with the Eightfold Way and Section 2.4 with the Quark Model. Then, the next sections establish the necessary formalism: Section 2.5 explains the Elastic Scattering, Section 2.6 details the Deep-Inelastic Scattering, Section 2.7 explains the Quark-Parton Model, and Section 2.8 summarizes the properties of Quantum Chromodynamics. Section 2.9 defines the process of hadronization and some phenomenological models, and Section 2.10 defines the experimental observable of interest, the Multiplicity Ratio. Finally, Section 2.11 highlights some hadronization studies published by previous collaborations, and Section 2.12 elaborates on the importance of the $\omega(782)$ meson.

2.1 NOTATION AND CONVENTIONS

This document will make use of *Natural Units*, except where stated otherwise, i.e.,

$$\hbar = 1, \quad c = 1. \tag{2.1}$$

The metric to use is the flat space metric, or *Minkowski Metric*, following the particle physicist's convention $(+,-,-,-)$, also called the *mostly minus metric*:

$$\eta^{\mu\nu} = \begin{pmatrix} 1 & 0 & 0 & 0 \\ 0 & -1 & 0 & 0 \\ 0 & 0 & -1 & 0 \\ 0 & 0 & 0 & -1 \end{pmatrix}. \tag{2.2}$$

This sign convention is useful to treat relevant *timelike* quantities, such as mass and energy, as positive numbers.

2.2 A BRIEF HISTORY OF PARTICLE PHYSICS

What is the world made of? This enigma started, as it often happens, as a philosophical question. The first record of answering it leads to Greece, with the natural philosophers and Aristotle, who believed that four

classical elements compose everything in nature: earth, air, fire, and water. Later, circa 460–370 BC, Greek philosophers Leucippus and Democritus proposed that matter was formed by extremely small, invisible, indivisible, and eternal constituents called atoms. A word that comes from the ancient Greek *atomos*, which means uncuttable.

It was not until the end of the 18^{th} century that J. Dalton converted the atomist theory into a scientific theory rather than a philosophical one. Dalton's atomism postulated that the atoms were indivisible particles. However, in 1897, J. J. Thomson concluded the contrary upon the discovery of a negatively-charged particle smaller than a hydrogen atom. These subatomic particles would be later baptized as *electrons*.

Thomson suggested that the electrons were embedded on a positively-charged region like raisins in a plum pudding. This model would be later disproved in 1911 by E. Rutherford, who, based on experimental results, concluded that most of the atom is empty and most of the mass corresponds to a positively-charged condensed region called the *nucleus*, that is surrounded by orbiting electrons. A scheme of the Rutherford experiment is given by Fig. 2.1.

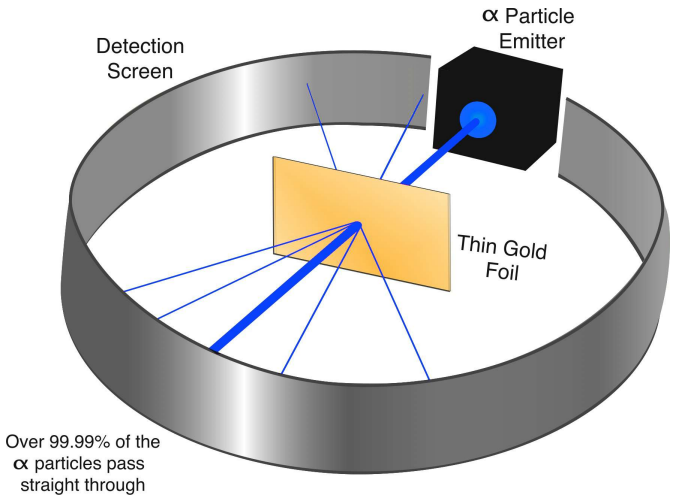

Figure 2.1: Illustration of the Rutherford experiment.

Nevertheless, science is characterized by its constant evolution, and over the course of the 20th century, many corrections and developments were achieved. Classical mechanics and electromagnetism proved successful in the macroscopic realm, but many phenomena could not be explained in the microscopic world. In this context, revolutionary ideas appeared, such as the wave-particle duality, the quantization of light, and the discretization of energy levels. Together with new mathematical formalisms, these ideas would become the foundations of a new physics capable of predicting

phenomena at the atomic and subatomic levels. It was the birth of quantum mechanics.

But quantum mechanics was still incompatible with the theory of special relativity, published by Einstein in 1905. In an attempt to solve this, P. Dirac proposed a pioneering equation that would be later completed as the most accurate physics theory in history: Quantum Electrodynamics (QED), which fully describes the interactions between light and matter.

Near the same time, several experiments led to the discovery of new particles, such as neutrons, positrons, muons, pions, and kaons. These advances were drastically accelerated in the 1950s, with the flourishing of particle physics, which sought to describe the most fundamental components of matter and their interactions. Higher energies were necessary, and they were achieved by constructing particle accelerators and cosmic rays studies, where new experiments led to discovering a bewildering variety of particles, which would be referred to as the *particle zoo*. And just like the periodic table of the elements has a substructure, it became evident that smaller constituents must exist. These fundamental particles would later be called *quarks*.

At present, the most successful theory in explaining the fundamental forces that govern the universe is the Standard Model. Leaving gravitation aside, this framework includes electromagnetic, weak, and strong interactions. Its latest and most notable achievement was the prediction (in 1964, [1]) and subsequent discovery of the Higgs boson (in 2012, [2, 3]).

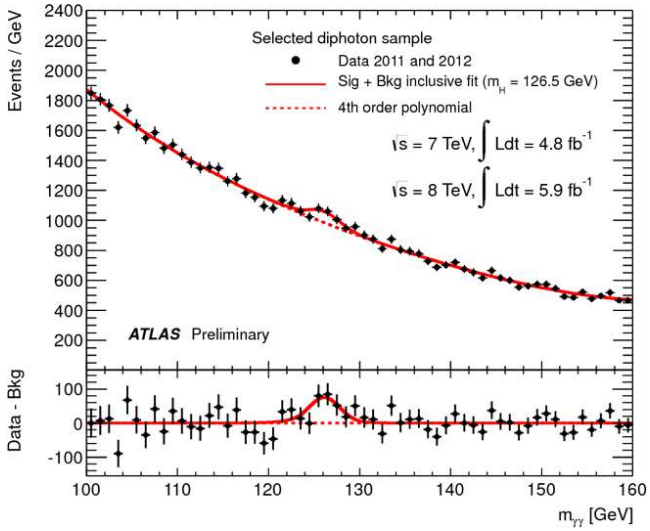

Figure 2.2: Invariant mass distribution from pairs of photons selected in the $H \to \gamma\gamma$ analysis, as shown at Ref. [2]. The excess of events over the background prediction around 125 GeV is consistent with predictions for the Standard Model Higgs boson. Results obtained by the A Toroidal LHC Apparatus (ATLAS) Collaboration at CERN.

2.3 THE EIGHTFOLD WAY

The newly discovered pions and kaons had large masses, were produced in pairs with large cross sections, and had lifetimes too large to be nuclear resonances. Furthermore, they were produced by strong interactions and decayed by weak interactions. It was necessary to establish rules for classifying them.

In the 1960s, M. Gell-Mann[1] proposed the eightfold way[2]. Under the definition and proposal of new quantum numbers, such as strangeness S, baryonic number B, and hypercharge $Y = B + S$, they observed that groups of particles were related in a way that matched the representations of the $SU(3)$ symmetry. As shown in Fig. 2.3 and considering the proposed quantum numbers, mesons and spin 1/2 baryons can be organized as octets.

Physicists accepted this model for a long time. It was even able to predict a new particle. Following the theory, the baryons with spin 3/2 should be represented by a multiplet of ten elements, or decuplet. So far nine had been discovered, and the missing particle had to appear in a certain decay and had a specific range of mass. In 1964, that particle with $S = -3$ was discovered and was named Ω^- [23].

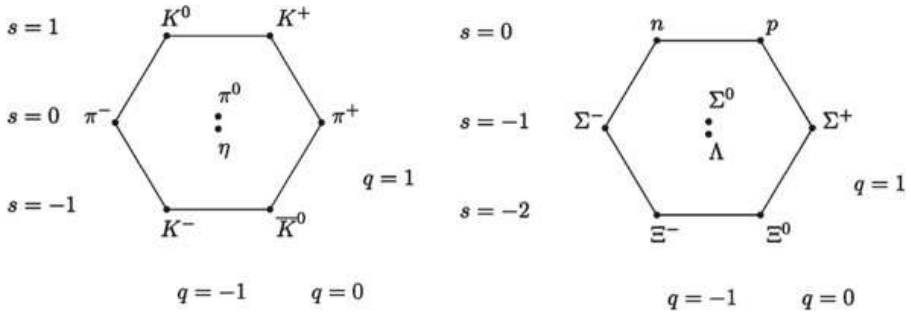

Figure 2.3: The eightfold way organizes both groups of mesons with spin 0 (left panel) and baryons with parity 1 and spin 1/2 (right panel) into octets. Diagrams taken from Ref. [24].

2.4 THE QUARK MODEL

Because of the eightfold way, the multiplets of mesons and baryons were interpreted as representations of the $SU(3)$ group symmetry. However, it seemed that these results could be achieved by combining even more fundamental representations. Because of this, in 1964, M. Gell-Mann and G. Zweig proposed a triplet of spin 1/2 particles with fractional electric

1 Independently of Y. Ne'eman and A. Petermann.
2 Name inspired by the Noble Eightfold Path of Buddhism.

charge and baryonic number called *quarks* and its conjugate representation of *antiquarks*. Three different states or flavors of quarks were proposed: *up* u, *down* d, and *strange* s. *Mesons* are quark-antiquark bound states, while *baryons* are composed of three quarks.

The new formalism proved successful in classifying the particles that had been discovered, except for one. Δ^{++} is a baryon composed of three u quarks, which is a problem because the Pauli exclusion principle states that identical fermions[3] cannot occupy the same quantum state within a quantum system simultaneously. This problem was known as the Δ^{++} puzzle, which implied the existence of a new quantum number: the *color*.

The color, or color-charge, is the QCD equivalent to the electric-charge in QED. There are three colors in QCD, designated as *red*, *blue*, and *green*; with the antiquarks having the respective anticolors. Quarks interact via the emission or absorption of color field bosons[4], the *gluons*. Quarks are single-color states, gluons are bi-colored states, and all observable hadrons are neutral in color. Despite being based on QED, the situation in QCD is more complex because gluons can also interact with themselves.

In 1964, J. Bjorken and S.L. Glashow suggested the existence of a fourth flavor to keep the same symmetry as the four leptons discovered at the time: the electron, the muon, and their respective neutrinos. In 1970, to explain the suppression of some neutral current weak processes, this suggestion became a necessity. In 1974, two experimental groups from the SLAC and the Brookhaven National Laboratory (BNL) simultaneously discovered a heavy resonance; with such a long lifetime, it couldn't be an excited state. This particle was named J/ψ, and it is interpreted as the bound state of a $c\bar{c}$ pair, being c the new quark flavor *charm*. The flavor symmetry group would change from $SU(3)$ to $SU(4)$, giving rise to more complex multiplets or *supermultiplets*, as seen in Fig. 2.4.

In 1977, a fifth quark was discovered by an experiment in Fermilab under the observation of a new heavy and narrow resonance named Υ (upsilon), which was interpreted as the bound state of a $b\bar{b}$ pair, being b the new quark flavor named *bottom*. This time, the lepton sector had five known leptons with the recent discovery of the τ. With the discovery of the bottom quark, the symmetry was restored. The hypothetical sixth quark would be named before its discovery as the *top* quark t, which could be finally discovered in 1995 by the Collider Detector at Fermilab (CDF). This quark is heavier than a gold nucleus; its decay phase space is vast, and its lifetime is so short that it does not live enough to hadronize.

3 Classification of particles that follow Fermi–Dirac statistics and have half odd integer spin, e.g., quarks and leptons.

4 Classification of particles that follow Bose-Einstein statistics and have integer spin, e.g., mesons, gluons and photons.

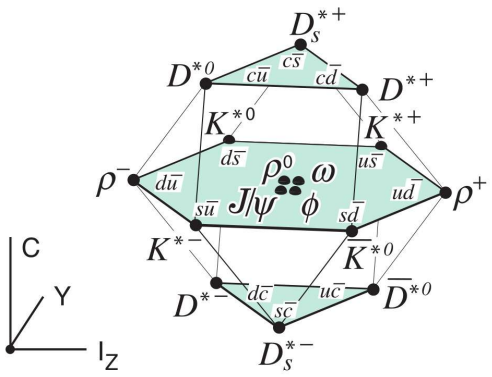

Figure 2.4: Supermultiplet for the vector mesons made of the u, d, s, and c quarks as a function of isospin I_z, hypercharge Y, and charmness C. Diagram taken from Ref. [22].

2.5 ELASTIC SCATTERING

M. Gell-Mann himself stated that quarks seemed to be just mathematical entities. This was true until the development of an experimental method that could demonstrate the existence of quarks: the *deep inelastic scattering*. But first, it is necessary to refer to more basic formulations. As seen in Section 2.2, the Rutherford scattering corresponds to the non-relativistic elastic scattering of a charged particle by a static Coulomb field generated by a fixed point-like particle-in this case, the protons that formed the gold foil. The Rutherford cross section can be expressed as:

$$\left(\frac{d\sigma}{d\Omega}\right)_0 = \frac{\alpha^2}{4E^2 \sin^4(\theta/2)}, \tag{2.3}$$

where θ is the scattering angle, $\alpha = 1/137$ is the QED coupling constant, and E is the energy of the incident particle. If one changes the charged particle to be a relativistic electron with nonzero spin, i.e. non zero magnetic moment, the following derivation can be performed:

$$\left(\frac{d\sigma}{d\Omega}\right)_{\text{Mott}} = \left(\frac{d\sigma}{d\Omega}\right)_0 \left(1 - \beta^2 \sin^2(\theta/2)\right). \tag{2.4}$$

This is known as the Mott cross section, where β is the particle's velocity relative to the speed of light in vacuum. If $\beta \to 0$, the Rutherford cross section is recovered, and if $\beta \to 1$, it becomes

$$\left(\frac{d\sigma}{d\Omega}\right)_{\text{Mott, } \beta\to 1} = \left(\frac{d\sigma}{d\Omega}\right)_0 \cos^2(\theta/2). \tag{2.5}$$

Defining q as the four-momentum transfer between the electron and the target, $q = k_i - k_f$, and $Q^2 \equiv -q^2$, one can now consider that the target is a point-like proton with mass M, spin $1/2$ and that does recoil:

$$\frac{d\sigma}{d\Omega} = \frac{\alpha^2 \cos^2(\theta/2)}{4E_0^2 \sin^4(\theta/2)} \frac{E'}{E} \left[1 + \frac{Q^2}{2M} \tan^2(\theta/2)\right]. \tag{2.6}$$

This is known as the Rosenbluth formula. The first term corresponds to the relativistic Mott cross section defined in Eq. 2.5, the factor E'/E accounts for the energy lost due to the proton's recoil, and the expression between brackets represents the spin-spin interaction. Note that for a fixed electron energy E, this differential cross section depends solely on one electron variable. For convenience, if the scattering angle θ is chosen as the independent variable, the proton's recoil term can be rewritten as:

$$\frac{E'}{E} = \frac{M}{M + E(1 - \cos\theta)}. \tag{2.7}$$

Furthermore, two new Q^2-dependent terms called *Form Factors* G_E and G_M can be added to parameterize the proton structure:

$$\frac{d\sigma}{d\Omega} = \frac{\alpha^2 \cos^2(\theta/2)}{4E_0^2 \sin^4(\theta/2)} \frac{E'}{E} \left[\frac{G_E^2 + \tau G_M^2}{1 + \tau} + 2\tau G_M^2 \tan^2(\theta/2)\right], \tag{2.8}$$

with $\tau \equiv Q^2/4M^2$. The form factors G_E and G_M parametrize our ignorance of the detailed structure of the proton, but appear to be closely related to the proton charge and magnetic moment distributions, respectively[5].

2.6 DEEP-INELASTIC SCATTERING

So far, only elastic interactions have been discussed, where no extra particle is produced. However, one can refine the proton structure's spatial resolution by increasing the energy transfer Q^2 to break it into pieces. This experimental process is denominated Deep-Inelastic Scattering (DIS), and its general expression is:

$$l(k)\, n(p) \to l'(k')\, X, \tag{2.9}$$

where l and l' are the incident and outgoing lepton, respectively, n is the struck nucleon, and X corresponds to the unknown or undetected final hadronic state. The process is a pure electromagnetic interaction, and only charged constituents of the hadron target are probed.

5 In a particular Lorentz frame, called the Breit (or brick wall) frame.

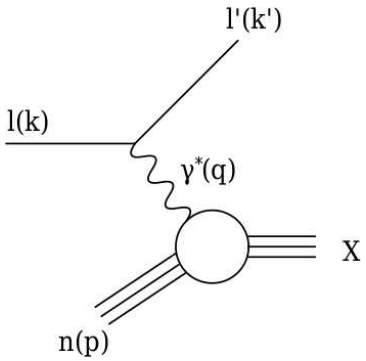

Figure 2.5: Leading-order Feynman diagram describing DIS on a nucleon via virtual photon exchange.

In the laboratory frame of reference, where the initial proton is at rest, its four-momentum is expressed as p:

$$p = (M, 0), \tag{2.10}$$

where $M = 0.938$ GeV is the mass of the proton [22]. On the other hand, the four-momentum for the incident electron k and outgoing electron k' can be written as,

$$k = (E_k, 0, 0, E_k), \quad E_k \gg m_e, \tag{2.11}$$

$$k' = (E'_k, \vec{p}_k), \quad E'_k \gg m_e, \tag{2.12}$$

where E_k is the incident electron's energy and E'_k is the outgoing electron's energy. Therefore, the four-momentum of the virtual photon γ^* would correspond to the energy and momentum exchange of the reaction, and it is denoted by q.

$$q = k - k' = (E_k - E'_k, -p_{ex}, -p_{ey}, E_k - p_{ez}) \tag{2.13}$$

From here, the energy transfer, or the energy of the virtual photon, can be extracted and defined as ν.

$$\nu \equiv \frac{p \cdot q}{M} \overset{lab}{=} E_k - E'_k \tag{2.14}$$

The square of the four-momentum transfer of the electron-proton interaction (or the four-momentum squared of the virtual photon) is Q^2, which can be interpreted as a measure of the virtuality of the probe electron or virtual photon.

$$Q^2 \equiv -q^2 \overset{lab}{=} 2\, E_k\, E'_k\, (1 - \cos\theta)\,, \tag{2.15}$$

where θ is the angle between incident and outgoing electron and $\cos\theta = p_{ez}/E'_k$.

In elastic scattering, the mass of the final hadron state would correspond to M, as the proton target remains intact. However, in DIS, the invariant mass of the final hadronic system can be denoted as W,

$$W^2 \equiv (p+q)^2 \overset{lab}{=} M^2 - Q^2 + 2M\nu. \tag{2.16}$$

A distribution of W at fixed (E, θ) is shown in Fig. 2.6. In the case of elastic scattering where the proton does not break, $W = M$. In the case that the target is excited to resonant baryon states, $M < W < 2$ GeV. And in the case of interest, beyond the resonances region, where multiparticle states appear with large invariant mass, $W > 2$ GeV.

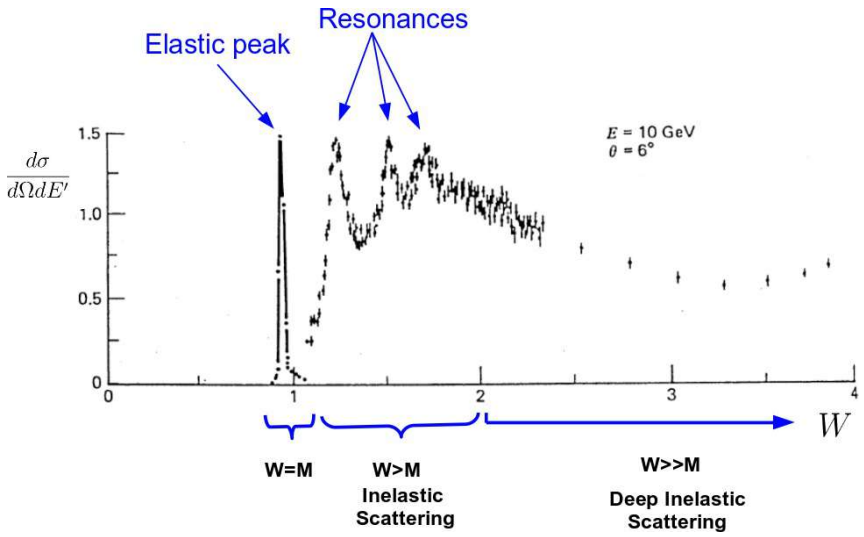

Figure 2.6: DIS differential cross section as a function of the invariant mass of the final hadronic system W (in GeV) at a fixed (E, θ). The elastic peak at $W = M$ has been reduced by a factor of 8.5. Data taken from the SLAC [25].

The inelasticy scaling variable y corresponds to the fractional energy loss of the incident electron.

$$y \equiv \frac{p \cdot q}{p \cdot k} \overset{lab}{=} \frac{\nu}{E_k}, \quad 0 \leq y \leq 1. \tag{2.17}$$

The Bjorken scaling variable x corresponds to the fraction of the proton momentum carried by the struck quark.

$$x \equiv \frac{-q^2}{2p \cdot q} \overset{lab}{=} \frac{Q^2}{2M\nu}, \quad 0 \leq x \leq 1. \tag{2.18}$$

The DIS process can be separated according to the detected products at the final state. Eq. 2.9 represents what is called an Inclusive DIS, because only the scattered lepton is detected. On the contrary, when all the final

products are detected, it is called Exclusive DIS. However, for the case of this work and to extract more information about the quarks and gluons inside the proton than the Inclusive DIS, the framework to study will be the Semi-Inclusive Deep-Inelastic Scattering (SIDIS), where the scattered electron and an extra hadron h is detected in the final state.

The SIDIS reaction can be written as:

$$l(k)\, N(p) \rightarrow l'(k)\, h(p_h)\, X, \tag{2.19}$$

where the four-momentum of the measured hadron h is given by

$$p_h = (E_h, \vec{p}_h). \tag{2.20}$$

This gives rise to the definition of more kinematical variables, such as the hadron fractional energy z_h, defined in the laboratory frame as the energy of the detected hadron divided by ν,

$$z_h \equiv \frac{p \cdot p_h}{p \cdot q} \overset{lab}{=} \frac{E_h}{\nu} \tag{2.21}$$

The direction of the detected hadron with respect to the the virtual photon's direction can be constructed from two angles, the polar angle θ_{PQ},

$$\cos\theta_{PQ} = \frac{\vec{q} \cdot \vec{p}_h}{|\vec{q}||\vec{p}_h|}, \tag{2.22}$$

and the azimuthal angle ϕ_{PQ}, as it's depicted in the Figure 2.7 as the angle between the lepton-scattering plane and the hadron-production plane.

Making use of these angles, one can express the hadron's momentum $\vec{p}_h$ into a transverse and longitudinal component, with respect to the virtual photon,

$$\vec{p}_h{}^2 = \vec{p}_T{}^2 + \vec{p}_L{}^2, \tag{2.23}$$

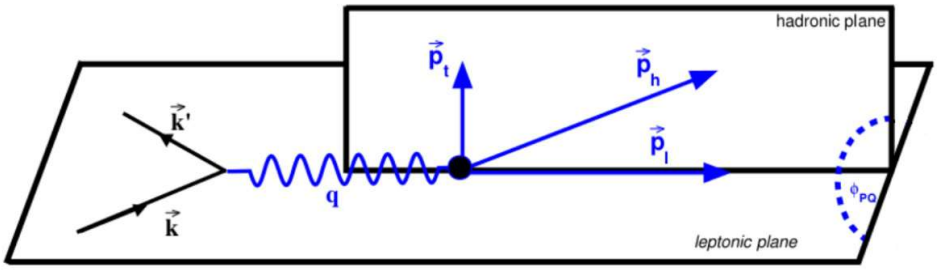

Figure 2.7: Schematic representation of the lepton scattering plane and the hadron production plane in SIDIS in the laboratory frame of reference.

where the explicit expressions of the momentum components can be written as:

$$p_T^2 = |\vec{p}_h|^2(1 - \cos^2\theta_{PQ}), \tag{2.24}$$

$$p_L^2 = |\vec{p}_h|^2 \cos^2\theta_{PQ}. \tag{2.25}$$

Another interesting variable is the missing mass M_x, defined as the invariant mass of the undetected state X.

$$\begin{aligned} M_x^2 &\equiv (q + p - p_h)^2 \\ &\overset{lab}{=} W^2 + m_h^2 - 2\,z_h\,\nu^2 + 2\,p_h\sqrt{\nu^2 + Q^2}\cos\theta_{PQ} \\ &\quad - 2\,M\,z_h\,\nu \end{aligned} \tag{2.26}$$

The differential cross section of the inelastic electron-proton scattering is parameterized, as in the elastic case, with the introduction of two independent functions. These functions, called *structure functions* W_1 and W_2, depend on two degrees of freedom–two of the kinematic variables previously discussed. Choosing Q^2 and ν, it becomes:

$$\frac{d\sigma}{d\Omega} = \left(\frac{d\sigma}{d\Omega}\right)_{\text{Mott}} \frac{E'}{E}\left[W_2(Q^2,\nu) + 2W_1(Q^2,\nu)\tan^2(\theta/2)\right]. \tag{2.27}$$

It can be seen that in the elastic limit, where $x \to 1$ and $2M\nu = Q^2$, these functions must reproduce the elastic cross section.

$$W_1(Q^2,\nu) = \tau G_M^2(Q^2)\delta\left(\nu - \frac{Q^2}{2M}\right), \tag{2.28}$$

$$W_2(Q^2,\nu) = \frac{G_E^2(Q^2) + \tau G_M^2(Q^2)}{1+\tau}\delta\left(\nu - \frac{Q^2}{2M}\right), \tag{2.29}$$

where $\tau = \frac{Q^2}{4M^2}$. Note that if $G_E = G_M = 1$, the Rosenbluth formula of Eq. 2.6 is recovered.

An important property of the structure functions is the *scaling*. To probe the proton substructure, the incident virtual photon must have very small wavelengths ($\lambda \sim 1/\sqrt{Q^2}$), i.e., large Q^2. However, there is a point when increasing the spatial resolution where the structure description no longer depends on the energy of the experiment, but on dimentionless kinematic variables.

A particular case of scaling was proposed in 1967 by J. Bjorken, where he stated that for sufficiently high values of Q^2 and ν, the scaling of the structure functions would be:

$$W_1(Q^2,\nu) \to \frac{1}{M}F_1(w); \quad W_2(Q^2,\nu) \to \frac{1}{\nu}F_2(w), \tag{2.30}$$

where w is the inverse of the x variable:

$$w = \frac{1}{x} = \frac{2M\nu}{Q^2}. \tag{2.31}$$

In other words, at high Q^2 and ν, if one would determine experimentally the value of $F_2(w) = \nu W_2$, it should be independent of Q^2, but dependent on x. This hyphothesis is named *Bjorken Scaling*, and its first experimental proof is represented by Fig. 2.8.

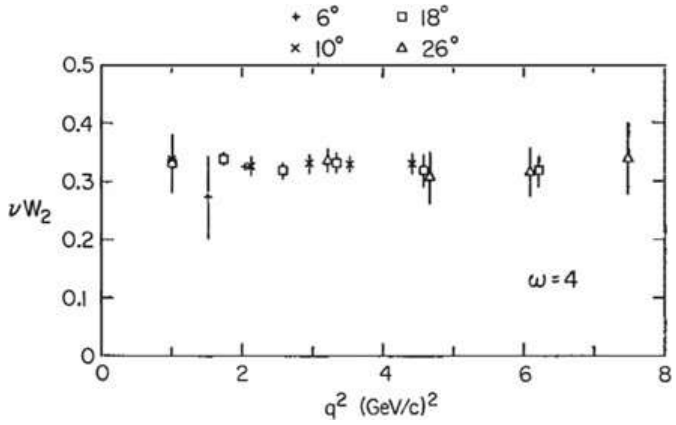

Figure 2.8: The νW_2 scaling for the proton: measurements at fixed x and at different Q^2. Results measured by the SLAC and plot taken from Ref. [25].

2.7 THE QUARK-PARTON MODEL

In 1968, R. Feynman worked out the Quark-Parton Model (QPM) to explain the Bjorken Scaling and the SLAC results. This model states that the inelastic electron-proton scattering at high Q^2 might be seen as the elastic scattering of a lepton into free point-like charged particles in the nucleon, named *partons*[6].

In the QPM, the partons are free inside the hadrons but confined in them. In a first approximation, each parton i may share a fraction x_i of the four-momentum p of the nucleon:

$$p_i = x_i p, \quad \sum_i x_i = 1. \tag{2.32}$$

Each parton must be represented within the structure functions. For this, the probability density function $f_i(x)$ is defined in order to find a parton i with momentum fraction[7] x and charge e_i. After integrating [24], F_1 and F_2 can be expressed as:

$$F_1(Q^2, \nu) = \frac{1}{2} \sum_i e_i^2 f_i(x), \tag{2.33}$$

6 Nowadays, this term is used to denominate all the nucleon constituents: quarks, antiquarks, and gluons.

7 Defined in Eq. 2.18.

$$F_2(Q^2, \nu) = x \sum_i e_i^2 f_i(x). \tag{2.34}$$

The functions $f_i(x)$ are denominated Parton Distribution Functions (PDFs). It can be noticed that the following relationship, named *Callan-Gross relation*, holds:

$$F_2(Q^2, \nu) = 2xF_1(Q^2, \nu). \tag{2.35}$$

The sum of all the fractional functions corresponding to each parton should be 1,

$$\sum_i \int_0^1 e_i^2 f_i(x) dx = 1. \tag{2.36}$$

But experimental observations showed that the sum of the charged constituents functions only correspond to 50% of the nucleon's total momentum. Currently, a more realistic model states that three major components form the nucleons: *valence quarks* that carry most of the hadron's momentum and determine the hadron's quantum numbers; *sea quarks*, that are virtual quark-antiquark pairs created inside the hadron[8]; and a vast background of *gluons*, in charge of embedding everything.

This more realistic model implies a violation of Bjorken scaling, which has been observed experimentally, as shown in Fig. 2.10. The Dokshitzer-Gribov-Lipatov-Altarelli-Parisi (DGLAP) equations have been formulated to explain this model [26–28], which describes the PDFs in a scaling-dependent way. These equations are widely used in global determinations of proton or deuteron distributions, such as the CTEQ[9] or NNPDF[10] collaborations, as seen in Fig. 2.9.

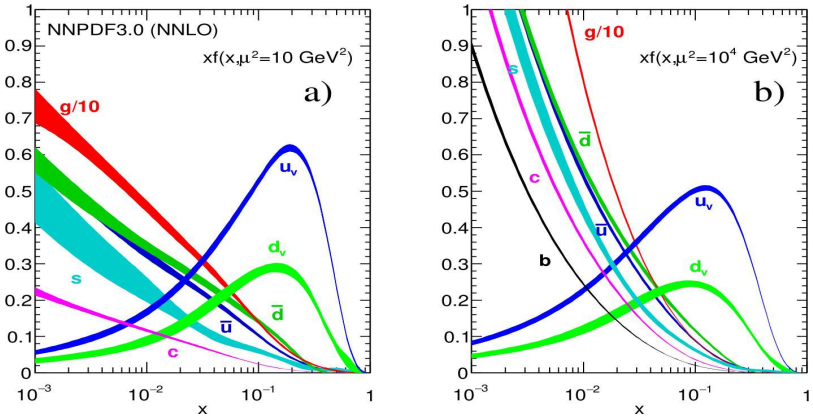

Figure 2.9: The PDFs of the quarks are named according to their flavor: $u(x)$, $d(x)$, $s(x)$, etc. Plots taken from Ref. [22].

8 In a similar way to the Casimir effect in QED.
9 The Coordinated Theoretical-Experimental Project on QCD.
10 Collaboration that determines the Parton Distribution PDFs using Neural Networks.

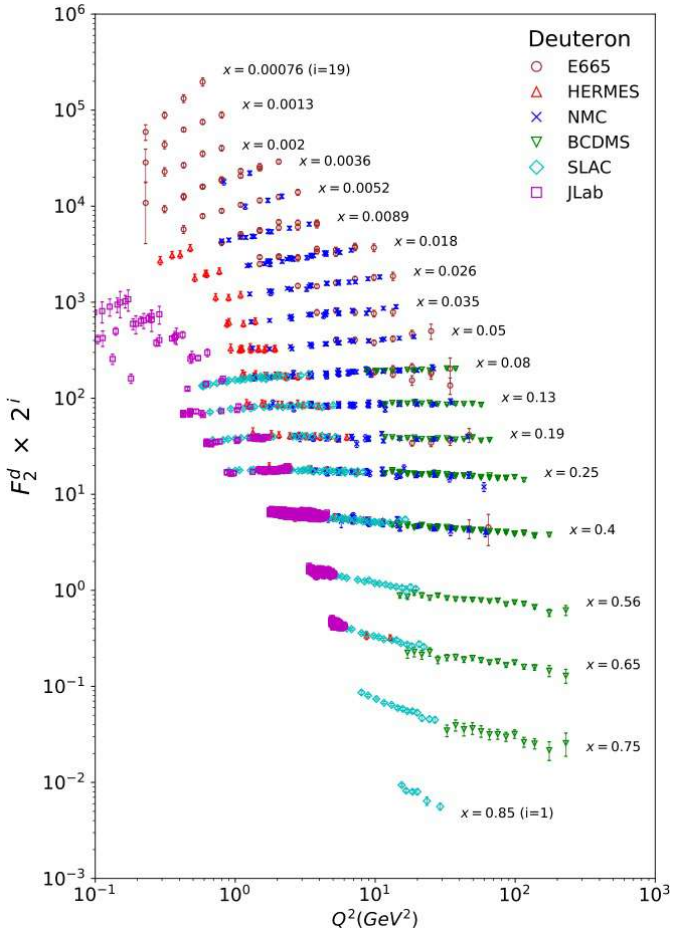

Figure 2.10: The deuteron structure function F_2^d measured in electromagnetic scattering of electrons/positrons (SLAC, HERMES, JLAB) and muons (BCDMS, E665, NMC) on a fixed target, shown as a function of Q^2 for bins of fixed x. For the purpose of plotting, F_2^d has been multiplied by 2^{i_x}, where i_x is the number of the x bin. Plot taken from Ref. [22].

2.8 QUANTUM CHROMODYNAMICS

Quantum Chromodynamics (QCD) is the component of the Standard Model that describes quark–gluon interactions, where *chromo* is the Greek word for color. The interaction between quarks and gluons is called *strong interaction* and is the mechanism responsible for the strong nuclear force, which is in charge of holding most of the ordinary matter together by confining quarks[11] into hadrons and binding *nucleons*[12] together to form the atomic nuclei.

11 Actually, valence quarks, sea quarks, and gluons.
12 Collective term for the hadrons that form atomic nuclei, i.e., protons and neutrons.

Every particle formed by quarks is called a *hadron*. Hadrons can be classified as *mesons*, which are quark-antiquark pairs; and *baryons*, which correspond to bound states of three quarks.

Quoting Ref. [29], the essential properties of QCD are:

- Quarks carry color charge as well as electric charge. There are three colors: red, green and blue.
- The strong interaction, also known as color interaction, is mediated by the exchange of electrically-neutral particles named *gluons*. They correspond to the gauge bosons of the strong nuclear force.
- Color interactions are assumed to be a copy of electromagnetic interactions. In a sense that both theories, QCD and QED, are formulated as a consequence of local gauge symmetries.
- Gluons themselves carry color charge, and there are eight types of them[13].
- The strong interaction is observable at short distances (up to 3 fm).
- The strength of the force its directly proportional to the strong coupling constant, α_s. For example, compared to other interactions at the range of 10^{-15} m the strong force is: approximately 137 times stronger than electromagnetism, approximately a million times stronger than the weak interaction, and approximately thousand times stronger than gravitation.

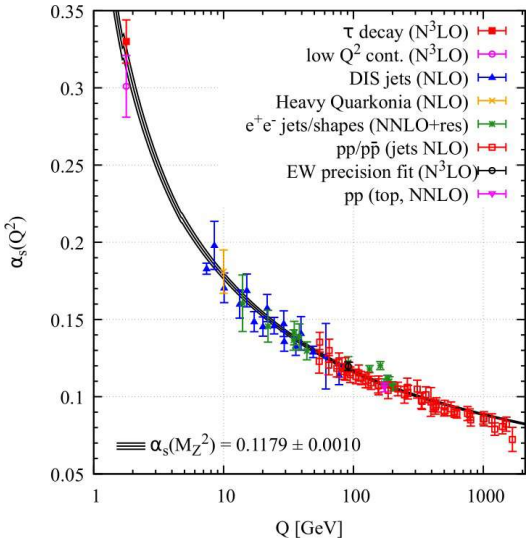

Figure 2.11: Summary of measurements of α_s as a function of the energy scale Q. Plot taken from Ref. [22].

13 Equivalent the octet representation given by the Gell-Mann matrices.

To this day, QCD still presents phenomena that require explanation. For example, the strong interaction has a property called *asymptotic freedom*, where the strength of the strong force diminishes at higher energies (or temperatures). In consequence, when quarks are very close to each other, they behave almost as free particles. This phenomenon is directly related to the running coupling constant of the strong force, α_s, which has proven to decrease at high energies, as seen in Fig. 2.11.

Another of the most important mysteries of QCD is *confinement*, which states that for a particle to be observable, it must be colorless, i.e., have a neutral color charge. In other words, as proven by many experiments, hadrons and mesons can be measured, while quarks and gluons cannot be observed in isolation. Considering this principle, the following question arises: how is it, then, that quarks bind and transform into hadrons?

2.9 HADRONIZATION

Hadronization is the process by which a set of colored partons transform (or combine) into colorless hadrons. It corresponds to a dynamic and low-energy process, which means that current non-perturbative techniques cannot calculate it. However, it can be described by non-established models that are based on general features of the QCD, denominated *phenomenological models*.

A phenomenological description of the time evolution of the hadronization process is illustrated in Fig. 2.12, where two different time-scales are portrayed[14]:

1. *Production length* l_p: just after the virtual photon-quark scattering, the quark propagates and loses energy through gluon bremsstrahlung [30]. This stage finishes when the quark fully neutralizes its color by picking up an antiquark.

2. *Hadron formation length* l_f: after the production time, the produced color dipole –also known as *pre-hadron*, a colorless structure with no definite wave function– will propagate and develop until its wave function collapses into the observed hadron.

It is thought that the stage of production length is characteristic of the propagating quark and independent of the measured hadron. On the contrary, the stage of formation length is expected to heavily depend on the final-state hadron species.

14 They are also known as production time and production length, respectively.

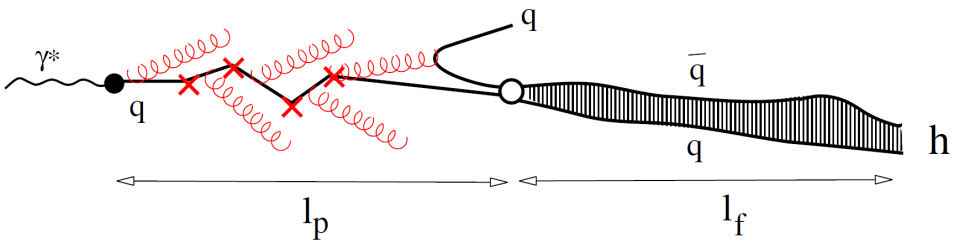

Figure 2.12: Time picture of hadronization. Diagram taken from Ref. [31].

2.9.1 *Lund String Model*

One of the main phenomenological models for describing hadronic interactions is the Lund string model [32]. The main idea of this model is that gluons act as *strings* between propagating partons, similar to electromagnetic field lines, with the important difference that in this case, the field lines do interact between themselves.

The simplest example to describe hadronization through the Lund string model is the propagation of a quark-antiquark pair. Initially, between the two partons, there is a gluonic string that stretches as they propagate. While doing so, their kinetic energy is transformed into potential energy, which is stored in the string between them. An important contribution to the string's potential energy is thought to be due to the self-attraction of the gluonic field. Once enough potential energy has been accumulated, and due to vacuum fluctuations, the string breaks. The potential energy is transformed into mass, causing a new quark-antiquark pair to emerge; as seen in Fig. 2.13a. This process is repeated until only hadrons remain in the final state, as seen in Fig. 2.13b.

The Lund string model is implemented in PYTHIA [33], a general-purpose Monte Carlo event generator widely used by the HEP community.

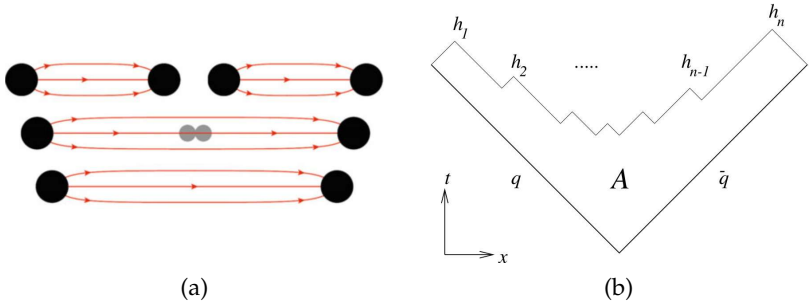

Figure 2.13: String breaking into quark-antiquark creation (a), and space-time picture of string hadronization (b), where h_1, ..., h_n represent the produced hadrons. In both panels, time evolution goes from bottom to top.

2.9.2 *Cluster Model*

The cluster hadronization model is based on the *preconfinement* property of QCD [34]. Initially, after the parton shower, gluons separate into quark-antiquark pairs. These $q\bar{q}$ combinations are grouped into neutral-colored clusters whose invariant mass distributions have a wide range. Finally, these clusters decay into hadrons.

The cluster model has few parameters and is implemented in the HERWIG simulation software [35].

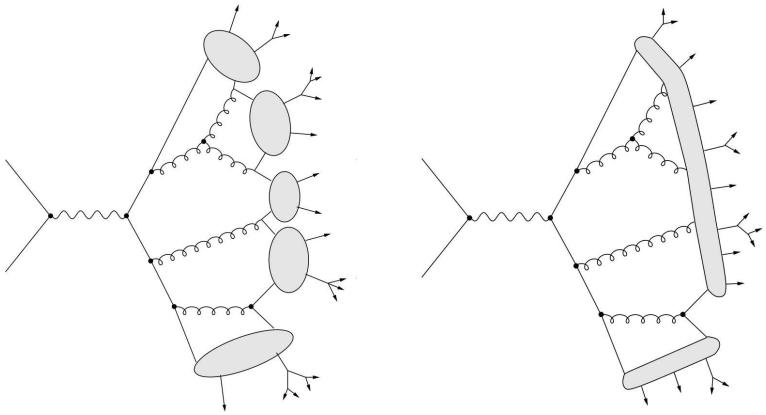

Figure 2.14: Cluster hadronization model (left), and Lund string model (right).

2.10 MULTIPLICITY RATIO

In Semi-Inclusive Deep-Inelastic Scattering (SIDIS), the high virtuality of the virtual photon allows it to be absorbed by a quark, so it can be fragmented before becoming hadrons.

This process is described by the *fragmentation functions* $D_q^h(z)$, which represent the probability density of finding a hadron h produced by a parton q carrying a fraction z of its energy[15].

Fragmentation functions are analogous to the PDFs of Section 2.7: fragmentation functions describe the transition from parton to hadron, just as PDFs describe the partons confined within a hadron. Additionaly, the sum of the energies of all hadrons must be equivalent to the energy of the parent quark:

$$\sum_h \int_0^1 z\, D_q^h(z)\, dz = 1. \tag{2.37}$$

15 Defined earlier as z_h in Eq. 2.21.

The fragmentation functions $D(z)$ describe properties of hadrons and are universal, no matter how the partons are produced. Under few derivations [29], it can be shown that:

$$\frac{1}{\sigma}\frac{d\sigma(eN \to ehX)}{dz} = \frac{\sum_q e_q^2 f_q(x) D_q^h(z)}{\sum_q e_q^2 f_q(x)}, \tag{2.38}$$

where σ is the integrated DIS cross section, $d\sigma/dz$ is the differential semi-inclusive DIS cross section; e_q and $f_q(x)$ is the charge and PDF of the quark q carrying a momentum fraction x of the nucleon N, respectively. In this expression, the fragmentation functions $D(z)$ are independent of x, under the assumption that the virtual photon is absorbed by a quark on a short time scale, and that the quark fragments on a much longer time scale. In other words, the scattering process and the fragmentation process should be independent. This is called the *factorization* assumption, and it can be tested experimentally.

Considering the relationship between event rate R, cross section σ and luminosity $\mathcal{L}$, $R = \sigma\mathcal{L}$, and generalizing into a wider range of variables, one can rewrite the left side of Eq. 2.38 as:

$$D^h(Q^2, \nu, z_h, p_T^2) \equiv \frac{1}{N_e(Q^2,\nu)}\frac{d^4N_h}{dQ^2\, d\nu\, dz_h\, dp_T^2}, \tag{2.39}$$

where N_e is the number of inclusive DIS electrons, and N_h is the number of measured hadrons h in an multi-dimensional interval on the electron variables Q^2, ν and the hadron variables z_h, p_T^2[16]. This new function $D^h(Q^2, \nu, z_h, p_T^2)$ is defined as the *multiplicity* of the hadron h.

Within a nuclear environment, the hadronization process must be influenced by quark energy loss due to gluon radiation and by multiple quark-nucleon scatterings as the quark propagates. Moreover, hadron-nucleon interactions can also affect the process if the hadron is formed inside the nucleus. To measure these effects, one can define the ratio D_A^h/D_D^h between the hadron multiplicities produced in a massive nucleus A and produced in a lighter nucleus of reference D. This observable is known as the Hadronic Multiplicity Ratio (MR) and it's defined as follows:

$$R_A^h(Q^2, \nu, z_h, p_T^2) \equiv \frac{\left(\frac{N_h(Q^2,\nu,z_h,p_T^2)}{N_e^{\text{DIS}}(Q^2,\nu)}\right)_A}{\left(\frac{N_h(Q^2,\nu,z_h,p_T^2)}{N_e^{\text{DIS}}(Q^2,\nu)}\right)_D}, \tag{2.40}$$

where $N_h(Q^2, \nu, z_h, p_T^2)$ is the number semi-inclusive hadrons h in a given (Q^2, ν, z_h, p_T^2) bin, and $N_e^{DIS}(Q^2, \nu)$ is the number of inclusive DIS electrons

16 All of them defined in Section 2.6.

in the same (Q^2, ν) bin. This quantity represents the *attenuation* in hadron production due to nuclear medium effects. For example, in the case of the absence of nuclear environment effects, the present ratio should be equal to 1. Additionaly, information such as hadron formation lengths, the characteristic distances over which hadrons form, can be extracted from R_A^h [36].

Experimentally, the MR is a convenient quantity because it's a double-ratio, reducing many possible systematic effects on its quotient. In addition, it allows a multidimensional study of the impact of the nuclear environment on hadron production, both for various nuclear targets and kinematical variables.

The following section describes MR measurements made by previous collaborations. In the present analysis, one-dimensional MR results for the ω meson are presented in Chapter 6.

2.11 PREVIOUS MEASUREMENTS

In the 1970s, the Stanford Linear Accelerator Center (SLAC) pioneered the measurement of the effect of the nuclear environment on hadron electroproduction by using a 20.5 GeV electron beam incident on different nuclear targets: deuterium, beryllium, carbon, copper and tin. They observed the attenuation R_A^h of the forward hadrons for the first time and found that it increases as a function of the nucleus's size [4].

Later in 1991, the European Muon Collaboration (EMC) of the European Organization for Nuclear Research (CERN), known for the EMC effect

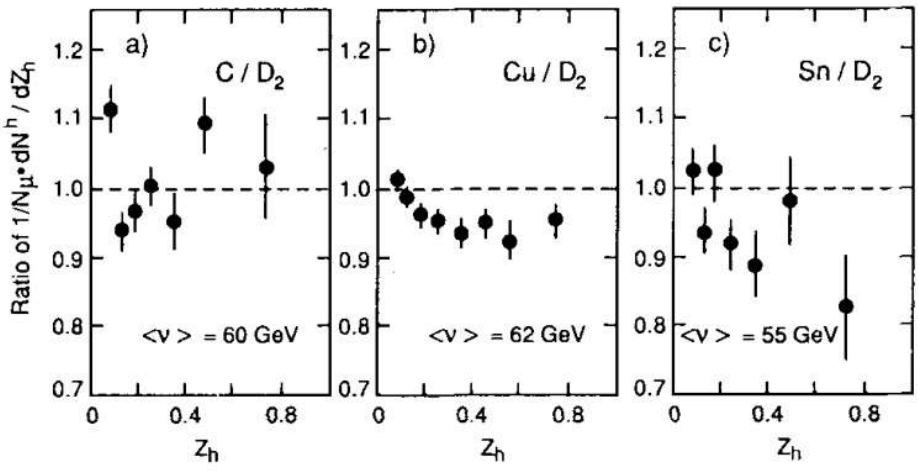

Figure 2.15: Values of R_A^h as a function of z_h for different targets: carbon, copper and tin, on plots (a), (b), and (c), respectively. Results measured by the EMC Collaboration. Plots taken from Ref. [5].

[37], carried out similar studies. But this time, with higher luminosity and performing several experimental runs with high muon energies of 100, 120, 200, 280 GeV, incident on deuterium, carbon, copper and tin. To reduce systematic uncertainties, this was the first experiment to expose targets simultaneously in the beamline. At these energy levels, they observed rather small nuclear effects [5]. However, the obtained results discarded many theoretical models proposed at the time.

In 1994, the Experiment-665 of Fermilab (E665) measured DIS with a more energetic muon beam of 490 GeV incident on two targets: deuterium and xenon, and found almost no nuclear dependence [6]. In conclusion, both experiments done by EMC and E665 confirmed that the optimal energy levels to study hadronization are between 1-50 GeV., inspiring the design of future experiments at HERMES and CLAS.

More recently, the collaboration that has published the most experimental studies on hadronization is the HERA Measurements of Spin (HERMES) Collaboration from the Deutsches Elektronen-Synchrotron (DESY), Germany. They performed experiments with electron and positron beams, with 27.6 GeV of energy, incident on deuterium, helium, nitrogen, krypton and xenon. For the first time, the experiments had the capacity to identify the hadrons and not just separate them by charge. The HERMES collaboration performed an extensive study on the hadronization of several hadrons, such as $\pi^{\pm}$, π^0, $K^{\pm}$, $p, \bar{p}$. The R_A^h results were presented as functions of the variables Q^2, ν, z_h, and p_T^2:

- 1-dimensional multiplicity ratio R_A^h for $\pi^{\pm}$, $K^{\pm}$, $p, \bar{p}$ [9].
- 1-dimensional multiplicity ratio R_A^h for π^0 [9].
- 2-dimensional multiplicity ratio R_A^h for $\pi^{\pm}$, $K^{\pm}$, $p, \bar{p}$ [11].

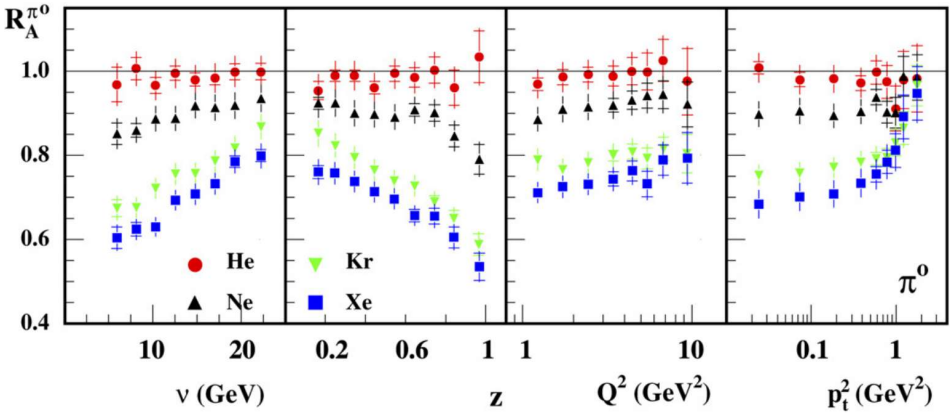

Figure 2.16: Values of R_A^h for π^0 as a function of ν, z_h, Q^2 and p_T^2, measured for helium, neon, krypton, and xenon. Results obtained by the HERMES Collaboration [9].

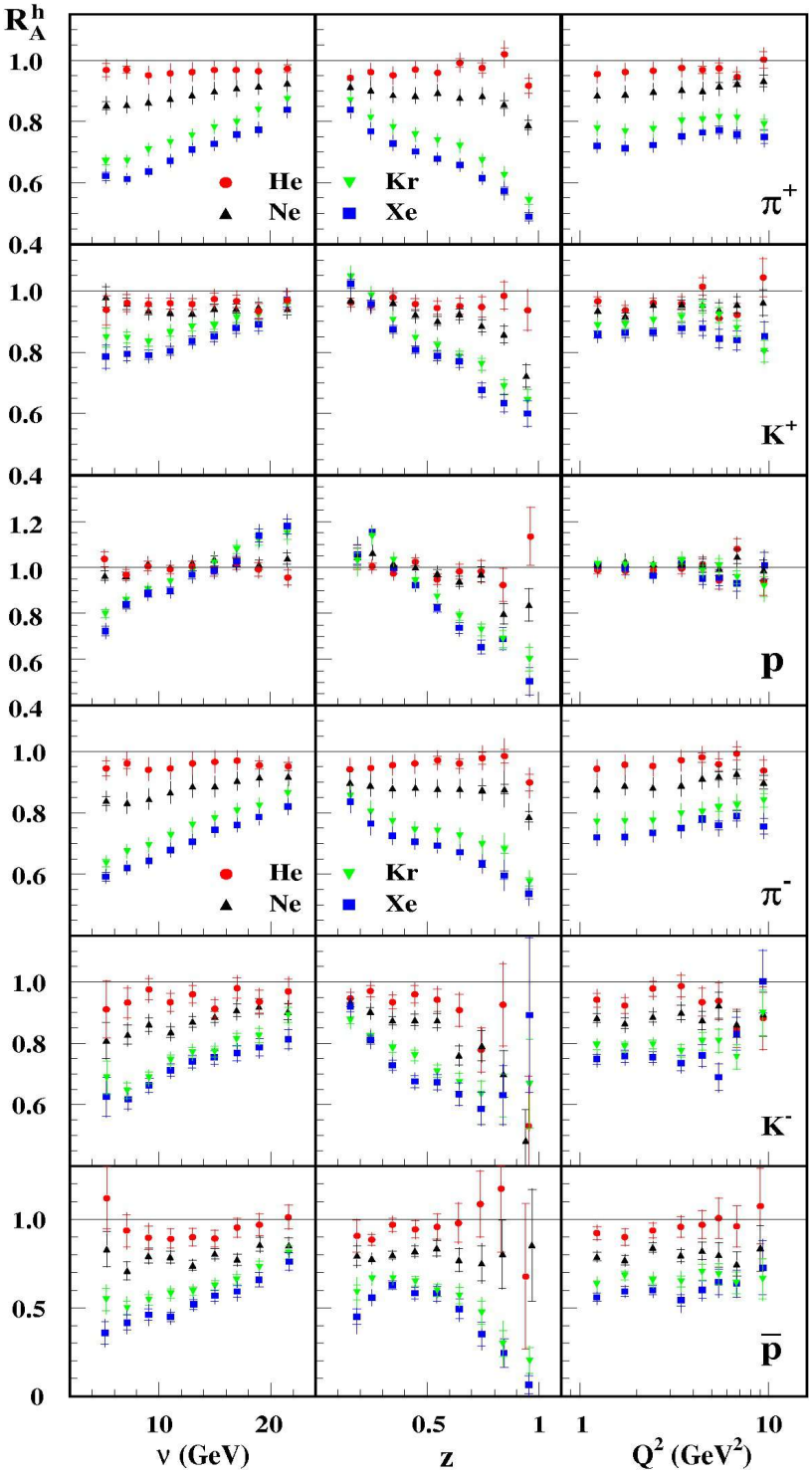

Figure 2.17: Values of R_A^h for ($\pi^{\pm}$, π^0, K^+) as a function of ν, z_h and Q^2, measured for helium, neon, krypton, and xenon. Results obtained by the HERMES Collaboration [9].

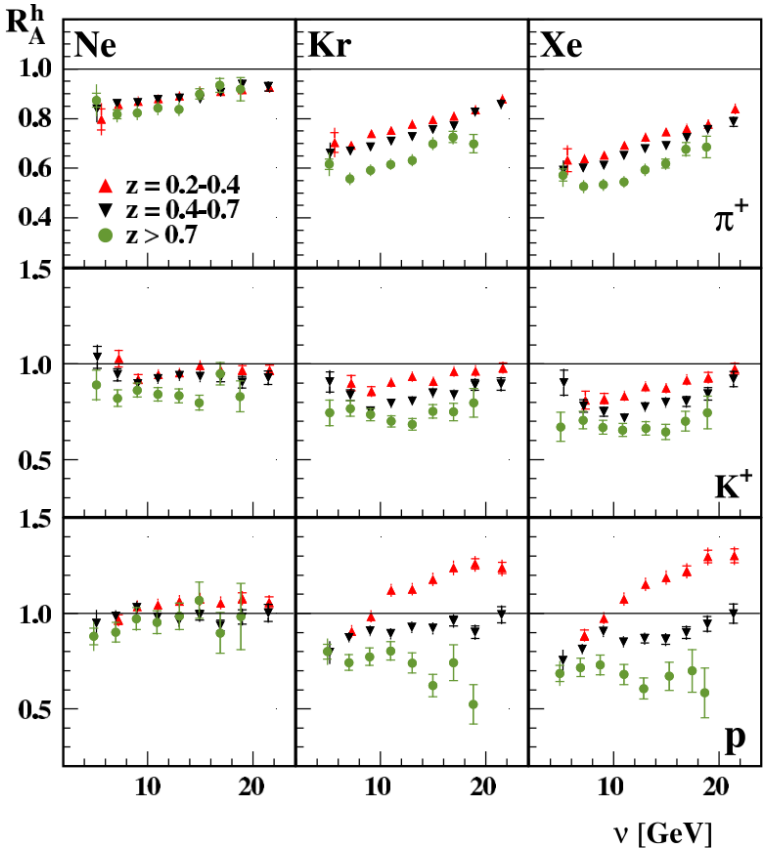

Figure 2.18: Values of two-dimensional R_A^h for (π^+, K^+, p) as a function of ν and z_h, measured for neon, krypton, and xenon. Results obtained by the HERMES Collaboration [11].

At these energy levels, the attenuation R_A^h decreases with increasing nuclear size, almost independent at high p_T^2. For the first time, the MR was observed to increase with z_h and decrease with ν. And the average values of R_A^h are shown to be in the same order of magnitude for $\pi^\pm$, π^0, K^+; however, they are very different from K^-, p, $\bar{p}$.

2.12 THE MESON SECTOR

The present analysis corresponds to the world's first studies on the hadronization of the ω meson and is part of a collaborative line of investigation on the hadronization of the meson sector.

The dataset to study was measured in 2004 by the EG2 experiment of the CLAS Collaboration, with higher luminosity and higher acceptance than the previously mentioned experiments. SIDIS measurements were performed with a 5 GeV electron beam incident on deuterium, carbon, iron and lead. The hadronization on nuclei results involve:

- 1-dimensional R_A^h for K_s^0, by Aji Daniel [14].
- 4-dimensional R_A^h for $\pi^{\pm}$, by Sebastián Morán, Hayk Hakobyan *et al.* [15–18].
- 3-dimensional R_A^h for π^0, by Taisiya Mineeva [19, 20], as shown in Fig. 2.19.
- 1-dimensional R_A^h for η, by Orlando Soto [21].

As the same data are being used, the present thesis maintains the methods, corrections and Particle Identification (PID) cuts established by the EG2 experiment group. More information about the CLAS and the experiment can be found in Chapter 3.

Table 2.1 compares the three electrically neutral mesons π^0, η and ω. As can be appreciated, the ω meson is the heaviest and the only vector meson among the three. The three of them have extremely short lifetimes, leading to reconstruct their masses through their decay channels. They also have nearly the same quark content, except for the η, which contains strangeness. Regarding their decay channels, ω shares the three-pion decay channel with the η meson, and from that channel, ω decays into π^0, which later decays into 2γ.

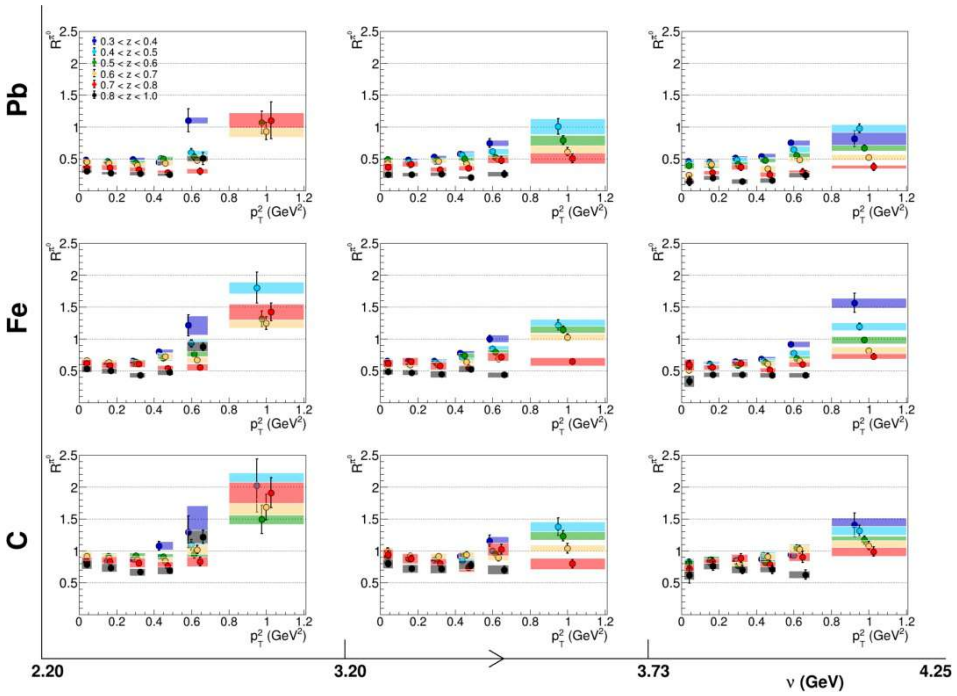

Figure 2.19: Values of R_A^h for π^0 as a function of (ν, z_h, p_T^2), measured for carbon, iron and lead. Results obtained by Taisiya Mineeva for the CLAS Collaboration [20].

Particle	π^0	η	ω
Charge	0	0	0
Type of meson	Pseudoscalar	Pseudoscalar	Vector
Mass (GeV)	0.135	0.548	0.782
Mean lifetime (s)	$\sim 10^{-17}$	$\sim 10^{-19}$	$\sim 10^{-23}$
Quark content	$u\bar{u} - d\bar{d}$	$u\bar{u} + d\bar{d} - 2s\bar{s}$	$u\bar{u} + d\bar{d}$
Decay channels (%)	$\pi^0 \to \gamma\gamma$ (99%)	$\eta \to \gamma\gamma$ (39%) $\eta \to \pi^0\pi^0\pi^0$ (33%) $\eta \to \pi^+\pi^-\pi^0$ (23%)	$\omega \to \pi^+\pi^-\pi^0$ (89%) $\omega \to \pi^0\gamma$ (8%)

Table 2.1: Table of comparison between mesons π^0, η and ω [22].

3

EXPERIMENTAL SETUP

Founded in 1984, Thomas Jefferson National Accelerator Facility (TJNAF), also known as Jefferson Lab (JLAB), is a U.S. laboratory focused on the study of nuclear matter through high-energy physics experiments. The laboratory operates the Continous Electron Beam Accelerator Facility (CEBAF) [38], a linear electron accelerator connected to experimental end stations called *Halls*. Among them, Hall B houses the CEBAF Large Acceptance Spectrometer (CLAS) [12], which is assembled from multiple detectors to measure multiparticle final state reactions and conduct experiments that require large acceptance.

This chapter summarizes the different experimental apparatus used to produce the data analyzed by this work. From outside to inside, Section 3.1 will give a brief description of the CEBAF, Section 3.2 will broadly explain the functioning of the multiple detectors that form CLAS, and Section 3.3 will describe the setup of the CLAS EG2 experiment [13], from which all the data presented in this analysis were measured.

3.1 THE CONTINUOUS ELECTRON BEAM ACCELERATOR FACILITY

Built 8 m below the Earth's surface, the Continous Electron Beam Accelerator Facility (CEBAF) is an underground racetrack-shaped electron accelerator used to study nuclear reactions. Figure 3.1 shows an aerial view of the accelerator complex, and Fig. 3.2 illustrates the components of the accelerator.

Figure 3.1: Aerial view of the CEBAF.

Initially, the electron beam is produced in the injector with a Radio-Frequency (RF) electron gun, formed by a laser hitting a photocathode. Electrons are produced out of phase and maintained that way within all the accelerator's structure to be delivered simultaneously into each experimental hall with different energies and currents, as depicted in Fig. 3.3.

After leaving the injector with a 45-MeV energy, the electron beam enters the north *linac*, which is one of the two anti-parallel linear accelerators. Each linac has a length of 1.4 km, which accelerates the electron beam up to 0.6 GeV energy for each pass. They consist of superconducting niobium cavities that boost the beam with RF waves, which are achieved with the liquid helium produced by the Central Helium Liquefier (CHL), capable of cooling the niobium down to approximately 2 K.

Both linacs are connected by recirculation arcs, which are two magnetic arc sections with a radius large enough not to slow down the electrons due to synchrotron radiation. The electrons are separated by momentum to circulate in each of the 9 arcs. For each pass, an electron can accelerate up to 600 MeV. So, an electron beam that travels 5 entire orbits can reach up to 6 GeV of energy.

Finally, the electron beam leaves the south linac and is delivered every 2 ns to each of the three experimental halls. Each hall corresponds to a domed chamber equipped with detectors to measure the interactions between incoming electrons and distinct target materials. For the case of the Hall B, the luminosity is limited up to 2×10^{34} cm^{-2}s^{-1}.

3.2 THE CEBAF LARGE ACCEPTANCE SPECTROMETER (CLAS)

The CEBAF Large Acceptance Spectrometer (CLAS) is a magnetic spectrometer with almost 4π acceptance in solid angle, making it ideal for studying multi-particle final states because of the larger available phase space [12]. It can detect charged particles with polar angles from 8° to 140°, neutral particles from 8° to 75°, and full azimuthal coverage.

The CLAS detector is based on a toroidal magnet, referred to as the *main torus*, composed of six coils placed perpendicular to the incoming electron beam, separating the CLAS into six symmetrical parts, described as *sectors*. The coils' current produces a toroidal magnetic field that bends charged particles toward or away from the beam axis in the polar direction but keeps the azimuthal angle essentially unchanged.

The target is located on the beam axis, near the CLAS geometrical center, and the total beam current received by the target is measured by the Faraday Cups situated at the end of the beamline. Each sector operates as a separate spectrometer while sharing the same target, trigger, and data acquisition system.

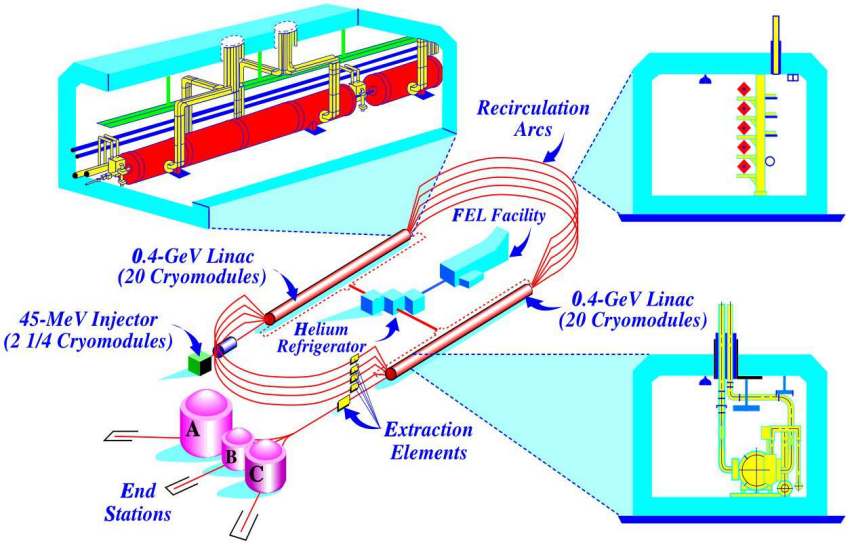

Figure 3.2: Schematic representation of the CEBAF. In the upper left corner, one can see a close-up of the north linac showing one of the cryomodules. In the upper right corner, a cross section of the five recirculation arcs is depicted. In the lower right corner, a vertical cross section of a cryomodule is shown. The two linacs and bending arcs appear in the center of the image. The electron beam starts at the injector and ends in the experimental Halls A, B, and C.

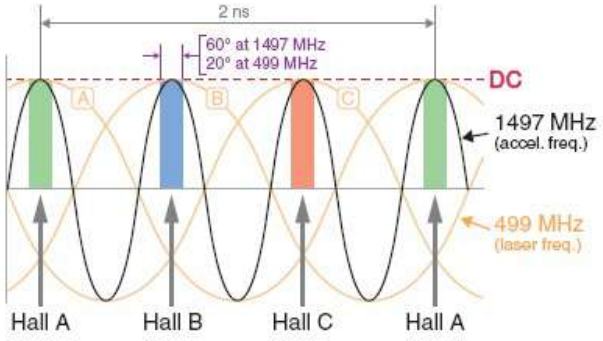

Figure 3.3: Schematic representation of the RF accelerating system.

As seen in Figures 3.4 and 3.5, CLAS is a large assembly of detectors. From the center to the periphery, the particle detection system consists of Drift Chambers (DC) to determine charged particles' trajectories [39], Cherenkov Counters (CC) for identifying light-charged particles [40], Scintillator Counters (SC) for Time of Flight (TOF) measurements [41], and Electromagnetic Calorimeters (EC) to identify showering particles [42, 43].

Placed between the targets and the first region of the DC, there is a second magnet. Referred to as the *mini-torus*, it shields the detectors from

the target's charged electromagnetic background produced by scattered Møller electrons.

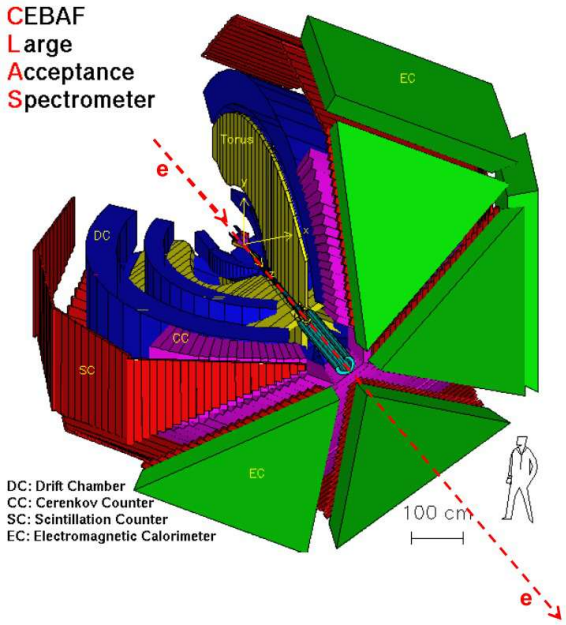

Figure 3.4: Schematic view from outside CLAS. Red dashed line indicates beam direction. Each component can be seen: magnetic torus (yellow), DC (blue), CC (magenta), SC (red), and EC (green).

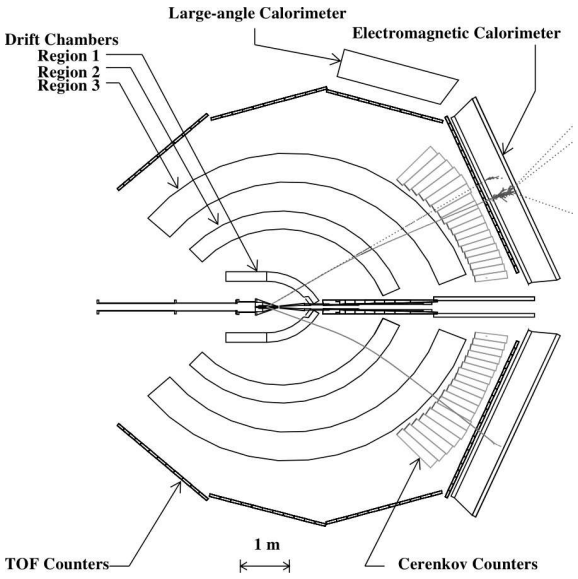

Figure 3.5: Schematic top view of the CLAS, cut along the beamline. Outgoing photon, electron, and proton tracks are shown from top to bottom.

3.2.1 *Drift Chambers (DC)*

The first detectors to receive the scattered electrons and outgoing particles are the multiwire Drift Chambers (DC), which map the trajectories of charged particles with momentum greater than 200 MeV with a resolution of 0.5% and an angular coverage from 8° to 140° in the polar angle and 80% in the azimuth.

The fundamental principle of operation of the DC is based on the ability to ionize matter by the high-energy particles. In this case, each wire cell is filled with a gas mixture of 90% Ar and 10% CO_2, where the passage of a charged particle would produce electrons to trigger the signal. Fig. 3.6 shows a typical track pattern passing through the cells.

Each of the six sectors of the DC consists of three separate regions, being a total of 18 drift chambers. Region 1 (R1) is the closest to the target and is under the weakest magnetic field. Region 2 (R2) is located between the magnetic coils, characterized by the strongest magnetic field. And Region 3 (R3) has the largest chambers, placed outside of the torus magnet influence. R1 and R3 are used to determine the particle's initial and final directions, respectively, while R2 is used to determine the particle track's maximum curvature.

To increase pattern recognition, each chamber is divided into two superlayers of wires: one axial superlayer aligned in parallel to the magnetic field and one stereo superlayer, tilted at 6° with respect to the axial wires. These two different directions allow determining the azimuthal angle ϕ of the particle. Each superlayer is made up of 6 layers of hexagonal wire cells, except for the stereo superlayer in R1, which only has 4 layers.

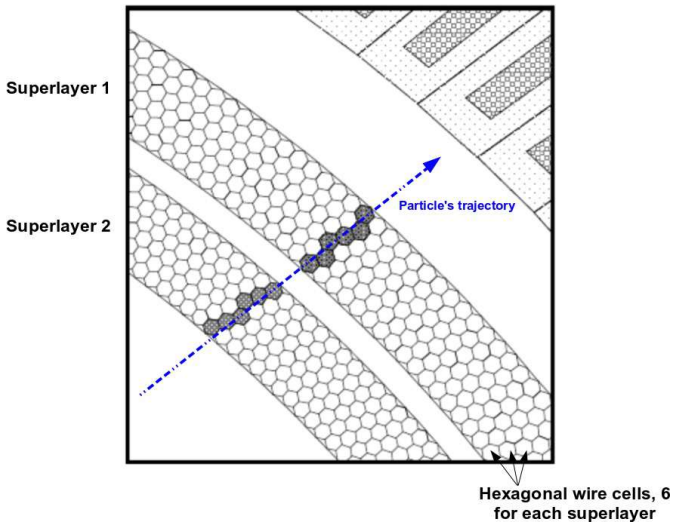

Figure 3.6: Layout of superlayers in the R3 of the DC.

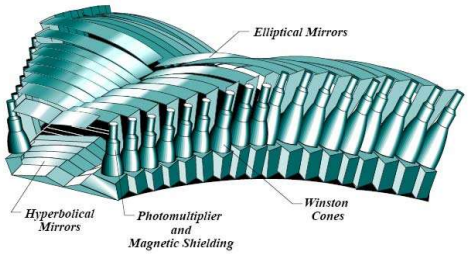

Figure 3.7: External representation of a CC module.

3.2.2 *Cherenkov Counters (CC)*

After passing through the DC, the outgoing particles must travel through the Cherenkov Counters (CC) [40], located in the forward region of every sector, covering polar angles up to 45° and a full azimuthal range, as seen in Fig. 3.7.

The CC are used in the trigger system for electron scattering experiments and to differentiate electrons from negative pions up to 2.5 GeV by measuring the number of photoelectrons emitted due to Cherenkov radiation.

The Cherenkov Radiation corresponds to the electromagnetic radiation emitted by a charged particle when passing through a dielectric medium at speed greater than the speed of light in that medium. Due to its high refractive index, the CC are filled with C_4F_{10}. Hence the speed of light within that gas is slightly lower than the speed of light in vacuum. An electron traveling through the active volume of the detector typically produces $4-5$ photoelectrons.

The CC in each sector consists of two identical sub-sectors, each consisting of 18 optical modules, giving a total of 216 light-collecting modules. Each module is equipped with elliptical, hyperbolic, and cylindrical mirrors to direct the light into light-collection cones (Winston cones) with Photomultiplier Tubes (PMT) attached to their ends.

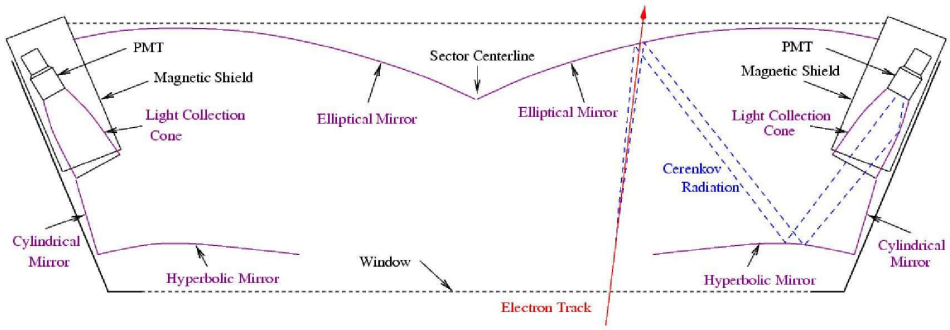

Figure 3.8: Schematic view of the internal components of a CC module.

3.2.3 *Scintillator Counters (SC)*

The Scintillator Counters (SC) or Time of Flight (TOF) counters [41], located radially outside the tracking system and the CC, have an angular coverage of $8 - 142^\circ$ in the polar angle and the entire azimuthal range.

Time of Flight (TOF), corresponds to the time interval ΔT during which a particle travels a length Δl_{SC} from the point of interaction in the target to the CLAS's external boundary, where the TOF system is located. This is the most important measurement for particle identification because it enables measuring the particle's velocity, β. Which in addition to the measured momentum p by the DC, it allows the reconstruction of the particle's mass m, as follows:

$$\beta \Rightarrow \beta = \frac{\Delta l_{SC}}{\Delta T} \Rightarrow m = \frac{p\sqrt{1-\beta^2}}{\beta}. \tag{3.1}$$

Each of the six sectors has 57 organic plastic scintillators. Additionally, each SC system is aligned perpendicular to the average local particle trajectory with a PMT at each end, as seen in Fig. 3.9. The system has been designed to optimize the timing resolution from 100 to 200 ps, depending on the scattering angle.

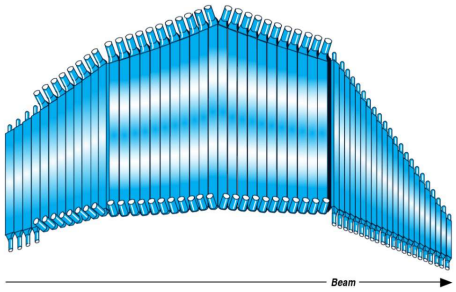

Figure 3.9: External representation of a TOF counter.

3.2.4 *Electromagnetic Calorimeters (EC)*

The Electromagnetic Calorimeters (EC) are the last components of the CLAS to detect the outgoing particles. The forward calorimeter modules [42] cover from 8° to 45° in the polar angle, and the two modules of the Large-Angle Calorimeter (LAC) [43] extend the coverage up to 75° in two sectors.

The primary goals of the EC are detecting and triggering electrons at energies above 0.5 GeV, detecting photons at energies above 0.2 GeV to allow for π^0 and η reconstruction, and detecting neutrons. It is designed to collect the total energy deposited by the electromagnetic showers caused

by electrons or photons. For the case of charged pions, they are minimum ionizing particles, which means they deposit a small constant fraction of energy regardless of their momentum. In addition to the information measured by the CC, this difference is what allows the separation of electrons and charged pions. On the other hand, the discrimination of photons and neutrons is achieved through the TOF system.

The EC are an assembly of alternating layers of plastic scintillators and lead, with a thickness of 16 radiation lengths, that allow measuring the particles' energy. The lead sheets work as a passive medium, or absorber, to induce electromagnetic showers. The scintillator strips act as an active medium that produces the signal output and delivers it through optical fibers to the readout system placed on the back of the calorimeter.

Each EC sector corresponds to 39 triangular layers distributed equally into three planes of observation, or views: U, V, W, as seen in Fig. 3.10, which provide stereo information on the position of energy deposition. Each view is further subdivided into an inner and outer stack, providing longitudinal sampling to improve separation between hadrons and electrons. For notation purposes, the energy deposited in the 5 innermost layers is E_{in}, the energy deposited in the 8 outermost layers is E_{out}, and the energy deposited all the 13 layers is E_{tot}. The ratio between energy deposited to the incoming particle's total energy is called sampling fraction f_S and is estimated to be $\approx 27\%$ for electrons and photons.

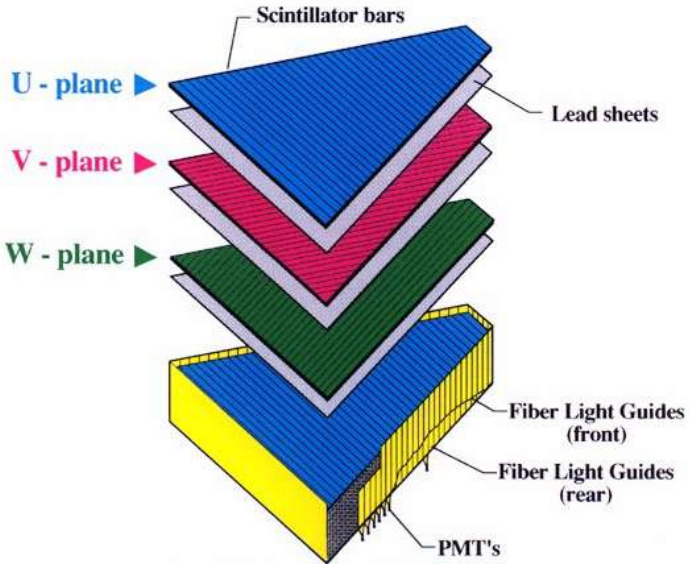

Figure 3.10: Exploded view of one of the six EC modules. The three different planes of observation (U, V, W) are depicted.

3.3 THE EG2 EXPERIMENT

The CLAS experiments "Quark Propagation Through Cold QCD Matter", E-02-104 [44], and "Q^2 Dependence of Nuclear Transparency for Incoherent ρ^0 Electroproduction", E-02-110 [45], operated in parallel during the EG2 experimental run. It collected data in 2003-2004 over three run-periods: *EG2a* with an electron beam of 4.0 GeV; *EG2b*, with an electron beam of 4.5 GeV; and *EG2c* an electron beam of 5.014 GeV. The present work forms part of the E-02-104 program and analyses the data collected from the *EG2c* period, which provides the largest statistics amongst the three run-periods. For this particular period, the magnetic currents of the torus and mini-torus were fixed at 2250 A and 6000 A, respectively. More information, such as the complete list of run numbers and the beam currents of the EG2c period, can be found in Ref. [46].

One of the objectives of the EG2 experiment is to understand one particular phenomenon of quark propagation through cold nuclei: the process of hadronization. To gather information about the characteristic time-distance scales of this process, a DIS experiment on a range of different nuclei was proposed. In this sense, a double-target system was designed and built to measure the nuclear environment's effects on the electroproduction of hadrons.

The experimental requirements for the double-target system were as follows [13]:

1. Large acceptance for semi-inclusive and exclusive kinematics, plus a good match to the CLAS spectrometer acceptance.
2. Minimal mass for low-energy particles at large angles (70-140° relative to the beam direction) as well as forward-going particles.
3. Approximately equal scattering rates for two targets in the beam simultaneously.
4. One of the targets needed to be a stable deuterium cryotarget.
5. Less than 2-3% of a radiation length of any target material to suppress secondary electromagnetic processes.
6. Minimal entrance/exit window thicknesses for cryotarget to maximize target/window ratio.
7. Rapid target changes for the heavy nuclear targets.
8. Minimal amount of mass in support structure.

The advantage of having the two targets in the beamline simultaneously is that several systematic effects related to the beam and inefficient detector channels will cancel in the quotient of the Multiplicity Ratio (MR), increasing the precision of the final results.

To achieve this, the system was assembled with solid targets supported by mechanical arms, which allow the swapping of targets remotely and within a few seconds, and the cryogenic liquid deuterium target in the back, enveloped in aluminum foils as depicted in Fig. 3.12a. The two targets are aligned along the beamline and separated by only 4 cm to reduce the acceptance differences between them.

The solid targets chosen for this experiment were carbon, aluminum, tin, iron, and lead, making it possible to measure the hadron production from nuclei of various sizes and contrast it to the production from deuterium, which essentially is no nuclear environment. The experimental runs to study in the present analysis are the carbon (C), iron (Fe), and lead (Pb) runs, as they have the most statistics.

Target	Thickness (cm)
^{12}C	0.17
^{56}Fe	0.04
^{207}Pb	0.014

Table 3.1: Thickness of the three solid targets under study, in cm.

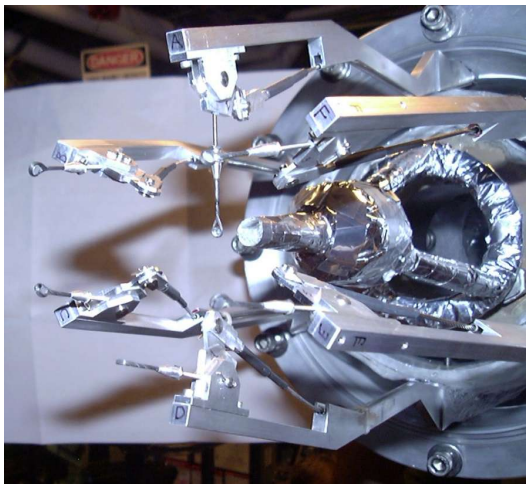

Figure 3.11: Photograph of the full double-target assembly for the EG2 experiment, showing one solid target inserted, five solid targets retracted, and the thermally insulated cryotarget cell [13].

Fig. 3.12b gives a clear representation of the size of the solid targets. The length of the liquid target was 2 cm, while the solid targets had a form of a circular disk with a radius of 0.15 cm and variable thickness, detailed in Table 3.1. The thickness of each target was selected to get an equal number of nuclei along the target length for all cases. However, the thickness of the lead target was reduced by half because of excessive background previously measured.

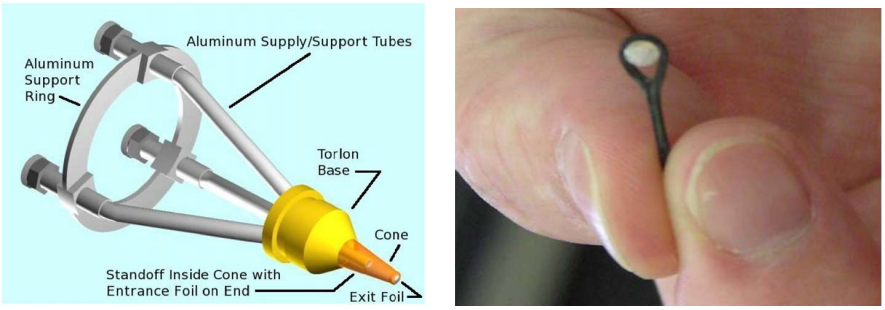

(a) (b)

Figure 3.12: Design of the cryotarget cell to be filled with liquid deuterium (a), and photograph of one of the solid targets surrounded by a carbon fiber loop (b).

3.4 DATA ACQUISITION AND PROCESSING

Once the accelerator and detectors are operating, the outgoing electron and many particles will be measured by the various detectors that constitute CLAS. The method for recording the received electrical signals and converting them to data is known as Data Acquisition System (DAQ), with its process is described in Fig. 3.13.

The condition for an event to be saved is part of the triggering system. In the case of hadron electroproduction experiments, the condition that triggers the DAQ to record the event is the detection of the scattered electron through a coincident signal between the EC and the CC over a certain threshold. This is known as the Level 1 trigger, designed to form and send a fast signal to the Read-Out-Controllers (ROCs).

The Level 2 trigger reads the DC information to find possible tracks. If no candidate is found, Level 2 registers it and continues searching for more triggers. Otherwise, the event is sent to the Event Builder (EB), responsible for recreating the entire event by gathering the different responses from each detector and storing the information in banks. Then, the Event Recorder (ER) process writes the data to the Redundant Array of Inexpensive Disks (RAIDs) for monitoring, to finally be transferred to

the tape silo in the massive data system of Jefferson Lab for permanent storage.

The accelerator and detector operation and data acquisition process is monitored live to assess the detector components' status and the quality of the data.

The collected RAW data is stored in Bank Object System (BOS) format–an established file format in HEP experiments–and each run is separated into multiple files of approximately 10 million events each. These files are processed by an offline reconstruction software called RECSIS to identify the particles [47]. This process is known as *cooking* and has three steps:

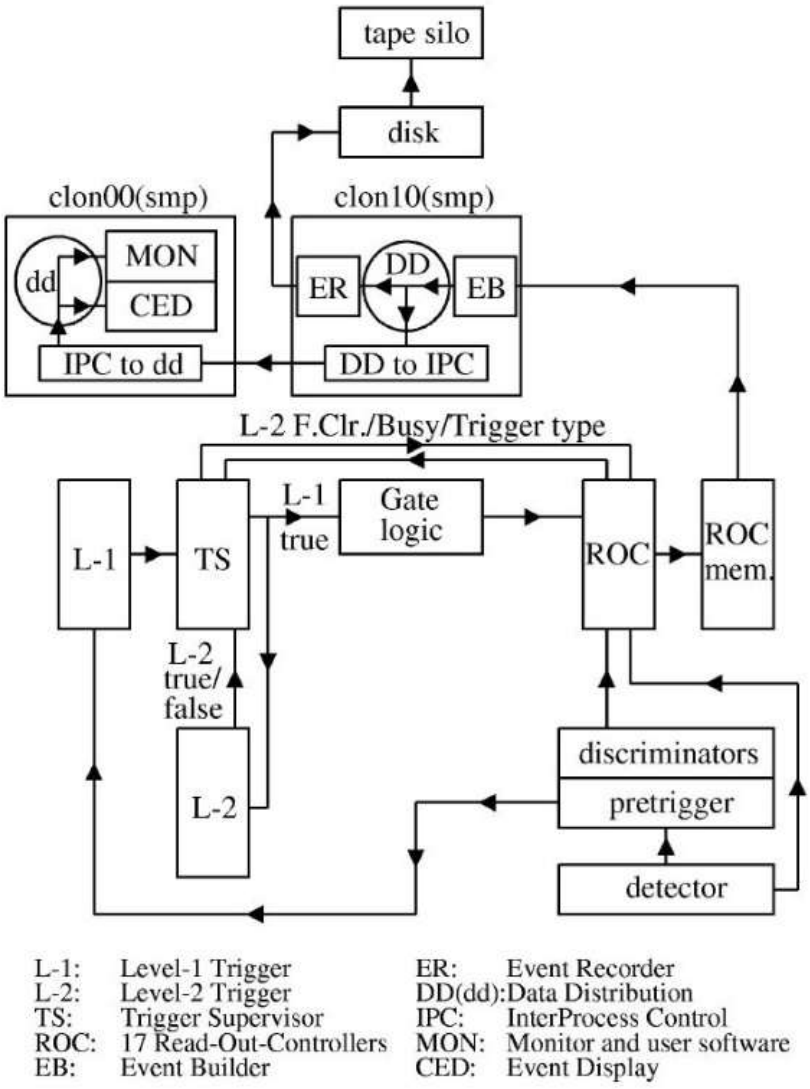

Figure 3.13: Flow diagram of the Data Acquisition System (DAQ).

1. Calibration of the signals from all detector subsystems. Measured energy in each detector is determined by the ADCs (analogous-to-digital converters), and timing information is given by the TDCs (time-to-digital converters).

2. Using the Simple Event Builder (SEB) [48], calibration constants convert the ADC and TDC signals into hits and record this information in the BOS format, using time-based tracking and geometrical matching, generating a preliminary Particle Identification (PID).

3. The BOS file is passed through the offline event reconstruction software (RECSIS), which translates the detector signals and stores their characteristic variables (tracking, charge, momentum, timing, etc.) into different formats, such as BOS banks or ROOT tuples.

The reconstruction, or *cooking*, used in this analysis is the *pass2*, performed by Taisiya Mineeva in 2009, in order to refine the PID and increase the electron and pion statistics by a factor of two, compared to the first cooking developed in 2005. The list of selected run numbers used in this analysis is given by Tables 3.2, 3.3 and 3.4.

More information about the DAQ, the cooking process and calibration procedures can be found in References [15, 49, 50].

Carbon Run Numbers							
42011	42012	42013	42014	42015	42016	42017	42022
42024	42025	42026	42027	42028	42029	42030	42031
42032	42033	42034	42037	42038	42039	42041	42042
42043	42044	42047	42048	42049	42050	42051	42052
42053	42054	42055	42056	42057	42058	42059	42060
42061	42062	42063	42064	42065	42066	42067	42068
42069	42070	42071	42072	42073	42074	42075	42076
42077	42078	42079	42080	42081	42082	42083	42084
42085	42086	42087	42088	42089	42090	42097	42098
42099	42100	42101	42102	42103	42104	42105	42106
42107	42108	42109	42111	42112	42113	42114	42115
42116	42117	42118	42119	42120	42121	42122	42123
42124	42125	42126	42127	42128	42129	42130	42131
42132	42133	42134	42135	42136	42137	42138	42139
42141	42142	42143	42144	42145	42146		

Table 3.2: List of the selected 118 run numbers for Carbon.

Iron Run Numbers							
41146	41147	41148	41149	41150	41153	41155	41158
41159	41161	41163	41164	41165	41166	41167	41168
41170	41171	41172	41173	41174	41175	41176	41177
41178	41179	41180	41181	41182	41184	41188	41189
41192	41197	41199	41200	41205	41206	41207	41208
41209	41210	41211	41212	41213	41214	41218	41220
41222	41235	41236	41239	41240	41241	41243	41244
41245	41247	41248	41249	41252	41256	41258	41259
41260	41261	41262	41263	41264	41265	41266	41267
41268	41269	41270	41271	41272	41273	41276	41285
41286	41287	41288	41289	41290	41291	41292	41293
41294	41295	41296	41297	41298	41299	41300	41301
41302	41306	41314	41316	41317	41318	41319	41320
41321	41322	41325	41326	41327	41328	41331	41332
41335	41336	41337	41338	41339	41340	41341	41344
41345	41346	41347	41348	41349	41350	41351	41352
41353	41354	41355	41356	41357	41358	41359	41360
41361	41362	41363	41364	41365	41366	41368	41369
41370	41371	41372	41373	41376	41377	41379	41382
41383	41384	41385	41386	41388	41389	41391	41392
41393	41395	41398	41399	41400	41402	41403	41405
41406	41407	41408	41409	41410	41413	41414	41415
41416	41417	41419	41420	41421	41424	41425	41426
41428	41429	41436	41442	41443	41444	41445	41446
41447	41450	41451	41452	41453	41454	41455	41457
41458	41459	41460	41461	41465	41466	41467	41468
41469	41470	41471	41472	41473	41474	41475	41476
41478	41479	41482	41483	41490	41492	41493	41496
41497	41498	41499	41500	41501	41502	41503	41504
41505	41509	41512	41513	41514	41515	41516	41517
41518	41519	41520	41521	41524	41525	41526	41527
41528	41529	41531	41532	41533	41535	41536	41537
41538	41539	41540	41541	41542	41543		

Table 3.3: List of the selected 262 run numbers for Iron.

Lead Run Numbers							
41762	41763	41765	41766	41767	41771	41772	41773
41774	41775	41776	41777	41778	41779	41780	41790
41791	41802	41803	41804	41805	41808	41809	41810
41811	41812	41813	41814	41815	41816	41817	41818
41819	41820	41821	41822	41823	41824	41825	41826
41827	41828	41829	41830	41831	41832	41833	41835
41836	41837	41838	41839	41841	41842	41843	41844
41845	41846	41847	41848	41862	41863	41864	41865
41866	41867	41868	41869	41870	41871	41872	41873
41874	41875	41876	41877	41878	41879	41880	41881
41883	41884	41885	41886	41887	41888	41889	41890
41891	41892	41893	41896	41897	41898	41899	41900
41901	41902	41903	41906	41907	41908	41910	41911
41912	41913	41914	41915	41916	41917	41918	41920
41928	41929	41930	41931	41932	41933	41934	41935
41936	41937	41938	41939	41940	41941	41942	41943
41952	41953	41954	41955	41956	41957	41958	41959
41960	41961	41962	41963	41965	41966	41967	41968
41969	41970	41971	41972	41973	41974	41975	41976
41977	41981	41982	41983	41984	41985	41986	41987
41988	41989	41990	41991	41992	41993	41994	41995
41996							

Table 3.4: List of the selected 169 run numbers for Lead.

4

DATA ANALYSIS

Once the reconstruction process is completed, the information is saved as a ROOT file [51], in the standard format of the collaboration, referred to as CLASTOOL format. This format stores the information delivered by each CLAS component in *banks* with different variables each and also provides a preliminary Particle Identification (PID). However, a data reduction software is developed to perform a refined PID and translate the CLASTOOL format into an easily accessible flat tuples format, from which the data analysis of this work will be performed.

This chapter covers the sequential analysis of the data collected by the EG2 experiment with the ultimate goal of multiplicity ratio of the ω meson, R_A^ω, depending on the targets C, Fe, and Pb, and the kinematical variables Q^2, ν, z_h, p_T^2.

This chapter is dedicated to the to identify and count the ω mesons through the final state particles produced from the decay channel

$$\omega \to \pi^+\pi^-\pi^0 \to \pi^+\pi^-\gamma\gamma. \tag{4.1}$$

For this, one must select trigger electrons, charged pions, and photons, whose PID cuts will be detailed in Sections 4.1, 4.2, 4.3, respectively. The scheme to determine from which nuclear target the particles come is explained in Section 4.4. Then, to reduce the background around the ω signal, neutral pions will be reconstructed and selected in Section 4.6, and neutral kaons will be reconstructed and excluded in Section 4.7. The invariant mass difference of the ω will be reconstructed in the Section 4.8. For the presentation of results, the kinematic binning will be decided in Section 4.9. Finally, to extract the ω multiplicities, two background subtraction methods will be described in Section 4.11.

4.1 ELECTRON IDENTIFICATION

The PID of the scattered electron is the most fundamental part of the analysis, as it decides the valid events to study. Most of the cuts described in this section are based on Sebastián Morán's analysis [17, 18].

In the CLASTOOL format, the bank that summarizes all the particles belonging to an event is the EVNT bank, sorting them by arrival time to the detectors. Additionally, the DCPB, CCPB, SCPB, and ECPB banks refer to the parameters measured and delivered by the DC, CC, SC, and EC

detectors, respectively. Each bank presents a variable that allows quantifying the quality or *goodness* of the measurement. This particular kind of variables are referred to as *status words*. The number of rows of each bank represents how many particles left a track on each detector.

The electron is identified as the first particle to be measured by the detectors, being at position or *row* 0 of the EVNT bank. Then, one can demand the measurements to have a minimum quality by specifying cuts on the number of rows and status words of each bank. In summary, the most important status cuts for the electron are as follows:

- It must leave a track in all detectors (DC, CC, SC, EC), i.e., the number of rows for each respective bank must be greater than zero.
- In the DC, the particle must have passed both Time Based Tracking (TBT) and Hit Based Tracking (HTB) during the reconstruction process.

The electron candidates are also required to be negatively charged. This can be determined by the bending direction of the tracks within the DC, caused by the magnetic field of the CLAS toroidal magnet. In contrast, to identify positrons, all the cuts in this section remain the same, except for the charge, which must be positive.

To discard the regions of the DC with low-efficiency, the author of a previous EG2 analysis, L. Zana, described a rigurous method to cut the edges of the DC through different fit functions and parameters. The procedure depends on the type of particle, and its momentum and angular coordinates $(\theta_{lab}, \phi_{lab})$. The proposed cuts are applied on this work and their direct effect is shown in Fig. 4.1. Further information about the DC fiducial cuts can be found at Ref. [49].

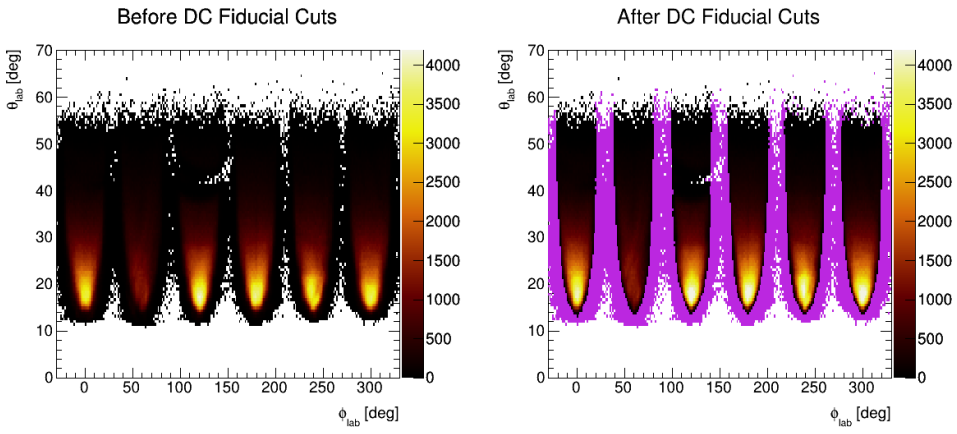

Figure 4.1: Plots of electron candidates's θ_{lab} vs ϕ_{lab} without and with the effect of DC fiducial cuts. Magenta points in the right panel represent the excluded regions.

Moving on to the EC cuts, the generated electromagnetic shower could fall outside the calorimeters, leading to a possible erroneous measurement of the deposited energy. For this, a fiducial cut is applied to remove the detected electrons at the borders of the EC.

$$40 < U < 410 \text{ cm}, \; V < 370 \text{ cm}, \; W < 405 \text{ cm}, \tag{4.2}$$

where UVW are the calorimeter's local coordinates defined in Fig. 3.10. The distributions of UVW are depicted in Fig. 4.2, and the effect of the EC fiducial cuts are shown in Fig. 4.3.

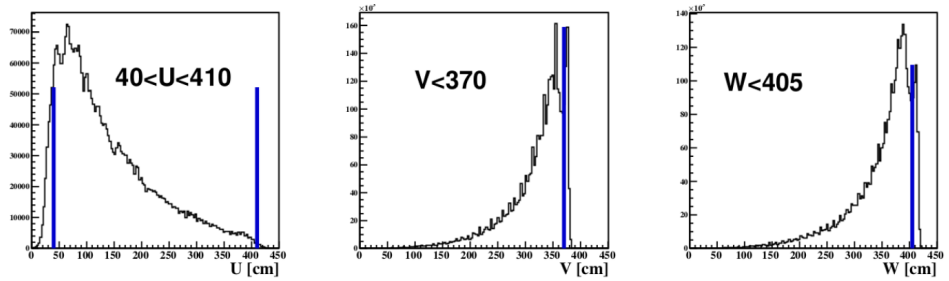

Figure 4.2: Distributions of the electron candidates on the local EC coordinates U, V, and W. Plots taken from Ref. [18].

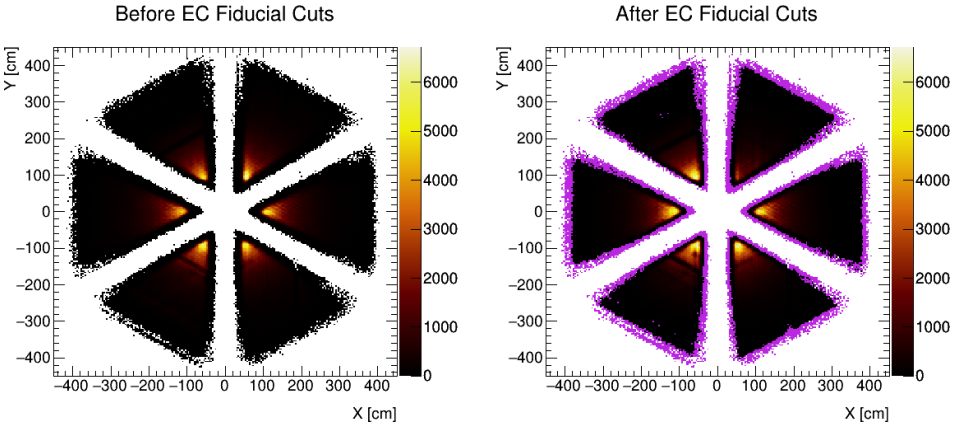

Figure 4.3: Distribution of global coordinates Y_{EC} vs X_{EC} before (left) and after (right) applying the EC fiducial cuts of Eq. 4.2. Magenta points in the right plot represent the discarded electrons.

As explained in Section 3.2.4, E_{in} corresponds to the energy deposited by a particle in the first 5 inner layers of the EC, while E_{out} corresponds to the energy deposited in the 8 outer layers. This information helps differentiate between electrons and negative pions, which are minimum ionizing particles, i.e., they deposit a constant energy fraction in the inner

layers. Therefore, to reject π^-, one can require the following cuts, as seen in Fig. 4.4.

$$E_{out} > 0, \quad \text{and} \quad E_{in} > 0.06 \text{ GeV}. \tag{4.3}$$

Furthermore, the selection of electrons can be improved by specifying correlated energy deposition patterns in the distinct EC layers, depending also on the momentum and sampling fraction factor of 27%. These preliminary sampling fraction cuts are imposed by the following expressions:

$$c_1 p < \frac{E_{in} + E_{out}}{0.27} < c_2 p, \tag{4.4}$$

$$d_1 p + d_2 < \frac{E_{tot}}{0.27} < d_3 p + d_4, \tag{4.5}$$

where E_{tot} corresponds to the energy deposited in all the EC layers. The parameters of both cuts are given by Table 4.1, and their application is described in Fig. 4.5.

Parameter	c_1	c_2	d_1	d_2	d_3	d_4
Value	0.80	1.20	1.15	-0.46	1.15	0.23

Table 4.1: Parameters obtained for Eqs. 4.5 and 4.4 in order to apply electron cuts based on the energy deposited on the different layers of the EC.

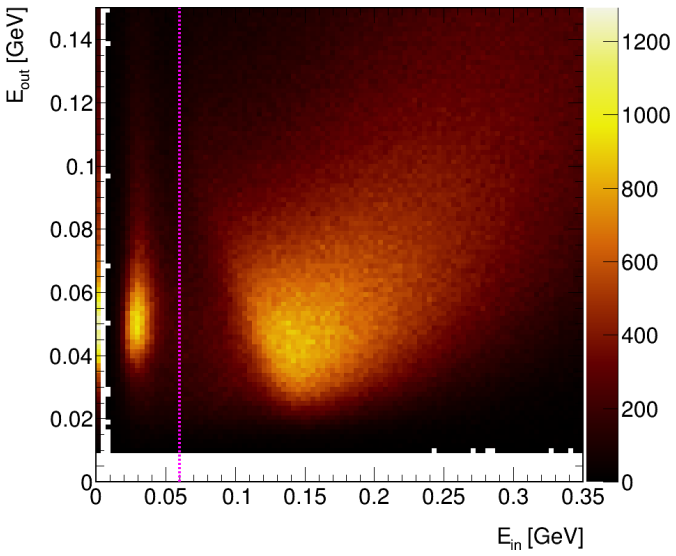

Figure 4.4: Distribution of E_{out} vs E_{in} for electron candidates. All particles located at the right of the vertical line satisfy the cuts of Eq. 4.3.

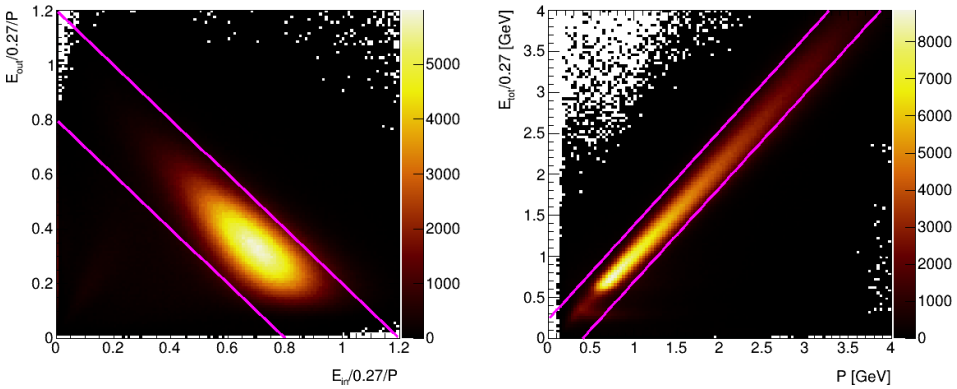

Figure 4.5: Distributions of $E_{out}/0.27/p$ vs $E_{in}/0.27/p$ and $E_{tot}/0.27$ vs momentum of electron candidates. Diagonal magenta lines correspond to cuts described by Equations 4.4 and 4.5, and Table 4.1.

As seen previously, the sampling fraction correspond to the ratio between deposited energy in the EC and the momentum measured by the DC, and it should remain constant at 0.27. But in reality, this ratio depends on the particle's momentum and sector of measurement. Deciding the electron candidate's energy to be $E = \max(E_{in} + E_{in}, E_{tot})$, one can refine the preliminary cuts of Eqs. 4.4 and 4.5 by additionally imposing the following sampling fraction cut:

$$\left| \frac{E}{p} - \mu(p) \right| > 2.5\,\sigma(p), \tag{4.6}$$

where $\mu(p)$ and $\sigma(p)$ are two momentum-dependent functions, with parameters that depend on the sector and target system, given by Tables 4.2, 4.3, and 4.4.

$$\mu(p) = a_1 + a_2 p + a_3 p^2, \tag{4.7}$$

$$\sigma(p) = \sqrt{b_1^2 + \frac{b_2^2}{p}}. \tag{4.8}$$

The models for these functions come from the respective CLAS and EC simulations and calibrations in [12] and [42]. The fitting procedure for the present dataset was performed by Taisiya Mineeva [20] and updated by Sebastián Morán [18]. Figure 4.6 illustrates the application of the sampling fraction cuts on E/p vs p distributions of electrons for each CLAS sector.

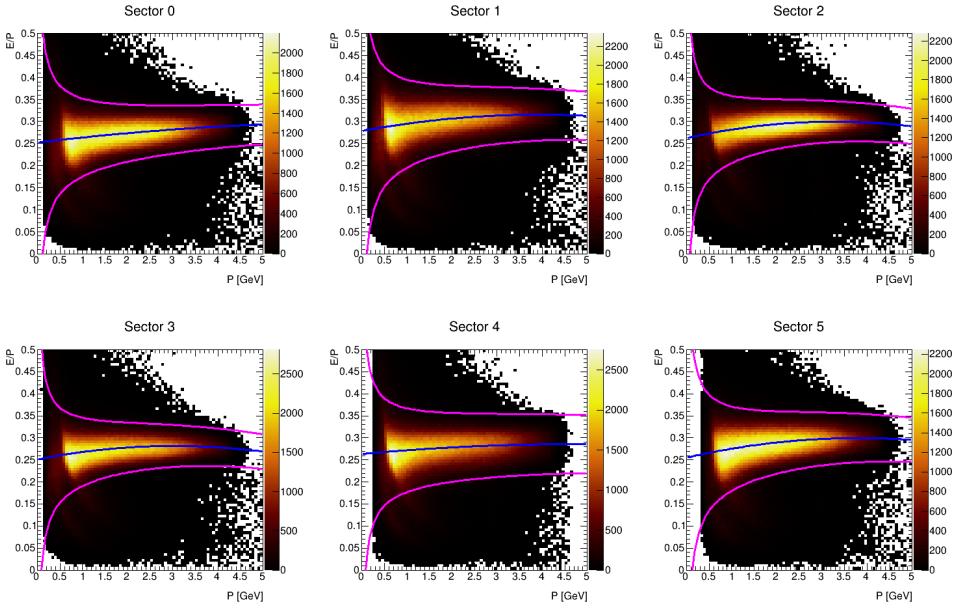

Figure 4.6: Plots of E/p vs p for each CLAS sector for C data. Central blue curve corresponds to $\mu(p)$ and magenta curves correspond to sampling fraction cuts $\mu \pm 2.5\sigma$, according to Eqs. 4.6, 4.7, and 4.8.

Sector \ Coef.	a_1	a_2	a_3	b_1	b_2
Sector 1	2.52×10^{-1}	1.2×10^{-2}	-7.93×10^{-4}	9.551×10^{-3}	3.406×10^{-2}
Sector 2	2.78×10^{-1}	1.8×10^{-2}	-2.0×10^{-3}	1.39×10^{-2}	3.748×10^{-2}
Sector 3	2.62×10^{-1}	2.3×10^{-2}	-3.5×10^{-3}	9.32×10^{-3}	2.94×10^{-2}
Sector 4	2.58×10^{-1}	2.0×10^{-2}	-3.0×10^{-3}	8.21×10^{-3}	2.99×10^{-2}
Sector 5	2.66×10^{-1}	9.0×10^{-3}	-1.0×10^{-3}	2.25×10^{-2}	3.06×10^{-2}
Sector 6	2.55×10^{-1}	2.3×10^{-2}	-3.0×10^{-3}	1.17×10^{-2}	3.64×10^{-2}

Table 4.2: Parameters extracted from fit on carbon data, for sampling fraction cut on electrons identification. Courtesy from Ref. [18].

Sector \ Coef.	a_1	a_2	a_3	b_1	b_2
Sector 1	2.224×10^{-1}	2.20×10^{-2}	-3.0×10^{-3}	9.230×10^{-3}	2.983×10^{-2}
Sector 2	2.34×10^{-1}	1.9×10^{-2}	-2.0×10^{-3}	8.663×10^{-3}	3.080×10^{-2}
Sector 3	2.52×10^{-1}	2.4×10^{-2}	-3.3×10^{-3}	1.070×10^{-2}	2.630×10^{-2}
Sector 4	2.50×10^{-1}	2.00×10^{-2}	-3.0×10^{-3}	7.28×10^{-3}	2.98×10^{-2}
Sector 5	2.71×10^{-1}	1.18×10^{-2}	-1.8×10^{-3}	1.841×10^{-2}	3.480×10^{-2}
Sector 6	2.52×10^{-1}	2.2×10^{-2}	-3.0×10^{-3}	4.115×10^{-3}	3.551×10^{-2}

Table 4.3: Parameters extracted from fit on iron data, for sampling fraction cut on electrons identification. Courtesy from Ref. [18].

Sector \ Coef.	a_1	a_2	a_3	b_1	b_2
Sector 1	2.531×10^{-1}	1.31×10^{-2}	-1.0×10^{-3}	7.67×10^{-3}	3.54×10^{-2}
Sector 2	2.49×10^{-1}	1.47×10^{-2}	-1.0×10^{-3}	7.52×10^{-3}	3.38×10^{-2}
Sector 3	2.54×10^{-1}	2.2×10^{-2}	-3.0×10^{-3}	8.13×10^{-3}	2.77×10^{-2}
Sector 4	2.55×10^{-1}	1.9×10^{-2}	-3.0×10^{-3}	7.20×10^{-3}	3.04×10^{-2}
Sector 5	2.76×10^{-1}	1.1×10^{-2}	-1.7×10^{-3}	1.80×10^{-2}	3.53×10^{-2}
Sector 6	2.62×10^{-1}	1.9×10^{-2}	-2.0×10^{-3}	1.99×10^{-3}	3.76×10^{-2}

Table 4.4: Parameters extracted from fit on lead data, for sampling fraction cut on electrons identification. Courtesy from Ref. [18].

When selecting electrons, a standard solution to reduce negative pions contamination requires a minimum amount of photoelectrons emitted by the particle within the CC. As seen in Fig. 4.7, there is a prominent peak at low number of photoelectrons emitted, expected from minimum ionizing particles such as low energy π^-. To remove these particles, a sector-dependent cut is implemented:

$$10N_{phe} > \begin{cases} 25, & \text{Sector 1 or Sector 2} \\ 26, & \text{Sector 3} \\ 21, & \text{Sector 4} \\ 28, & \text{Sector 5 or Sector 6} \end{cases} \tag{4.9}$$

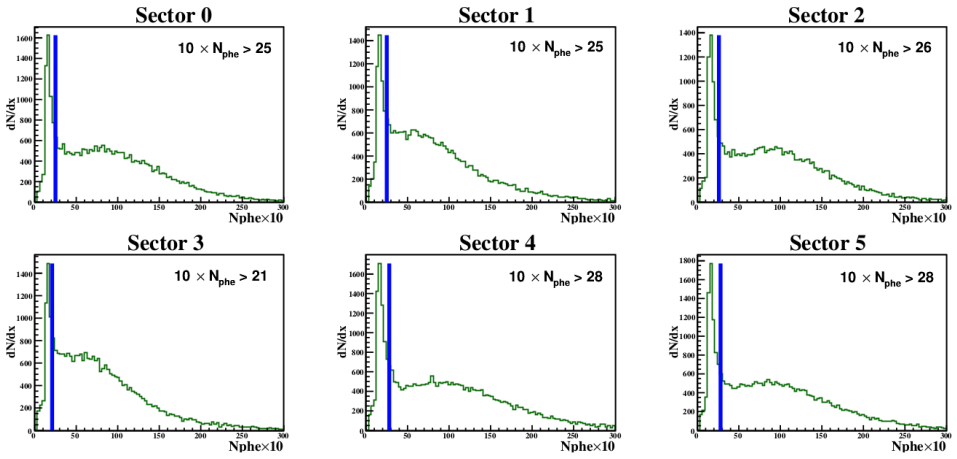

Figure 4.7: Distribution of number of photoelectrons (×10) emitted by electron candidates in each CLAS sector. Vertical blue lines correspond to the cut applied to reject π^-. Plots taken from Ref. [18].

As a final cut, one can prevent the misidentification of electrons with other particles by imposing a coincidence cut, that demands a certain difference between the measured time by the EC and the TOF counters.

$$\Delta T \equiv \left| t_{EC} - t_{SC} - \frac{1}{c}(l_{EC} - l_{SC}) \right| < 5\sigma, \tag{4.10}$$

where t_{EC} and t_{SC} correspond to the arrival time measured by the EC and SC, l_{EC} and l_{SC} to the determined path lengths, $c = 30$ cm/ns, and $\sigma = 0.35$ ns is the width parameter of the Gaussian determined by a previous fit of the ΔT distribution. Fig. 4.8 represents the distribution of the defined ΔT variable and the applied coincidence cuts.

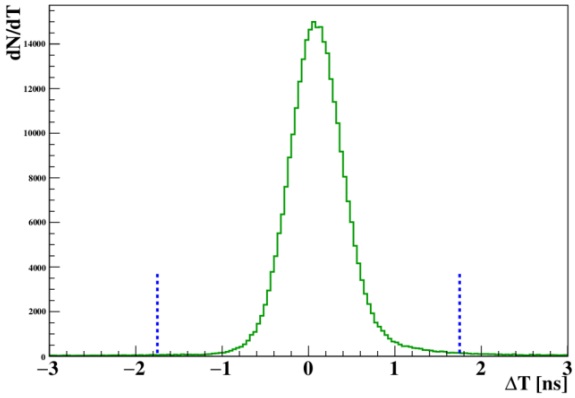

Figure 4.8: Distribution of the variable ΔT defined in Eq. 4.10 for electron candidates. Blue vertical lines represent the coincidence cut between EC and SC time measurements. Plot taken from Ref. [18].

4.2 CHARGED PIONS IDENTIFICATION

After the identification of the trigger electrons that define each event, the next logical step is to identify all the final-state particles produced by each event. Considering the decay described by Eq. 4.1, this section will detail the PID scheme to identify charged pions, π^+ and π^-. Most of the PID cuts for both pions are based on Sebastián Morán's analysis on the electroproduction of charged pions off nuclei from this same dataset [17, 18].

4.2.1 π^+ Identification

The first step to identify positive pions π^+ is to require a good measurement of the signal by the DC. For that, the particle must have left a track in the DC and have passed the Time Based Tracking (TBT) and Hit Based Tracking (HTB) during the reconstruction process. Then, based on

its bending direction, the particle is required to have positive electrical charge.

After selecting positive particles, the main cut to identify the kind of particle depends on the TOF measurements. However, due to limitations on the detector's resolution [41], it becomes more difficult to differentiate the kind of particle at $p > 2.7$ GeV [18]. This implies that a distinction must be made: low-energy π^+ with $p < 2.7$ GeV will be identified directly from the TOF measurements, while high-energy π^+ with $p > 2.7$ GeV will be determined by using the CC.

For the first category of low-momentum π^+ candidates, the following corrected TOF variable will be crucial:

$$\Delta T = \left(\frac{l_{SC}^{e^-}}{c} - \frac{l_{SC}^{\pi^+}}{v^{\pi^+}} \right) - \left(t_{SC}^{e^-} - t_{SC}^{\pi^+} \right), \tag{4.11}$$

where l_{SC} and t_{SC} correspond to each particle's path lengths and Time of Flight (TOF) from the interaction vertex to the SC, respectively. $c = 30$ cm/ns is the speed of light in vacuum, and v^{π^+} is the velocity of the positive pion candidate, derived from the β measured by SC. A positive particle is identified as a π^+ if it belongs to particular values of ΔT depending on specific momentum ranges, as depicted in Figure 4.9 and detailed in Table 4.5.

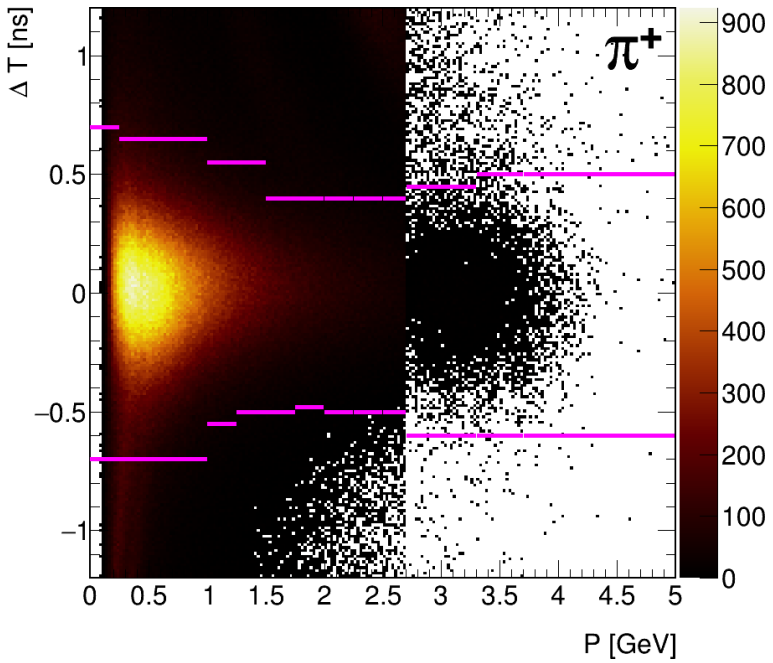

Figure 4.9: Plot of ΔT vs momentum of π^+ candidates. Horizontal lines represent ΔT cut to identify π^+, according to Table 4.5. Discontinuity in $p = 2.7$ GeV represents the change of PID method from TOF to CC.

Considering β as the reconstructed velocity[1] given by the SC and the momentum p measured by the DC, one can reconstruct the square of the particles' invariant mass as:

$$m^2_{SC} = p^2 \left(\frac{1}{\beta^2_{meas}} - 1 \right), \tag{4.12}$$

which is useful to improve the TOF cuts on certain p values, as seen in Table 4.6.

For the second category of high-momentum positive particles with $p > 2.7$ GeV, the CC measurements are used. Reliable status cuts from the CC are required. At this energy levels, massive particles, such as kaons and protons, do not produce photoelectrons as they cannot surpass the speed of light in the medium. Therefore, one can restrict the π^+ to satisfy:

$$10 N_{phe} > 25 \tag{4.13}$$

Despite the use of CC measurements, and to maintain a consistent selection in the entire p spectrum, ΔT (Eq. 4.11) cuts are also applied on particles with $p > 2.7$ GeV. These ranges appear in Fig. 4.9 and Table 4.5.

Momentum range (GeV)	Corr. Time of Flight (ns)
$0.00 < P \leq 0.25$	$-1.45 \leq \Delta T < 1.05$
$0.25 < P \leq 0.50$	$-1.44 \leq \Delta T < 1.05$
$0.50 < P \leq 0.75$	$-1.44 \leq \Delta T < 1.05$
$0.75 < P \leq 1.00$	$-1.40 \leq \Delta T < 1.05$
$1.00 < P \leq 1.25$	$-1.35 \leq \Delta T < 1.03$
$1.25 < P \leq 1.50$	$-1.35 \leq \Delta T < 0.95$
$1.50 < P \leq 1.75$	$-1.35 \leq \Delta T < 0.87$
$1.75 < P \leq 2.00$	$-1.25 \leq \Delta T < 0.68$
$2.00 < P \leq 2.25$	$-0.95 \leq \Delta T < 0.65$
$2.25 < P \leq 2.50$	$-1.05 \leq \Delta T < 0.61$
$2.50 < P \leq 2.70$	$-1.05 \leq \Delta T < 0.61$
$2.70 < P \leq 3.30$	$-0.60 \leq \Delta T < 0.45$
$3.30 < P \leq 3.70$	$-0.60 \leq \Delta T < 0.50$
$3.70 < P \leq 5.00$	$-0.60 \leq \Delta T < 0.50$

Table 4.5: TOF cuts on ΔT to identify π^+ on certain momentum ranges. Values taken from Ref. [18].

1 Velocity relative to the speed of light, $\beta = v/c$.

Momentum range (GeV)	m^2_{SC} Range (GeV)
$2.25 < P \leq 2.50$	$m^2_{SC} < 0.5$
$2.50 < P \leq 2.70$	$m^2_{SC} < 0.4$

Table 4.6: Cuts on m^2_{SC}, defined in Eq. 4.12, to identify π^+ at certain momentum regions. Values taken from Ref. [18].

4.2.2 π^- Identification

The PID scheme of negative pions π^- is similar to the selection cuts of π^+. The candidate particles must have left a track in the DC and pass both Time Based Tracking (TBT) and Hit Based Tracking (HTB). Plus, they must satisfy particular momentum-dependent cuts on the TOF variable ΔT, defined in Eq. 4.11. The selection is illustrated in Fig. 4.10 and detailed in Table 4.7.

Regarding the differences between both π^- and π^+ PID methods, the most trivial one is that negative pions must have a negative charge. Moreover, no CC technique is employed to identify π^-, i.e., they are identified only by using TOF measurements along the entire momentum spectrum up to 5 GeV. This upper limit in momentum is set to prevent the misidentification of non-interacting electrons as π^-.

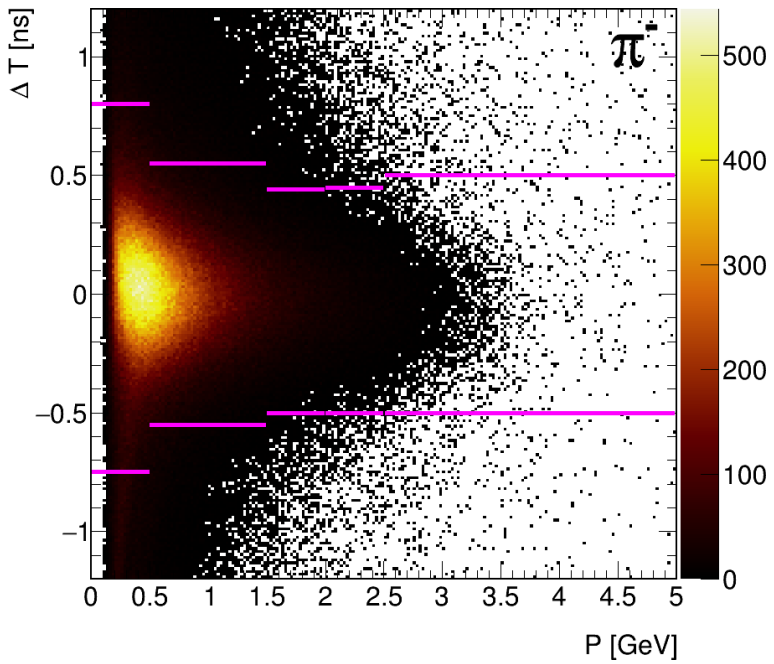

Figure 4.10: Plot of ΔT vs momentum of π^- candidates. Horizontal lines represent ΔT cut to identify π^-, according to Table 4.7

.

Momentum range (GeV)	Corr. Time of Flight (ns)
$0.00 < P \leq 0.50$	$-0.75 \leq \Delta T < 0.80$
$0.50 < P \leq 1.00$	$-0.55 \leq \Delta T < 0.55$
$1.00 < P \leq 1.50$	$-0.55 \leq \Delta T < 0.55$
$1.50 < P \leq 2.00$	$-0.50 \leq \Delta T < 0.44$
$2.00 < P \leq 2.50$	$-0.50 \leq \Delta T < 0.45$
$2.50 < P \leq 5.00$	$-0.50 \leq \Delta T < 0.50$

Table 4.7: TOF cuts on ΔT to identify π^-. Values taken from Ref. [18].

In conclusion, the PID of negative pions is less restrictive and more straightforward than positive pions'. Less restrictive because the multiplicity of π^- is lower, and more straightforward because the contamination of negative kaons K^- and anti-protons $\bar{p}$ is found to be relatively small [16], hence the use of CC measurements would reduce the statistics instead of improving the identification [18].

4.3 PHOTON IDENTIFICATION

As seen in Section 2.12 and as it will be seen in Section 4.6, the ω meson decays immediately into a π^0, which immediately decays into 2γ. For this, the photons PID is described in this section, where all cuts are based on a previous EG2 analysis performed by Taisiya Mineeva on the hadronization of the π^0 [20].

Unlike charged particles, photons will leave almost no track inside the DC and no track inside the CC because the PMTs of the CC are unable to measure photons at these energy levels. Therefore, photons only leave hits inside the EC, which measurements will become the primary source of information.

As a first restriction, photons must have neutral charge. Similarly to electrons, fiducial cuts must be applied to prevent low-efficiency detections at the border of the calorimeters. The cuts applied are depicted in Fig. 4.11 and correspond to:

$$40 < U < 410 \text{ cm}, \; V < 370 \text{ cm}, \; W < 410 \text{ cm}. \tag{4.14}$$

Another electrically neutral particle with a high level of occurrence is the neutron. To differentiate between neutrons and photons, and under the assumption that measured photon's speed is the speed of light $c = 30$ cm/ns, one can construct an EC coincidence time distribution to test the

EC's resolution on β, while also preventing some faulty photons. The cut applied to this distribution is depicted in 4.12, and is expressed as:

$$-2.2 < t_{EC} - t_{start} - l_{EC}/c < 1.3 \text{ ns}, \tag{4.15}$$

where t_{EC} and l_{EC} are flight time and the path length from the target to the EC, and t_{start} is the event start time.

The design of CLAS forward electromagnetic calorimeters allow for the detection of photons at energies above 200 MeV [12]. Thus, photons are kinematically constrained to have above 200 MeV of deposited energy in the EC.

$$E_\gamma \equiv \frac{\max(E_{tot}, E_{in} + E_{out})}{0.273} > 0.2 \text{ GeV}, \tag{4.16}$$

where the 0.273 factor corresponds to the sampling fraction of the photons, which is defined as the ratio of deposited energy in the EC to the momentum determined by the DC, and given as a parameter in the reconstruction algorithm [42].

Subsequently, to cover systematic uncertainties due to the double-target design and as a way to bring the π^0 mass closer to the global value measured by the Particle Data Group (PDG), the energy of the photons can be corrected. This can be achieved by setting a sampling fraction of 0.273 and comparing the π^0 invariant mass with its PDG value, in the moment of its reconstruction. This method is repeated until both photons π^0 have the same correction factor. The correction factors k were already measured in Ref. [20], where detailed steps of the method can be found, and they are applied as:

$$E'_\gamma = \frac{E_\gamma}{k}, \tag{4.17}$$

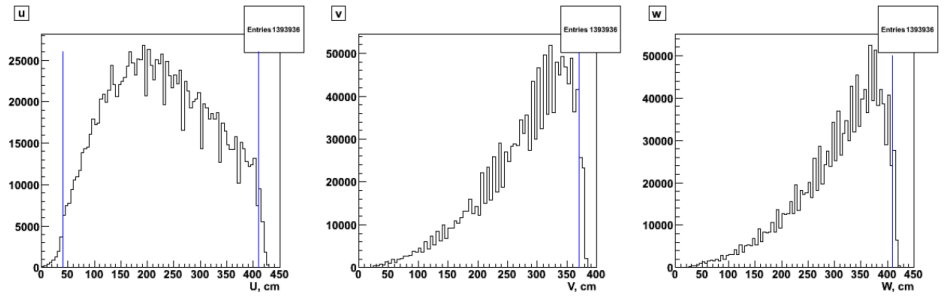

Figure 4.11: Distributions of the photon candidates on the local EC coordinates U, V, and W. Blue vertical lines represent the EC fiducial cuts to identify photons, expressed in Eq. 4.14. Plot taken from Ref. [20].

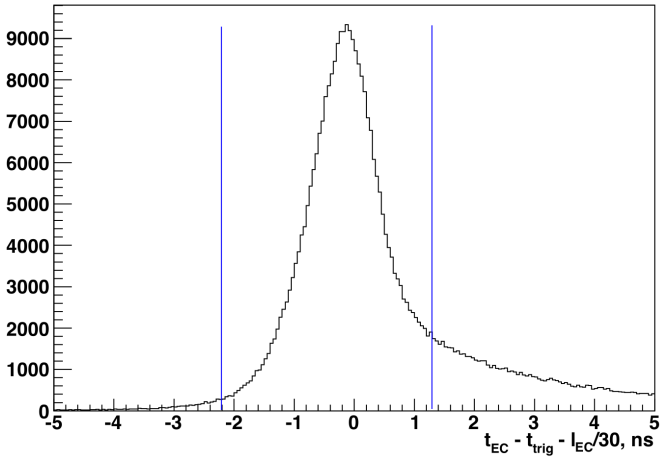

Figure 4.12: EC coincidence time distribution. Vertical lines represent the cut to select photons as in Eq. 4.15. Plot taken from Ref. [20].

where E'_γ is the corrected photon energy, E_γ is the energy defined in Eq. 4.16, and k is the correction factor that depends on the uncorrected energy:

$$k(E_\gamma) = k_1 + \frac{k_2}{E_\gamma} + \frac{k_3}{E_\gamma^2}, \tag{4.18}$$

for which parameters k_1, k_2, and k_3 depend on the experimental run and are detailed in Table 4.8.

Experimental run	k_1	k_2	k_3
D+C	1.129	-5.793×10^{-2}	1.07×10^{-12}
D+Fe	1.116	9.213×10^{-2}	1.007×10^{-2}
D+Pb	1.129	-5.793×10^{-2}	1.07×10^{-12}

Table 4.8: Parameters of the photon's energy correction factors. Values taken from Ref. [20].

Regarding photon's momentum, each component is corrected and derived from the position of the neutral hit in the EC and the corrected energy E'_γ:

$$\begin{aligned} p'_x &= E'_\gamma \sin(\theta_{EC}) \cos(\phi_{EC}), \\ p'_y &= E'_\gamma \sin(\theta_{EC}) \sin(\phi_{EC}), \\ p'_z &= E'_\gamma \cos(\theta_{EC}), \end{aligned} \tag{4.19}$$

where θ_{EC} and ϕ_{EC} are the angular components of the direction of the photon traced from the z-corrected vertex of the electron to the position of the neutral hit in the EC [20].

As a final constraint for the photons, it is also necessary to discard possible bremsstrahlung photons. According to the angular peak approximation proposed by the theoretical work of Ref. [52], most bremsstrahlung photons are emitted in the direction of the incoming or scattered electron. To address this, one can define the angle $\alpha_{e\gamma}$ as the angle between the measured photon's and the scattered electron's directions and apply the following cut, as represented by Fig. 4.13:

$$\alpha_{e\gamma} > 12^{\circ}. \tag{4.20}$$

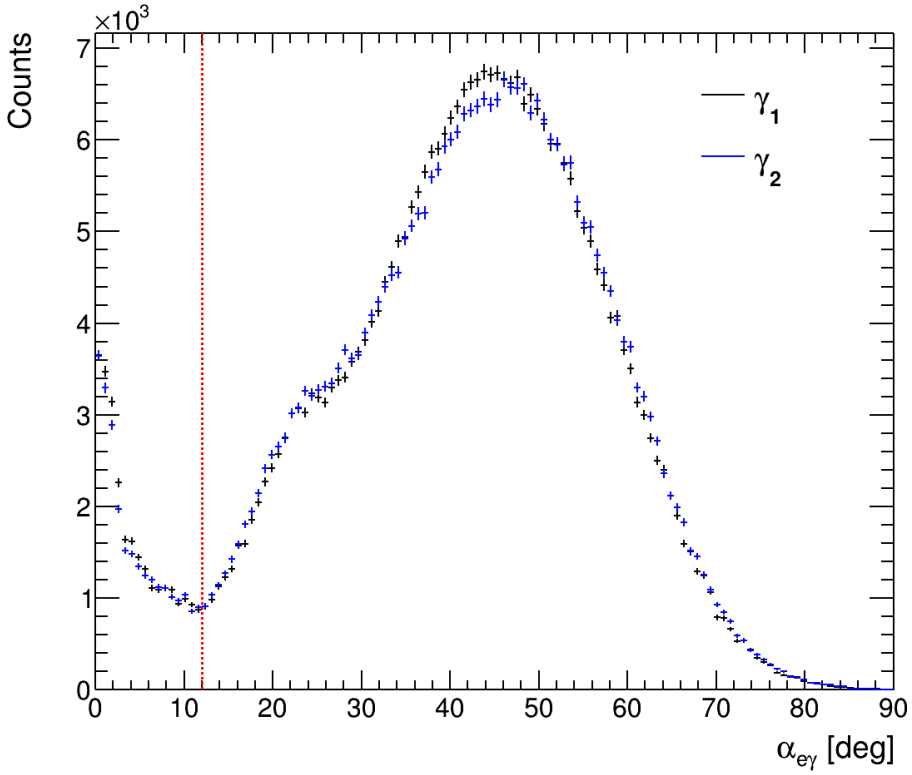

Figure 4.13: Distribution of the angle $\alpha_{e\gamma}$ between the scattered electron's direction with the direction of each photon that form a π^0 candidate. Red vertical line represents the $\alpha_{e\gamma} > 12^{\circ}$ cut.

4.4 TARGET DETERMINATION

During the running period of the EG2 experiment, two targets were simultaneously positioned in the beamline. Considering z as the beam axis, where $z = 0$ corresponds to the geometrical center of the CLAS, the center of the liquid deuterium target was placed at $z = -30$ cm and the center of the solid target A, which could be carbon, iron or lead, was placed at $z = -25$ cm.

To differentiate between the two nuclear targets and remove some background, it is necessary to determine the origin of the particles. This can be achieved by reconstructing the tracking of the position of the interaction vertex, depending on the sector it was detected, the particle's direction and assuming that the ideal beam position is at $(x, y) = (0, 0)$. However, the vertex reconstruction must be corrected by taking into account the displacement of the actual beam position: $(x, y) = (-0.043, 0.33)$ cm, which was calculated using the proton elastic scattering reaction. Considering this new beam position, a reverse engineering process can be performed to triangulate the corrected position of each vertex [20]. After the correction, the new electron vertex z^{corr} is aligned and is independent of the sector number, as shown in Fig. 4.14.

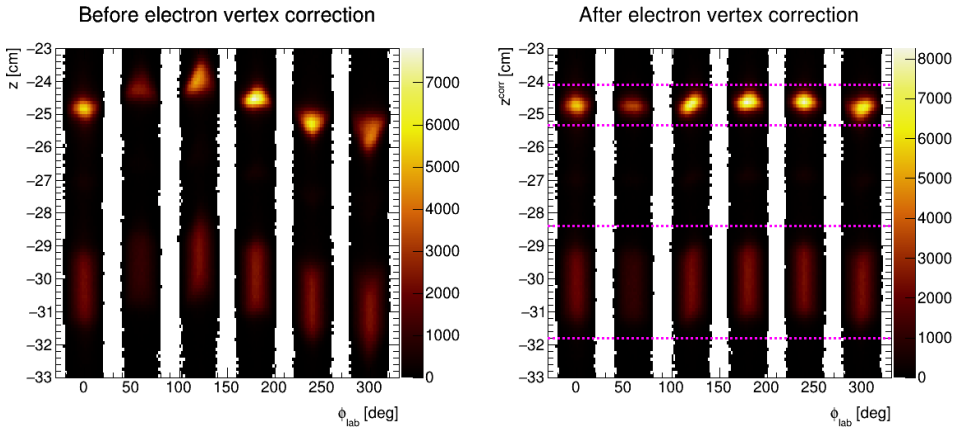

Figure 4.14: Electron z-vertex vs ϕ_{lab} before (left) and after (right) vertex correction. In right panel, upper horizontal lines represent cut to select solid target events, and bottom horizontal lines represent cut to select deuterium events.

The distinction of each target is performed by fitting the z^{corr} distributions around the expected target positions, as performed in Fig. 4.16. Then, a $\langle z^{corr} \rangle \pm 3\sigma$ cut is applied for each target. The boundary values are shown in Fig. 4.15 and given by the following expressions,

$$-31.80 < z_D^{corr} < -28.40 \text{ cm} \tag{4.21}$$

$$-25.65 < z_{Fe}^{corr} < -24.26 \text{ cm} \tag{4.22}$$

$$-25.33 < z_C^{corr} < -24.10 \text{ cm} \tag{4.23}$$

$$-25.54 < z_{Pb}^{corr} < -24.36 \text{ cm} \tag{4.24}$$

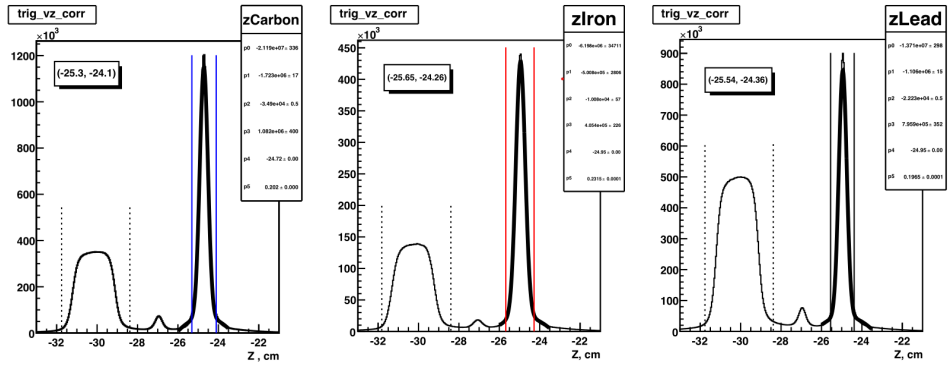

Figure 4.15: Electron z^{corr} vertex distributions. The dashed vertical lines correspond to the liquid deuterium targets (Eq 4.21). The blue, red and black solid vertical lines correspond to Iron (Eq 4.22), Carbon (Eq 4.23) and Lead (Eq 4.24), respectively. Plot taken from Ref. [20].

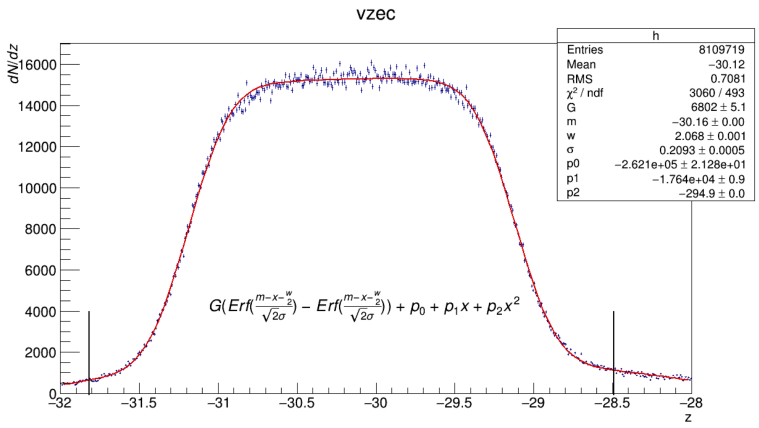

Figure 4.16: Fit to the electron z^{corr} vertex distributions for the deuterium target. Fit function given in the plot. Vertical lines represent the $\langle z^{corr} \rangle \pm 3\sigma$ cut. Fit perfomed by Orlando Soto. Plot taken from Ref. [20].

On the other hand, the y-position of the target has an usually poorer reconstruction than the z-vertex because of the positioning of the stereo wires. Therefore, in order to reject the underlying background [17], a cut was applied to the y^{corr} for both liquid and solid targets:

$$|y^{corr}| < 1.4 \text{ cm}. \tag{4.25}$$

It is unnecessary to apply a cut to x^{corr}, as it is already determined upon the reconstruction of the y-vertex.

4.5 KINEMATICAL REGION

To select events according to the DIS regime, one can impose the following kinematical cuts to the trigger electron:

$$Q^2 > 1\ \text{GeV}^2, \quad W > 2\ \text{GeV}, \quad y_B < 0.85. \tag{4.26}$$

These cuts are depicted in Figure 4.17 and are justified by the following arguments:

- $Q^2 > 1\ \text{GeV}^2$, to demand the necessary virtuality of the virtual photon to probe the nuclear substructure.
- $W > 2$ GeV, to exclude nucleon resonances, as seen previously in Fig. 2.6.
- $y_B < 0.85$, to limit the magnitude of the radiative corrections, based on previous HERMES analyses [9–11].

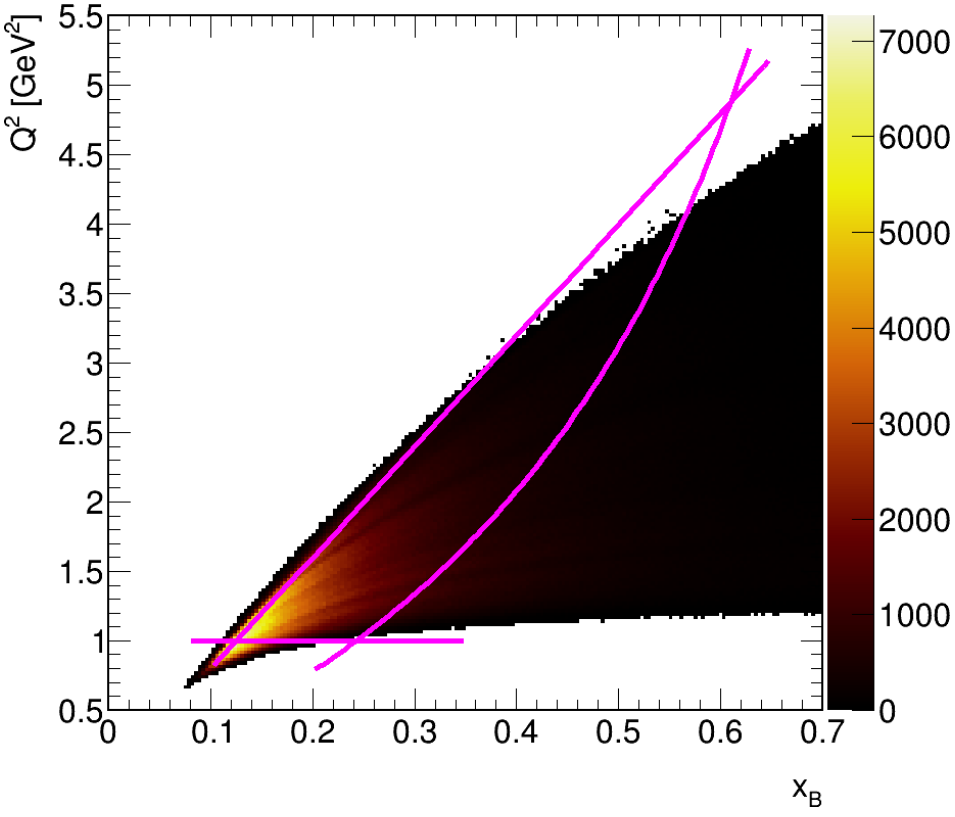

Figure 4.17: Representation of the kinematical cuts for the DIS regime in a (Q^2, x_B) phase space.

4.6 NEUTRAL PION RECONSTRUCTION

Once the scattered electron and the photons are properly identified, it is possible to identify the π^0. However, unlike charged pions, the neutral pion π^0 has a very short lifetime, of about 8.5×10^{-17} s [22], which cannot be measured directly. Therefore, the reconstruction of the π^0 invariant mass must be performed considering its main decay channel, with a branching ratio of $\sim 98.8\%$ [22]:

$$\pi^0 \to \gamma\gamma. \tag{4.27}$$

Selecting events with at least 2γ in their final state and combining all possible pairs, let p_{γ_1} and p_{γ_2} be the four-momentum of two photons from the same event. Then, the four-momentum of the pair, or π^0 candidate, would correspond to:

$$p_{\gamma\gamma} = p_{\gamma_1} + p_{\gamma_2} = (E_{\gamma_1} + E_{\gamma_2}, \vec{p}_{\gamma_1} + \vec{p}_{\gamma_2})\,. \tag{4.28}$$

The π^0 candidate will have an invariant mass that can be reconstructed as:

$$m^2_{\gamma\gamma} = p_{\gamma\gamma} \cdot p_{\gamma\gamma} = 2E_{\gamma_1}E_{\gamma_2}\left(1 - \frac{\vec{p_{\gamma_1}} \cdot \vec{p_{\gamma_2}}}{E_{\gamma_1}E_{\gamma_2}}\right). \tag{4.29}$$

Considering that $m_\gamma = 0$ and defining $\cos\theta_{12}$ as the cosine of the opening angle between both photons,

$$\cos\theta_{12} = \frac{\vec{p_{\gamma_1}} \cdot \vec{p_{\gamma_2}}}{E_{\gamma_1}E_{\gamma_2}}, \tag{4.30}$$

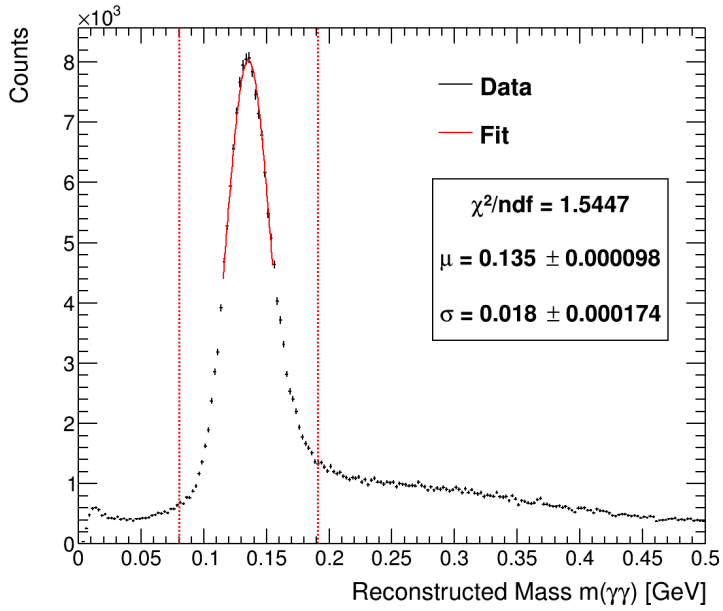

Figure 4.18: Gaussian fit around π^0 invariant mass. Vertical lines represent the $\mu \pm 3\sigma$ cut. Obtained μ is in agreement with PDG value [22].

the invariant mass of the π^0 can be rewritten as:

$$m_{\gamma\gamma} = \sqrt{2E_{\gamma_1}E_{\gamma_2}\,(1-\cos\theta_{12})}. \tag{4.31}$$

Figure 4.18 represents the reconstructed invariant mass of the π^0, which presents a clear peak in the expected π^0 signal [22]. To cut some of the background, a Gaussian function fit is made in the signal region, and from the obtained parameters, a $\mu \pm 3\sigma$ cut is further applied:

$$0.059 < m_{\gamma\gamma} < 0.204 \text{ GeV}. \tag{4.32}$$

4.7 EXCLUSION OF NEUTRAL KAONS

A previous analysis done on this same data set, Ref. [14], studied the hadronization of the short-lived neutral kaon K^0_S, which decays into a $\pi^+\pi^-$ pair. Therefore, under the evidence that there are neutral kaons, a procedure must be performed to exclude them in the reconstruction of the ω candidates.

To find the neutral kaons, the four-momentum of a 2-particle system must be defined:

$$p_{12} = p_1 + p_2 = (E_1 + E_2,\, \vec{p_1} + \vec{p_2})\,, \tag{4.33}$$

where E_i and p_i is the energy and momentum of the particle i, respectively. Then, the square of the system's invariant mass m^2_{12} can be expressed as:

$$m^2_{12} = p_{12}\cdot p_{12} = m_1^2 + m_2^2 + 2E_1E_2 - 2\vec{p_1}\cdot\vec{p_2}. \tag{4.34}$$

Considering a system consisting of a pair $\pi^+\pi^-$, this can be rewritten as follows,

$$m^2_{\pi^+\pi^-} = 2M^2_{\pi^\pm} + 2E_{\pi^+}E_{\pi^-} - 2(p_x^{\pi^+}p_x^{\pi^-} + p_y^{\pi^+}p_y^{\pi^-} + p_z^{\pi^+}p_z^{\pi^-}). \tag{4.35}$$

In the present analysis, since the mass of the pions is fixed and not reconstructed, the value $M_{\pi^\pm} = 0.13957$ GeV corresponds to the invariant mass of the pions according to the PDG, [22]. The distribution of this expression is shown in the left panel of Fig. 4.19.

What follows is the same as for selecting neutral pions, but this time, the aim is to exclude the neutral kaons. A Gaussian function fit is made on the expected signal of the K^0_S [22]. Finally, based on the obtained parameters, the opposite of a $\mu \pm \sigma$ cut is applied:

$$m^2_{\pi^+\pi^-} < 0.233 \text{ GeV} \quad \text{or} \quad m^2_{\pi^+\pi^-} > 0.261 \text{ GeV}. \tag{4.36}$$

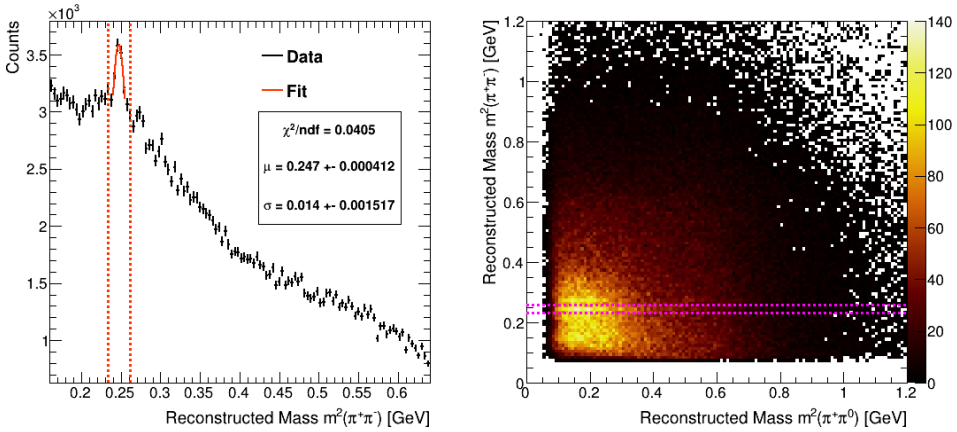

Figure 4.19: Plots that represent the K_S^0 exclusion cut. In the left panel, the distribution $m^2_{\pi^+\pi^-}$ is fitted with a gaussian function (red curve), where vertical lines represent the $(\mu \pm \sigma)$ cut. In the right panel, $m^2_{\pi^+\pi^-}$ vs $m^2_{\pi^+\pi^0}$ is plotted, horizontal lines represent the same $(\mu \pm \sigma)$ excluded band.

4.8 OMEGA RECONSTRUCTION

As stated in the beginning of the chapter, the ω meson primarily decays into the three pions, from which the π^0 subsequently decays into two photons,

$$\omega \to \pi^+\pi^-\pi^0 \to \pi^+\pi^-\gamma\gamma. \tag{4.37}$$

Therefore, to reconstruct the ω meson through this channel, all the events that have at least $1\pi^+$, $1\pi^-$ and 2γ in their final state are selected, in addition to the scattered electron. From this selection, all the possible combinations of ω will be stored and referred to as ω candidates. The total number of ω candidates per event is given by:

$$N_\omega^{comb} = \binom{N_{\pi^+}}{1}\binom{N_{\pi^-}}{1}\binom{N_\gamma}{2}, \tag{4.38}$$

where N_π^+, N_π^-, and N_γ are the number of π^+, π^- and γ from a same event, respectively.

Considering the ω as a 3-particle system, one can define its four-momentum as follows,

$$p_\omega = p_{\pi^+} + p_{\pi^-} + p_{\gamma\gamma} = (E_{\pi^+} + E_{\pi^-} + E_{\gamma\gamma},\ \vec{p}_{\pi^+} + \vec{p}_{\pi^-} + \vec{p}_{\gamma\gamma}), \tag{4.39}$$

being $p_{\gamma\gamma}$ the four-momentum of the reconstructed π^0, as stated in Eq. 4.28. In a similar way, the reconstructed invariant mass of the ω meson is expressed as:

$$m_{\pi^+\pi^-\pi^0} = \sqrt{(E_{\pi^+} + E_{\pi^-} + E_{\gamma\gamma})^2 - (\vec{p}_{\pi^+} + \vec{p}_{\pi^-} + \vec{p}_{\gamma\gamma})^2}. \tag{4.40}$$

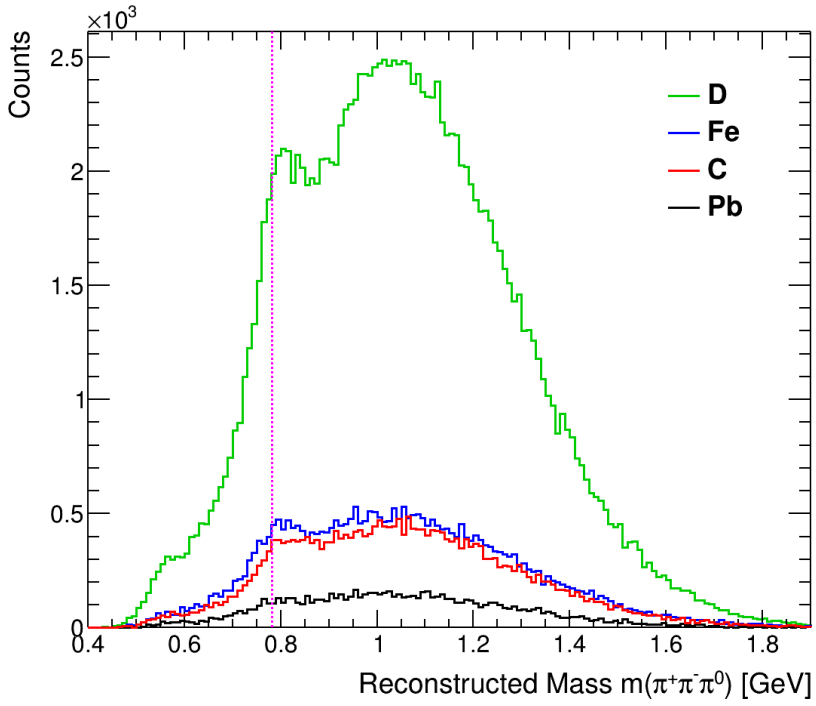

Figure 4.20: Invariant mass distributions of the reconstructed ω mesons from all targets. Green curve corresponds to the data collected from deuterium, blue curve to iron, red curve to carbon, and black curve to lead. Magenta vertical line represents the PDG value of the ω mass, $M_\omega = 0.782$ GeV [22].

The standard method to extract the number of *real* ω mesons is to integrate the distribution $m_{\pi^+\pi^-\pi^0}$ in the expected ω signal region, i.e. a pronounced peak in $M_\omega = 0.782$ GeV [22]. However, as shown in Fig. 4.20, a gaussian-shaped background is present throughout the invariant mass spectrum, and the signal/noise ratio is consequently low.

There is, however, an alternative method to deal with the ω meson's poor signal, widely used by other experimental collaborations in high-energy physics [53–56]. The technique exploits the fact that two or more invariant masses can be defined due to two or more consecutive decays. For example, in the simplest ideal case $P_1 \to P_A P_2 \to P_A P_B P_C$, where P_2 decayed into P_B and P_C, the difference between the invariant mass distributions $m(ABC) - m(BC)$ is also a Lorentz invariant and must be equal to the difference between the expected values $M(1) - M(2)$. Therefore, this new mass difference distribution should exhibit the peaks corresponding to each particle state, just as the invariant mass does. Translating the method to the ω case and considering that $M(1) = m(ABC) - m(BC) + M(2)$, the expression for the ω invariant mass difference becomes:

$$\Delta m_{\pi^+\pi^-\pi^0} = m_{\pi^+\pi^-\pi^0} - m_{\gamma\gamma} + M_{\pi^0}, \tag{4.41}$$

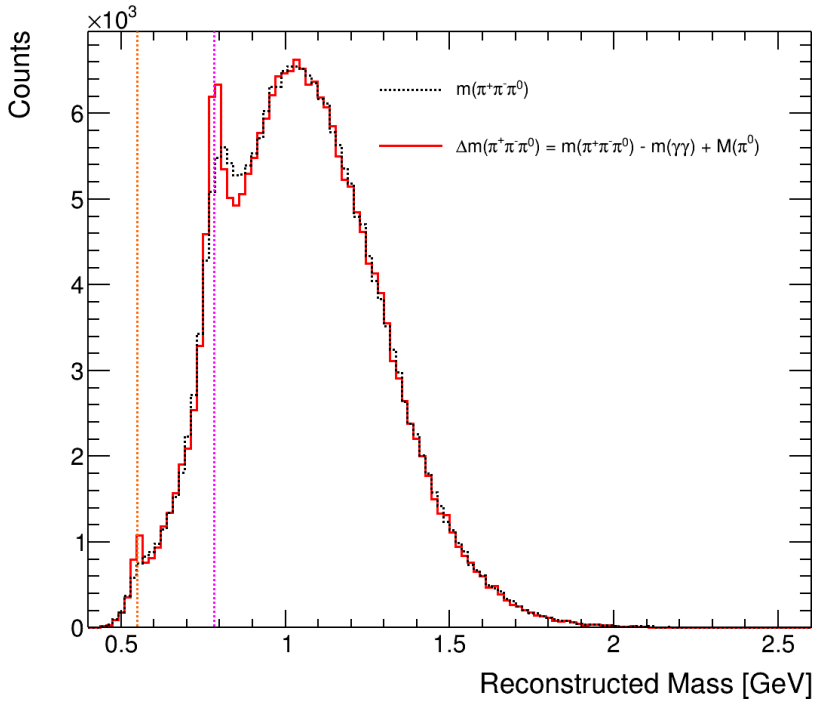

Figure 4.21: Invariant mass (black) and invariant mass difference (red) distributions of the reconstructed ω mesons, plotted simultaneously. Vertical lines represent the expected mass PDG values of η and ω mesons, with $M_\eta = 0.548$ GeV (orange) and $M_\omega = 0.782$ GeV (magenta) [22].

where $m_{\gamma\gamma}$ is the reconstructed invariant mass of the π^0, while M_{π^0} corresponds to the expected PDG value [22]. For comparison purposes, both reconstructed mass distributions are plotted simultaneously in Fig. 4.21. As it can be seen, the method grants two important benefits: the ω and η peaks gets narrower and higher, and the overall background shape does not change that much. For a more profound demonstration of the invariant mass difference method, please refer to the outstanding Ph.D. thesis written by Andrew Chislhom for the ATLAS Collaboration [55].

In conclusion, Figures 4.20 and 4.22 represent all the available ω candidates from the PID and kinematical cuts described throughout this chapter. The difference in the amount of data measured from each nuclear target can be appreciated. The largest amount of statistics corresponds to the data collected from the deuterium target, which results in the combined deuterium data from the three experimental runs in order to reduce the statistical errors when calculating the final results.

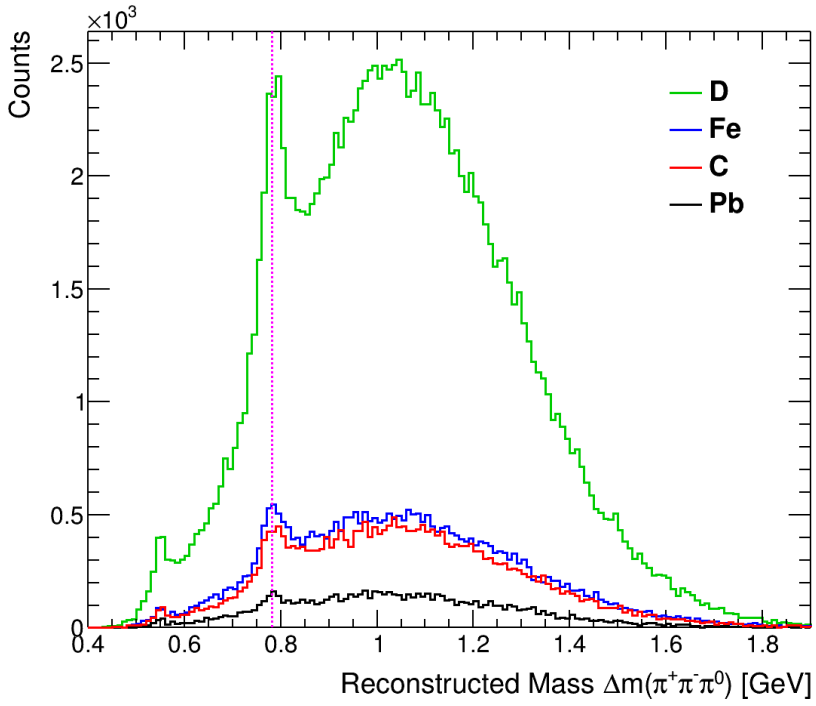

Figure 4.22: Invariant mass difference distributions of the reconstructed ω mesons from all targets. Green curve corresponds to the data collected from deuterium, blue curve to iron, red curve to carbon, and black curve to lead. Magenta vertical line represents the PDG value of the ω, $M_\omega = 0.782$ GeV [22].

4.9 BINNING

After the identification of the scattered electrons and the reconstruction of the ω meson as the hadron of interest, now it is possible to decide the binning in which the observable Multiplicity Ratio (MR) will be presented. As stated in Eq. 2.40, the MR is generally studied as a function of the inclusive electron variables Q^2 and ν, the hadronic variables z_h and p_T^2, and the nuclear targets.

There are two important factors to decide the binning of the MR. First, as seen in Fig. 4.22, this is a low-statistics analysis. Second, each of the kinematical variables presents very different and disperse shapes. Therefore, the most suitable option for presenting the MR of the ω mesons consists of one-dimensional distributions for each kinematic variable, equally distributed into 4 bins. In particular, the edges of each bin for all targets are calculated from the lead data since it is the target with the least statistics. The obtained edges are represented in Figure 4.23 and detailed in Table 4.9.

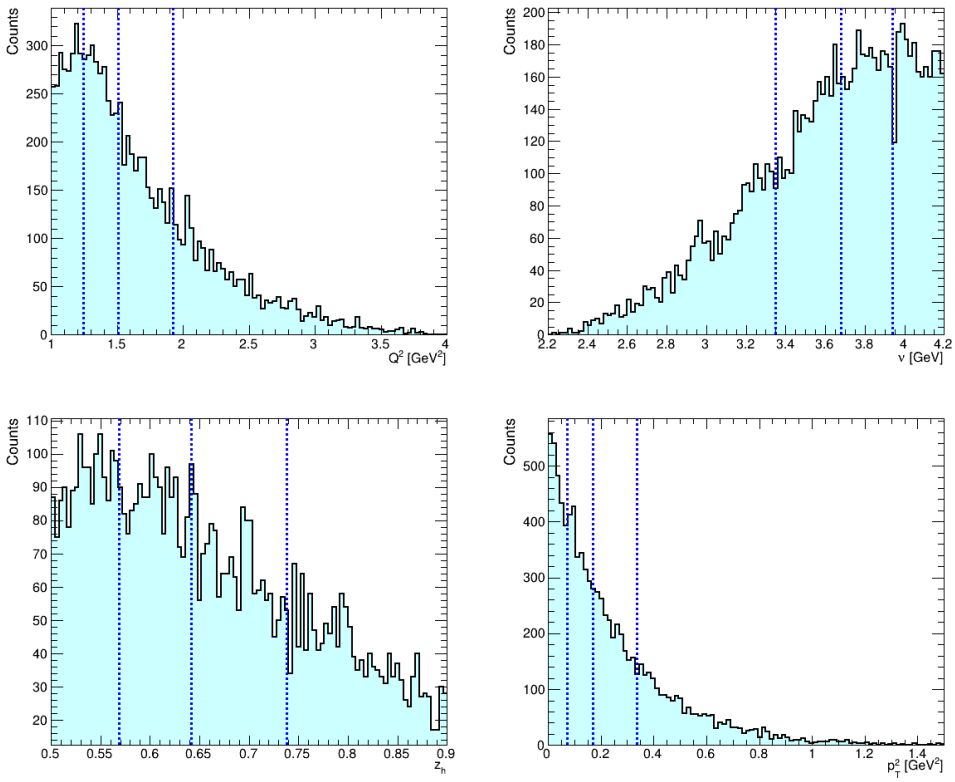

Figure 4.23: Distributions of Q^2 (upper left) and ν (upper right) of the scattered electrons of events with ω candidates, and distributions of z_h (bottom left) and p_T^2 (bottom right) of the ω candidates. Bin edges for each variable are given by the limits of the x-axis and the blue vertical lines in each histogram. Data taken from Pb target events.

Kinematic variable	Bin edges				
Q^2 (GeV^2)	1.0	1.25	1.51	1.92	4.0
ν (GeV)	2.2	3.35	3.68	3.94	4.2
z_h	0.5	0.57	0.64	0.74	0.9
p_T^2 (GeV^2)	0.0	0.07	0.17	0.34	1.5

Table 4.9: Binning for each variable, measured by using lead data.

4.10 ELECTRON NUMBERS

In the definition of the Multiplicity Ratio (MR), in Eq. 2.40, the number of semi-inclusive hadrons N_h in a given (Q^2, ν, z_h, p_T^2) bin is divided by the number of inclusive electrons $N_{e^-}^{DIS}$ in the same (Q^2, ν) bin.

The reason behind this normalization is to compensate for the different amount of events produced by each target and to cancel initial state effects.

The number of electrons and the multiplicity of hadrons are analogous to the relationship between luminosity $\mathcal{L}$ and cross section σ:

$$\sigma = \frac{R}{\mathcal{L}} \sim \frac{N_h}{N_e^{DIS}}, \tag{4.42}$$

where R is the rate of events. Figure 4.24 represents the number of inclusive electrons of each target for each bin of Q^2 and ν. Compared to the rest of the targets, the high number of electrons from deuterium is explained by the fact that deuterium data was merged from the three experimental runs, in order to decrease statistical errors in the final results.

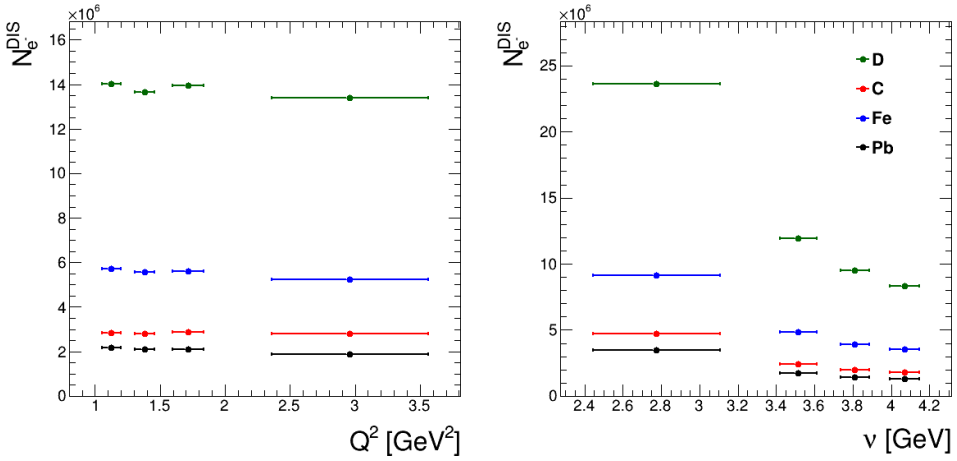

Figure 4.24: Number of inclusive DIS electrons depending on Q^2 and ν, for each target.

Target	Number of inclusive DIS electrons
D	54,997,138
C	11,287,494
Fe	22,137,224
Pb	8,234,343

Table 4.10: Integrated number of inclusive electrons for each target after all PID cuts. These values are used for the normalization of the number of ω mesons in hadronic variables z_h and p_T^2.

4.11 BACKGROUND SUBTRACTION

This section is dedicated to the description of the underlying background in the invariant mass difference distributions in order to extract the ω meson signal. During the development of this thesis, two methods for background subtraction were studied:

1. Background subtraction through a signal and background fit.
2. Description of the background with an event-mixing technique, to be later normalized and subtracted directly from data.

4.11.1 Signal and Background Fitting

The most direct approach to subtract the background is to fit the peak of the particle of interest with a signal and background model. This will allow counting the number of hadrons produced by integrating the signal component of the composite model.

The primary tool to perform the fit is the RooFit library [57], a toolkit developed to model the distribution of physics analysis events and carry various studies, such as convolution of probability density functions (PDF), unbinned maximum likelihood fits, and generation of toy Monte-Carlo samples.

The present fitting method consists of a maximum likelihood fit [58], which analyzes unbinned data by fitting the model function to a database on an event-by-event basis instead of fitting binned data points as the standard least-squares estimations do. The computation time of the maximum likelihood estimations is significantly longer than the least-squares method since the process depends directly on the number of events to analyze, making it perfect for low-statistic analyses as the current one. However, one major limitation is that this method does not have known tests to measure the goodness of the fits.

The fit function to use is an extended model expressed as:

$$f(x) = N_\omega \; G(x;\; \mu,\, \sigma) + N_{bkg} \; p_2(x;\; b_1,\, b_2), \tag{4.43}$$

where $G(x;\; \mu,\, \sigma)$ corresponds to a Gaussian probability density function (PDF) to represent the ω signal, $p_2(x;\; b_1,\, b_2)$ corresponds to a second-order Chebyshev polynomial to describe the underlying background, N_ω is the number of ω mesons, and N_{bkg} is the number of background particles. Since it is an extended model, these numbers are correlated by $N_\omega + N_{bkg} = N_{tot}$, being N_{tot} the total number of entries or ω candidates in the region of interest. Therefore, the extraction of ω yields is obtained directly from the fit's parameter N_ω. As an example, Fig. 4.25 represents the fits of all data in each z_h bin.

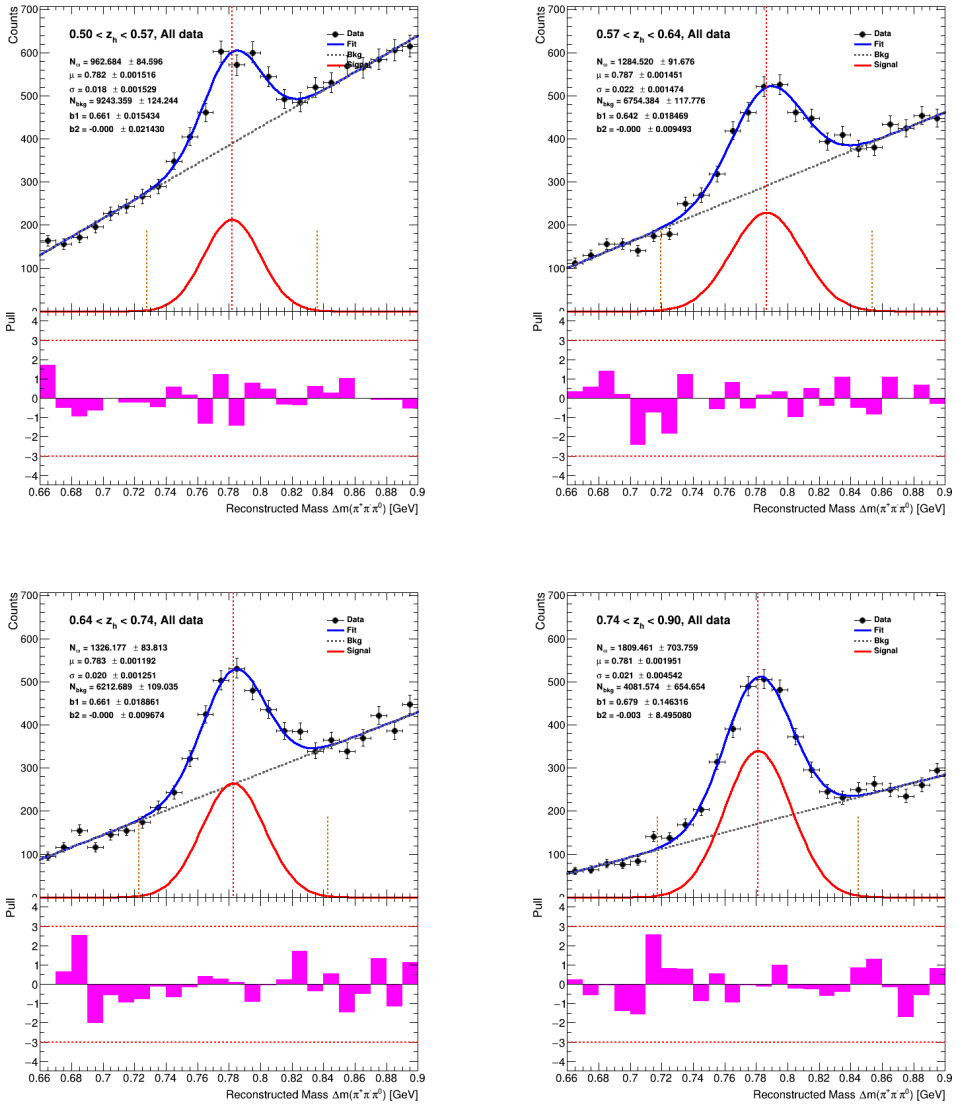

Figure 4.25: Signal and background fit for the ω yields extraction using all data, for each bin of z_h. In each panel, the upper plot corresponds to the model of Eq. 4.43 (blue) being fitted to the data (black), with its signal (red) and background (gray) components depicted. The central vertical line correspond to the obtained μ value, while the lateral lines delimit the $\mu \pm 3\sigma$ range. Lower plots are the subsequent pull distributions (magenta) of each fit, with red horizontal lines highlighting a difference of 3 standard deviations away from data. All fits for each separate target and kinematical bins can be found in Section A.1.

The range of the fitting is the same for every bin, and corresponds to a $\mu \pm 5\sigma$ cut, with $\mu = 0.782$ GeV and $\sigma = 0.024$ GeV obtained as parameters from a preliminary fit. A limit is imposed on the quadratic coefficient

of the second-order polynomial so that it is always negative. To stabilize the results, both μ and σ were fixed to the obtained values after fitting all data. The values are given in Table 4.11, and they are the same for each kinematical bin, independently of the target. This idea falls under the assumption that the width of the peak should remain the same for all targets as the resolution should not depend on the target, but the energies of the particles and their kinematical bin. Similarly, the present work also assumes that the signal's position, or mean, should not depend on the target nor the kinematical variable. However, because of charged pions energy loss, this statement still needs to be revised. This technique is still a conservative approach compared to a widely used method of extracting resonances by fixing the peak widths and positions to their nominal PDG values [59, 60].

Kinematic variable	Q^2		ν		z_h		p_T^2	
Bin number	μ	σ	μ	σ	μ	σ	μ	σ
0	0.785	0.024	0.784	0.024	0.782	0.021	0.790	0.018
1	0.785	0.024	0.784	0.021	0.787	0.023	0.785	0.022
2	0.785	0.022	0.783	0.022	0.783	0.021	0.782	0.020
3	0.781	0.019	0.783	0.023	0.781	0.022	0.782	0.021

Table 4.11: Obtained μ and σ (in GeV) of the resulting Gaussian function after fitting each kinematical bin over all data. Both parameters are fixed to these values when fitting each target by separate, as it can be seen in Section A.1.

The errors of the parameters were measured with the TMinuit class of Root by using the MINOS algorithm [61]. As an attempt to evaluate the goodness of the fits, a pull distribution is shown below each fit panel in Fig. 4.25. The expression to build a pull histogram is as follows:

$$\text{pull}(x_i) = \frac{\text{data}(x_i) - \text{model}(x_i)}{\text{data error}(x_i)}, \tag{4.44}$$

where x_i correspond to a respective bin of the invariant mass difference distribution. One can interpret that a fit is *good* if the pull values appear to be randomly distributed. For example, if the pull distribution presents a recognizable mathematical structure, e.g., a sinusoidal shape, the fit can be further improved.

The complete representation of the fit process for all targets and kinematical bins is given in Section A.1. The extracted number of ω mesons measured using this method is shown in Fig. 4.26. The subsequent Multiplicity Ratio (MR) results of the ω meson are presented in Section 6.1. In the end, these results serve as a first approximation, and they are not the

primary tool for ω signal extraction. Despite how straightforward is the process, the background subtraction through function fitting presents a critical disadvantage: the fitting function is arbitrary and not physically motivated, and it may be insufficient due to the lack of statistics.

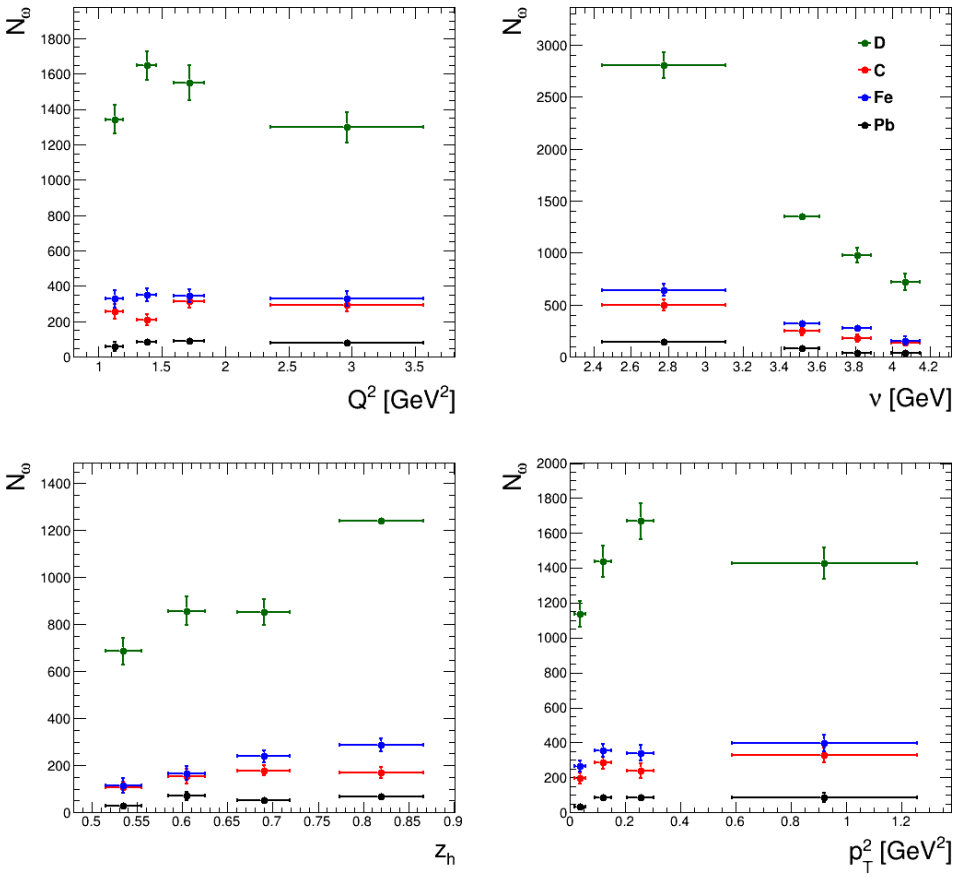

Figure 4.26: Extracted number of ω mesons after signal and background fitting, depending on each kinematical variable and target.

4.11.2 Event-Mixing Method

The event-mixing method [62] is a thoroughly used technique in reconstructing neutral mesons [19, 56]. The main idea is to describe the background shape of the ω invariant mass difference with pions that are no longer correlated, i.e., originating from different events. This technique requires a high degree of fine-tuning but overcomes most of the disadvantages of subtracting background through function fitting.

The event mixing for this analysis is performed with all ω candidates already selected to ensure the same phase space as the regular data. New ω mesons are artificially created by swapping one of their constituent

particles with another random ω candidate, which must belong to the same target type, i.e., same z-electron vertex cut and same experimental run. This idea is repeated four times: by exchanging only positive pions, only negative pions, only neutral pions (the photon pair), and the three pions at once.

The random number generator used is the one provided by ROOT through the TRANDOM3 class [51]. The new datasets present similar invariant mass difference distributions and are summed to form the mixed-event background, resulting in a statistic four times bigger than data. A comparison between the distributions of different kinematic variables of the data and the newly formed event-mixing can be seen in Figure 4.27.

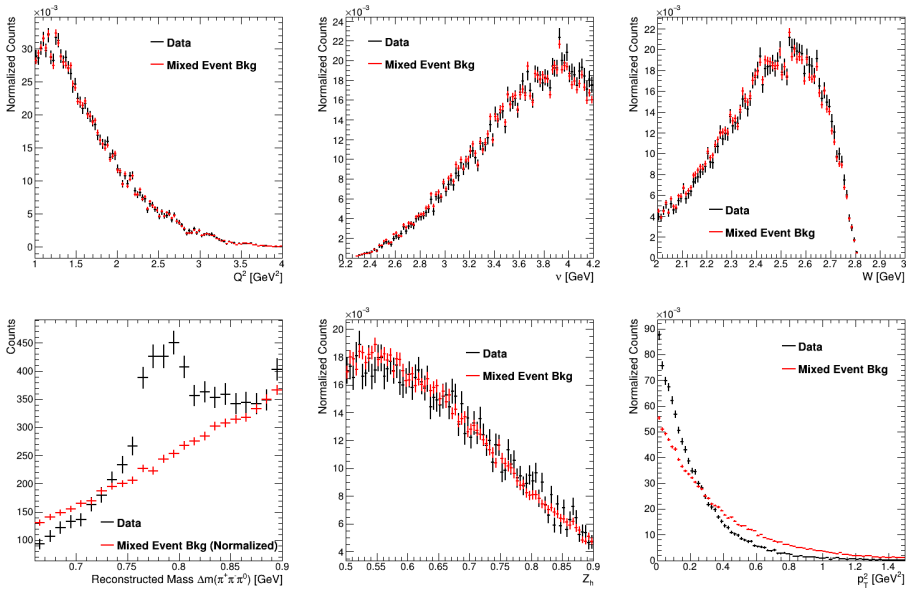

Figure 4.27: Comparison plots between carbon data (black) and mixed event background (red) for distinct kinematical variables. Upper row corresponds to the electron distributions Q^2, ν, and W, while the lower row presents the ω distributions $\Delta m_{\pi^+\pi^-\pi^0}$, z_h, and p_T^2.

What follows is the most crucial step: the normalization. In the invariant mass difference distributions, the mixed-event background must be normalized to match the data statistics in order to subtract both distributions and extract the hadron signal. The region of interest is around the expected ω invariant mass in a $\mu \pm 5\sigma$ range, with $\mu = 0.782$ GeV and $\sigma = 0.024$ GeV obtained from a preliminary fit. The mixed-event background distribution is then scaled by the following quantity:

$$\frac{I^{data}_{\Delta x_1} + I^{data}_{\Delta x_2}}{I^{bkg}_{\Delta x_1} + I^{bkg}_{\Delta x_2}}, \tag{4.45}$$

where $I_{\Delta x}$ corresponds to the integral of the data or mixed-event background distributions over the specific ranges Δx of the invariant mass difference:

$$\begin{aligned} \Delta x_1 : \quad & 0.66 < \Delta m_{\pi^+\pi^-\pi^0} < 0.71 \text{ GeV, and} \\ \Delta x_2 : \quad & 0.85 < \Delta m_{\pi^+\pi^-\pi^0} < 0.90 \text{ GeV.} \end{aligned} \tag{4.46}$$

The upper row in Fig. 4.28 represents the ω invariant mass distributions in each p_T^2 bin for data and the normalized event-mixed background.

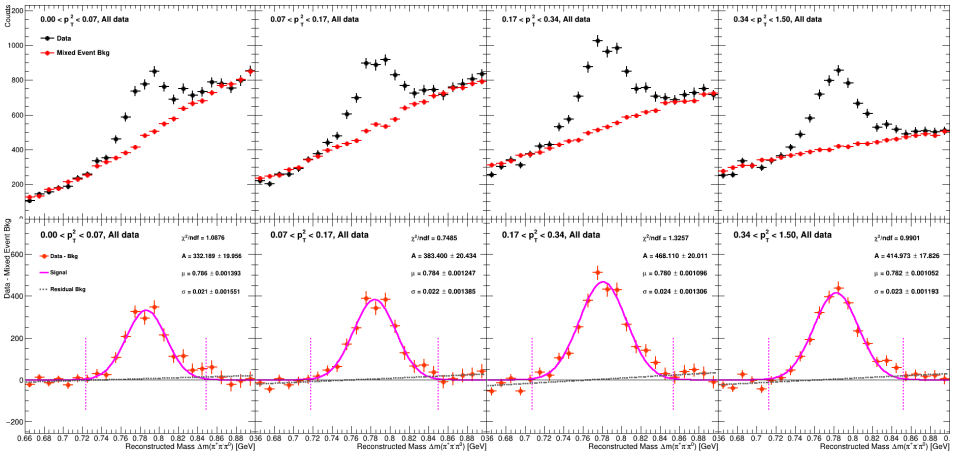

Figure 4.28: Signal extraction procedure after the generation of mixed event background, using all data for each p_T^2 bin. In the upper row, the mixed event background (red) is normalized to match the data (black). In the lower row, the background-subtracted distribution is fitted with a Gaussian (magenta) and a first-order polynomial (gray). The χ^2/ndf of the composite fit is shown. Vertical lines correspond to the $\mu \pm 3\sigma$ range used to integrate the number of ω mesons.

After the normalization, the mixed event background distribution is subtracted from the data, as depicted by the orange histograms in the lower row of Fig. 4.28. This new *background-subtracted* distribution is then fitted with the following model to subtract the residual background caused by the the normalization or the imperfections of the method:

$$f(x) = G(x;\ A,\ \mu,\ \sigma) + p_1(x;\ a_1,\ a_2), \tag{4.47}$$

where $G(x; A, \mu, \sigma)$ is an unnormalized Gaussian distribution and $p_1(x; a_1, a_2)$ is a first-order polynomial. In this case, after the subtraction of histograms, it is not possible to fit a database like in Section 4.11.1. The fit method employed was a regular chi-square fit, with the respective χ^2/ndf values shown. The Gaussian's parameters μ and σ are fixed of a prior procedure done in all data for each kinematical bin, as in Fig. 4.28. The fitting procedure is only used to describe the remaining background and determine the center of the integration range, but not for the yields' actual calculation.

The number of ω mesons is calculated by integrating the subtracted-background distribution over the obtained $\mu \pm 3\sigma$ range. As this histogram can present negative values due to high volatility and low statistics, only positive entries are summed. The results of this integration can be seen in Fig. 4.29.

The event-mixing method corresponds to the primary approach to calculate the main results of this work in Section 6.1. For more information, the complete process for all targets and all kinematical bins is presented in Section A.2.

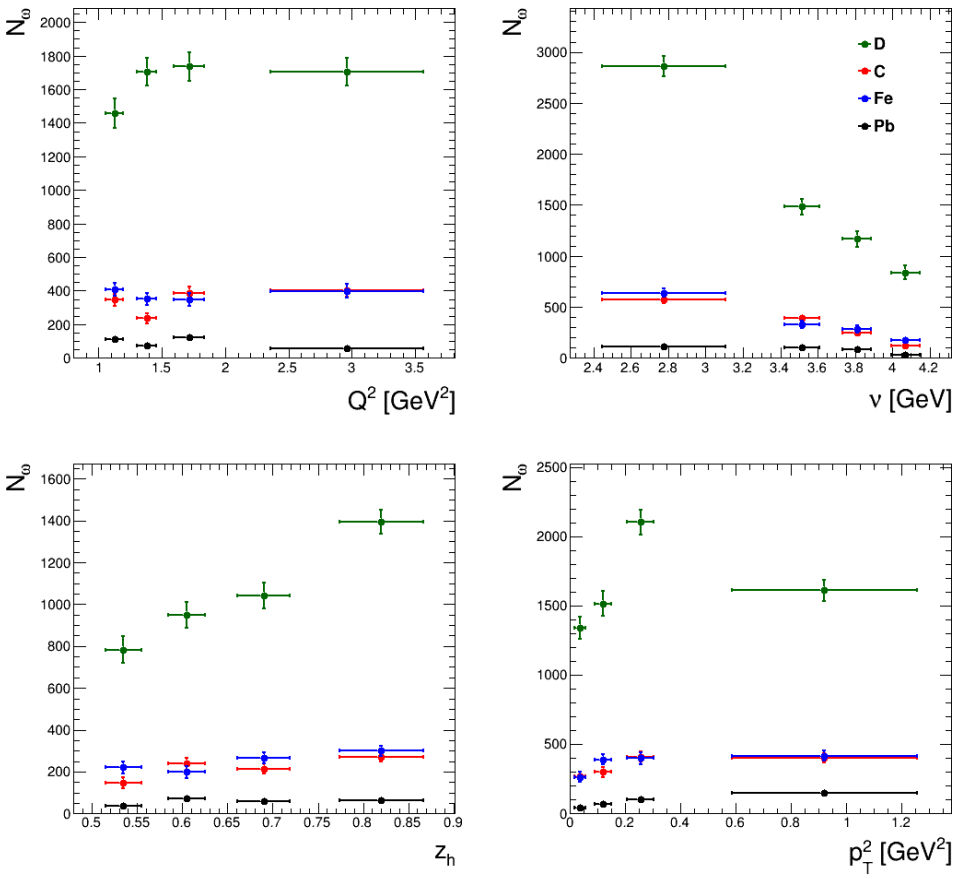

Figure 4.29: Extracted number of ω mesons after background subtraction through event-mixing, depending on each kinematical variable and target.

5 MONTE CARLO SIMULATIONS

No high-energy particle detector is exempt from having geometrical limitations or sectors and track reconstructions with poor efficiency. The procedure to correct such deficiencies is called *Acceptance Correction* and is based on contrasting the data with simulations of physical events.

Section 5.1 describes the generation of Monte Carlo (MC) events with LEPTO [63] and their reconstruction with the CLAS software to resemble the collected data. Section 5.2 and Section 5.3 describe the identification and selection of particles from the generated and reconstructed events, respectively. Section 5.4 shows a brief comparison between data and simulations. Section 5.5 presents the obtained acceptance correction factors for electrons and ω mesons.

5.1 GENERATION AND RECONSTRUCTION OF MONTE CARLO EVENTS

This particular analysis focuses on the ω meson production. Therefore, to calculate ω meson acceptance corrections in CLAS, events must be generated in which at least one omega has been generated and has decayed through the three pion channel. An alternative is to generate all particles. However, due to the low multiplicity of the ω meson and the high amount of underlying background, it is preferable to generate and reconstruct only the signal.

As a first step, the events are generated with a widely used software called LEPTO 6.5.1 [63]. This program is a Fortran-based Monte Carlo (MC) event generator, developed upon PYTHIA 5.7 and JETSET 7.4 [33], with a large amount of parameters and possible configurations. The process to be simulated consists of a DIS reaction, with an electron with energy $E_b = 5.014$ GeV incident on a fixed nuclear target with atomic mass A and atomic number Z. Table 5.1 gives the kinematical constraints to carry out the simulations. Tables 5.2 and 5.3 represent the values and descriptions of the parameters that were modified from their default value.

The output of LEPTO consists of a text file listing each event, the phase space of the outgoing electron, and all the generated particles and their decays. To manage the data with the standard format for HEP experiments, this file is converted into BOS format using the TXT2PART program.

Lower limit parameter	Variable	Upper limit parameter
CUT(1) = 0.09	$< x_B <$	CUT(2) = 1.0
CUT(3) = 0.0	$< y_B <$	CUT(4) = 1.0
CUT(5) = 0.9	$< Q^2 <$	CUT(6) = 10.0
CUT(7) = 4.0	$< W^2 <$	CUT(8) = 20.0
CUT(9) = 0.0	$< \nu <$	CUT(10) = $E_b - 0.3$
CUT(11) = 0.01	$< E' <$	CUT(12) = E_b

Table 5.1: Effective kinematic region imposed on LEPTO [63] for the generation of DIS events.

Configuration	Description
LST(1) = 1	Choose Q^2 and x_B as independent variables to simulate and integratethe cross section.
LST(2) = 1	Choose kinematic variables from differential cross section and cuts applied in the CUT() array.
LST(3) = 5	Set verbosity as full output.
LST(5) = 3	Set laboratory system as frame of reference.
LST(8) = 9	Simulation of QCD effects in hadronic final state are set by ARIADNE, [64].
LST(9) = 5	Set maximum-virtuality of parton initiating the shower to be $Q^2(1-x)\max(1, \ln(1/x))$.
LST(15) = 10	Choose CTEQ2D as source of PDFs, [65].
LST(16) = 1	Use PYTHIA's internal library of PDFs according to LST(15) [33].
LST(17) = 1	Allow varying energies of initial particles from event to event.
LST(19) = −1	Prevent use of grid, integrals are calculated for each event.
LST(23) = 1	Specify the simulated process as a γ exchange, i.e., electromagnetic interaction.
LST(25) = 1	Specify flavor of struck quark to d.
LST(26) = 5	Set entry line number of outgoing struck quark in event record.
LST(27) = 1	Split non-trivial nucleon remnant into parton and particle.
LST(31) = 1	Set Q^2 and x_B as integration variables.
PARL(1) = A	Set number of nucleons in target nucleus, i.e, A.
PARL(2) = Z	Set number of protons in target nucleus, i.e, Z.
PARL(8) = 0.02	Set lower cut in the QCD matrix elements to prevent gluon fusion divergencies.
PARL(9) = 3.5	Set upper cut in the QCD matrix elements to prevent gluon fusion divergencies

Table 5.2: Configuration of LEPTO used in this analysis. A detailed explanation on each parameter and their default values is given in Ref. [63].

Configuration	Description
PARJ(21) = 0.3	Set width σ of the Gaussian transverse momentum distributions for primary hadrons.
PARJ(23) = 0.02	Set parameterization factors of non-Gaussian tails on the Gaussian transverse momentum model assumed in PARJ(21).
PARJ(24) = 3.5	Set parameterization factors of non-Gaussian tails on the Gaussian transverse momentum model assumed in PARJ(21).
PARJ(41) = 0.6	Set parameter a of the symmetric Lund fragmentation function.
PARJ(42) = 0.1	Set parameter b of the symmetric Lund fragmentation function.

Table 5.3: Configuration of PYTHIA and JETSET parameters used in this analysis. A detailed explanation of each parameter is given in Ref. [33].

Once the information is stored in BOS format, it is possible to recreate the interaction of the generated final-state particles with the detector. This is done with the GEANT3-based [66] program GSIM, which simulates the geometry, materials and efficiency of the CLAS detector components. Within GSIM, the double-target configuration of the EG2 experiment is also implemented [15, 67].

As a next step, the data are passed through the GSIM Post-Processor, also known by its acronym GPP. This program is in charge of smearing the momentum and resolution of the particle measurements. Additionally, it incorporates inefficient detector elements that have been previously reported, such as scintillators or specific wires.

After passing through GSIM and GPP, the last step in the reconstruction chain is RECSIS [47]. As seen in Section 3.4, RECSIS corresponds to the exact set of programs used to reconstruct the data. After this procedure, the data of both generated and reconstructed particles can finally be converted into CLASTOOL format by the WRITEROOTDST program.

Regarding the number of events to be simulated, the objective is to generate enough events to reconstruct approximately more than 10 times ω mesons than the measured data, for each target and kinematical bin. The number of effective generated events is given in Table 5.4 below.

5.2 GENERATED PARTICLES IDENTIFICATION

One of the features of MC events is that the generated particles are already identified. It is not necessary to develop a new particle identification scheme or corrections to determine the generated final-state particles. This includes electrons, positive pions, negative pions, and photons. Figure 5.1 represents the number of DIS electrons as a function of Q^2 and ν. The integrated electron numbers per target–proportional to the number of events generated–are given in Table 5.4.

However, because the MC event generation and reconstruction code was inherited from previous analyses, the situation is different for the generated ω mesons. After generating more than half of the required MC simulations, two historical problems were encountered in the reconstruction process and the CLASTOOL format.

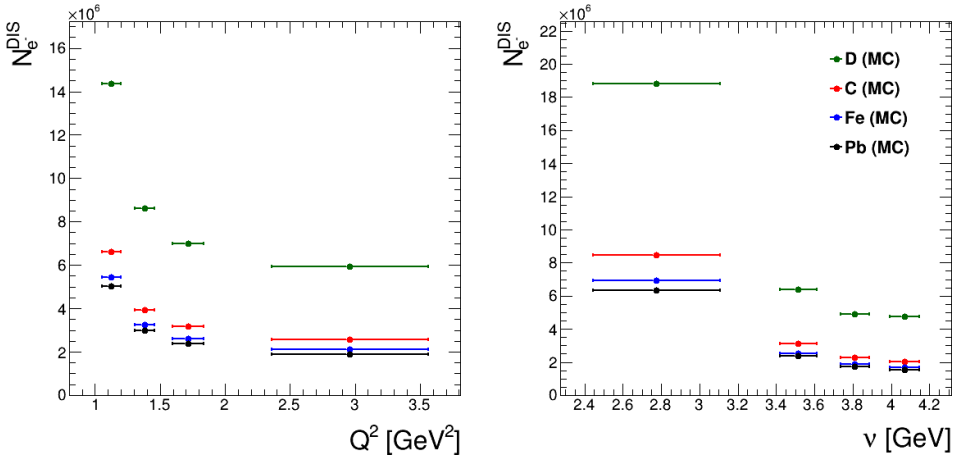

Figure 5.1: Number of MC generated electrons depending on Q^2 and ν, for each target.

Target	Number of inclusive DIS electrons
D	35,923,569
C	16,322,703
Fe	13,388,214
Pb	12,294,220

Table 5.4: Integrated number of MC generated inclusive electrons for each target after all PID cuts. These values are used for the normalization of the number of generated ω mesons in hadronic variables z_h and p_T^2.

One of the issues is the absence of a direct link between the generated and reconstructed particles. To address this, algorithms can be developed to approximately match the particles based on kinematical and geometrical criteria, such as *angular matching* [18, 20].

The next problem is that only final-state particles information is stored, but no parent particle information. Because of this, it is not possible to know whether a generated final-state particle comes from the decay of an ω meson. To deal with this, it is necessary to define a scheme to identify the generated ω mesons.

NEUTRAL PION RECONSTRUCTION

To count how many ω mesons were generated, it is necessary to select the Monte Carlo events that have at least $1\pi^+$, $1\pi^-$ and 2γ, combine the particles and form all possible ω candidates. After that, it is necessary to ensure that the photons come from the decay of a π^0. But since no information on the parent particles is available, one can reconstruct the neutral pion invariant mass and cut the signal region, similarly to the reconstruction procedure done in Section 4.6.

Figure 5.2 represents the reconstruction of the generated π^0 invariant mass through its 2γ decay, and it presents a clear peak in the expected π^0 signal [22]. A Gaussian function fit is made in the signal region, and from the obtained parameters, a $\mu \pm 3\sigma$ cut is further applied:

$$0.134 < m_{\gamma\gamma} < 0.136 \text{ GeV}. \tag{5.1}$$

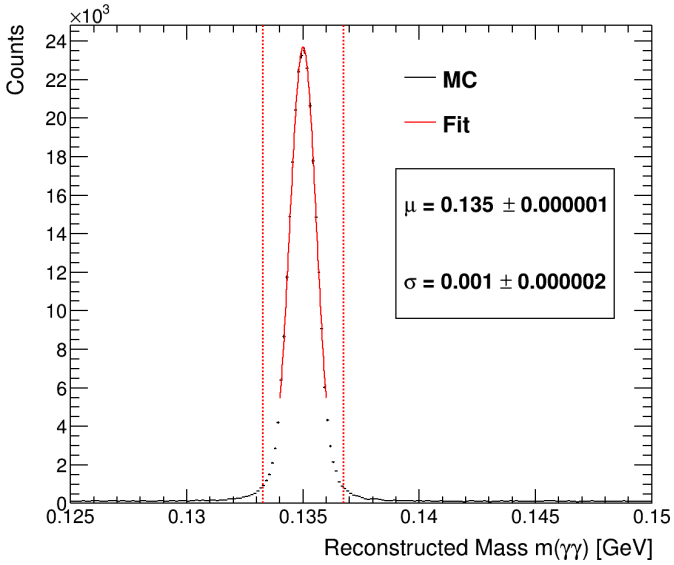

Figure 5.2: Gaussian fit around generated π^0 invariant mass. Vertical lines represent the $\mu \pm 3\sigma$ cut. Obtained μ is in exact agreement with nominal PDG value [22].

OVERVIEW OF CUTS

In addition to the final-state particles pre-identification and the neutral pion reconstruction, there is still a variety of cuts to consider:

- Unlike data, there is no vertex cut for the generated events. The vertex information is already determined by selecting the simulation file, which predetermines the vertex position, geometry, atomic number, and atomic mass of the nuclear target.

- As data, all DIS kinematical cuts of Eq. 4.26 are maintained.
- To keep consistency, the exclusion of neutral kaons is done in the same region of Eq. 4.36.

OMEGA RECONSTRUCTION AND BACKGROUND SUBTRACTION

Since there is no parent particle information, the only way to count the generated ω mesons is by reconstructing their invariant mass through their three-pion decay. However, one of the disadvantages of this method is that some combinatorial background will appear under the ω signal. To subtract it, one can employ the same method used for data in Section 4.11.2: the event mixing.

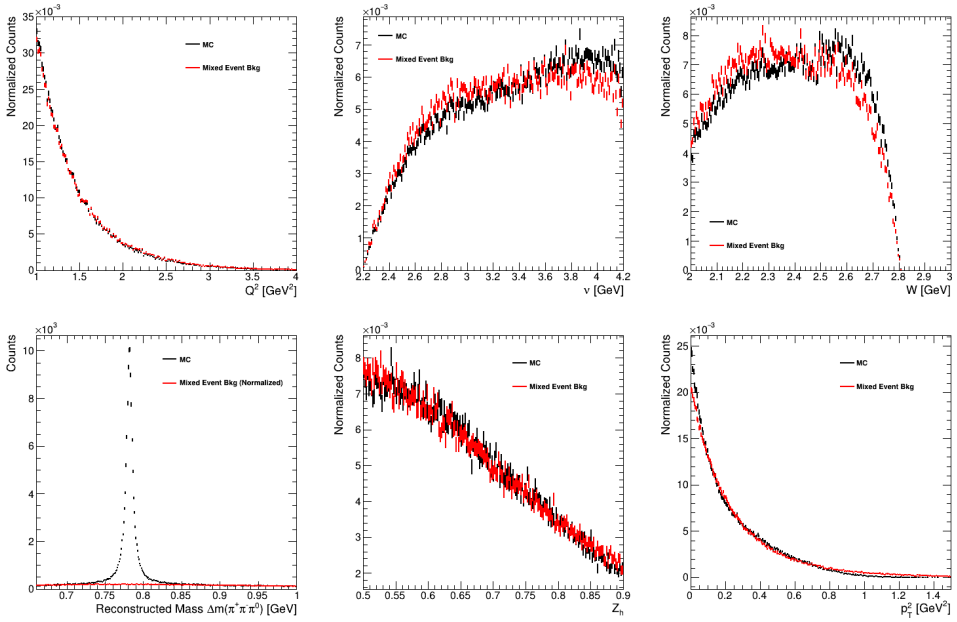

Figure 5.3: Comparison plots between generated carbon events (black) and mixed event background (red) for distinct kinematical variables. From left to right, the upper row corresponds to the electron distributions Q^2, ν, and W, while the lower row presents the ω meson distributions $\Delta m_{\pi^+\pi^-\pi^0}$, z_h, and p_T^2.

The event mixing procedure remains the same as with data, with the exception being the background subtraction process. As the shape of the generated ω mesons is different than data's, a model composed of a Breit-Wigner distribution and a first-order polynomial is preferred to fit the ω peak:

$$f(x) = A\,B(x;\ x_0,\ \gamma) + p_1(x;\ a_1,\ a_2), \tag{5.2}$$

here $B(x; x_0, \gamma)$ is a normalized Breit-Wigner distribution and $p_1(x; a_1, a_2)$ is a first-order polynomial. In contrast to the Gaussian distribution, the amplitude or maximum of the Breit-Wigner distribution is given by $A/(\pi\gamma)$,

the peak position is given by x_0, and the Half Width at Half Maximum (HWHM) is given by γ. This last parameter relates to the σ of the Gaussian distribution as:

$$\text{HWHM} = \gamma = \sqrt{2\ln 2}\,\sigma \approx 2.335\,\sigma \tag{5.3}$$

Therefore, to keep an equivalent cut of the $\mu \pm 3\sigma$ range as before, the cut $x_0 \pm 1.274\gamma$ is used.

Figure 5.4 corresponds to an example of the background subtraction procedure. As done in Section 4.11.2, the fitting is only used to describe the remaining background–which in this case is almost null–and determine the center of the integration range, but not for the actual calculation of the number of ω mesons. Instead, they are calculated by integrating the histogram in the stated range and the results of this integration can be seen in Fig. 5.5. For more information, the complete process for all targets and kinematical bins is presented in Section A.2.2.

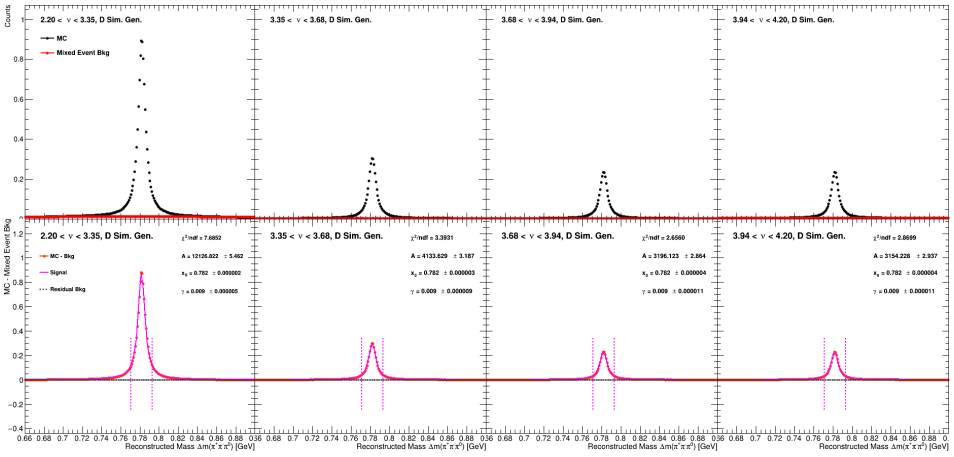

Figure 5.4: Signal extraction procedure after the generation of mixed event background, using generated events from deuterium simulations for each ν bin. In the upper row, the mixed event background (red) is normalized to match the data (black). In the lower row, the background-subtracted distribution is fitted with a Gaussian (magenta) and a first-order polynomial (gray). The χ^2/ndf of the composite fit is shown. Vertical lines correspond to the $x_0 \pm 1.274\gamma$ range used to integrate the number of ω mesons.

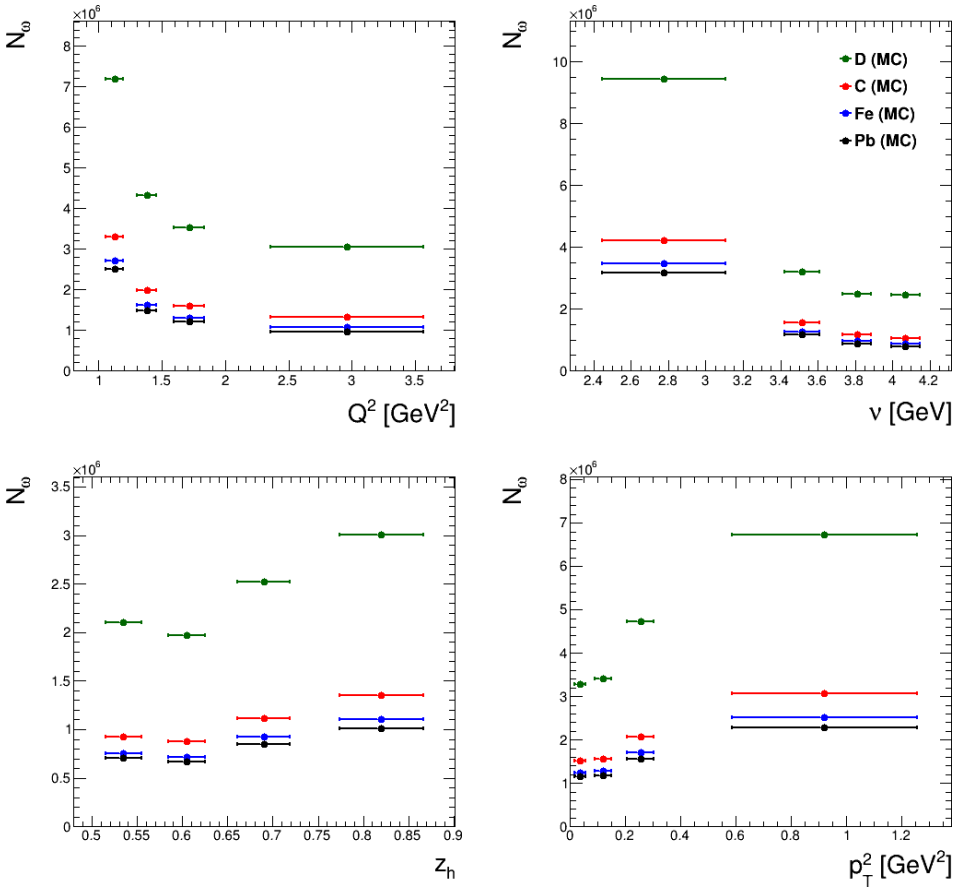

Figure 5.5: Extracted number of generated ω mesons after background subtraction through event mixing, depending on each kinematical variable and target.

5.3 RECONSTRUCTED PARTICLES IDENTIFICATION

This section describes the particle identification criteria used to determine the type of reconstructed or *accepted* particles. In general, the cuts are the same as those used for data in Chapter 4. The present section will specify when otherwise.

ELECTRONS IDENTIFICATION

Reconstructed electrons are identified following the same PID scheme used for data, with the only exception of the Sampling Fraction cuts. The cut maintains the same expression of Section 4.1,

$$\left| \frac{E}{p} - \mu(p) \right| > 2.5\,\sigma(p), \tag{5.4}$$

where $E = \max(E_{in} + E_{in}, E_{tot})$ is the electron's energy; and $\mu(p)$ and $\sigma(p)$ are two momentum-dependent functions with parameters that, this time, do not depend on the sector or the target system.

$$\mu(p) = a_1 + a_2 p + a_3 p^2, \tag{5.5}$$

$$\sigma(p) = \sqrt{b_1^2 + \frac{b_2^2}{p}}. \tag{5.6}$$

The values of the parameters $a_{1,2,3}$ and $b_{1,2}$ were obtained from fits performed by Taisiya Mineeva [20] and are given in Table 5.5. Figure 5.6 illustrates the application of the sampling fraction cuts on the E/p vs p distributions of reconstructed electrons.

a_1	a_2	a_3	b_1	b_2
2.623 $\times 10^{-1}$	8.9 $\times 10^{-3}$	-1.9 $\times 10^{-3}$	5.7 $\times 10^{-3}$	3.05 $\times 10^{-2}$

Table 5.5: Parameters extracted from fit on simulations, for sampling fraction cut on reconstructed electrons identification. Courtesy from Ref. [20].

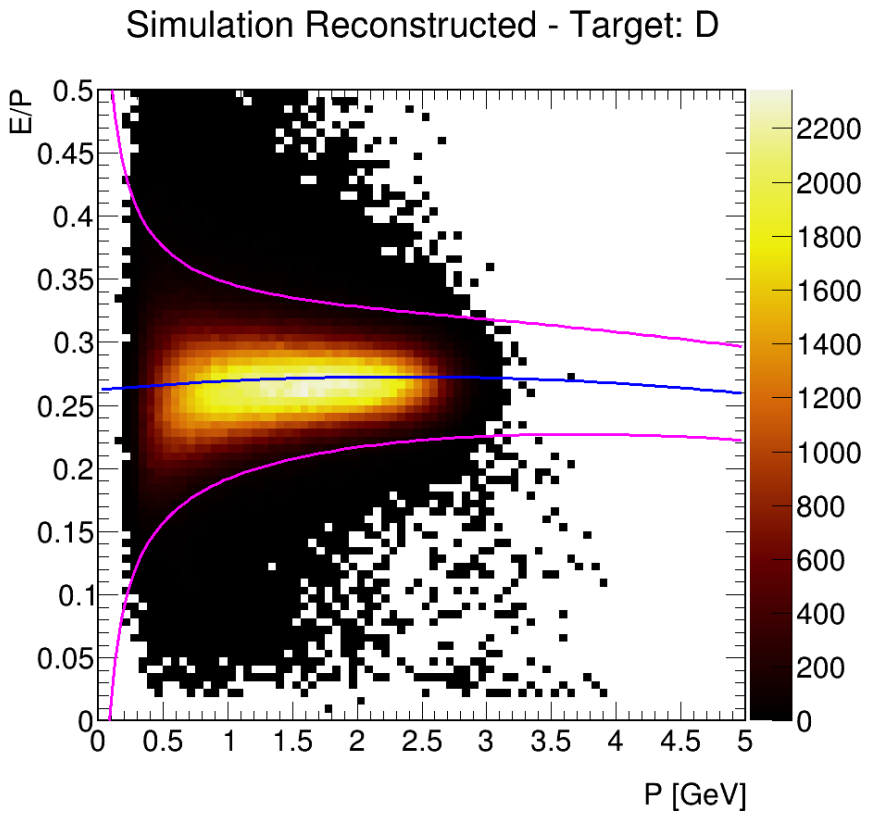

Figure 5.6: E/p vs p distribution for simulation reconstructed electrons. Central blue curve corresponds to $\mu(p)$ and magenta curves correspond to sampling fraction cuts $\mu \pm 2.5\sigma$, according to Eqs. 5.4, 5.5, and 5.6.

After identifying the electrons, in conjunction with the DIS kinematical cuts of Eq. 4.26, one can count the number of electrons generated per target and kinematic bin. The counts of electrons are plotted as a function of Q^2 and ν in Fig. 5.7, while the integrated counts are given in Table 5.6.

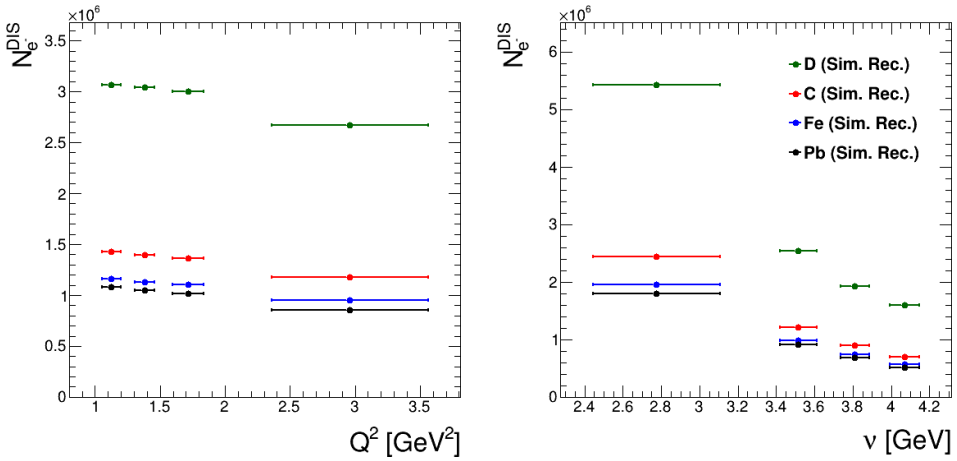

Figure 5.7: Number of simulations reconstructed inclusive DIS electrons depending on Q^2 and ν, for each target.

Target	Number of inclusive DIS electrons
D	11,778,035
C	5,365,105
Fe	4,348,846
Pb	3,997,881

Table 5.6: Integrated number of simulation reconstructed electrons for each target after all PID cuts. These values are used for the normalization of the number of simulation reconstructed ω mesons in hadronic variables z_h and p_T^2.

CHARGED PIONS IDENTIFICATION

The PID of the charged pions, π^+ and π^-, follow the same rules described in Section 4.2, except for the TOF cut of the reconstructed π^-, which is slightly different.

As a reminder, the corrected TOF measurement corresponds to:

$$\Delta T = \left(\frac{l_{SC}^{e^-}}{c} - \frac{l_{SC}^{\pi^-}}{v^{\pi^-}} \right) - \left(t_{SC}^{e^-} - t_{SC}^{\pi^-} \right), \tag{5.7}$$

where l_{SC} and t_{SC} correspond to each particle's path lengths and TOF from the interaction vertex to the SC, respectively. $c = 30$ cm/ns is the speed

of light in vacuum, and v^{π^-} is the velocity of the reconstructed negative pion, derived from SC measurements. The momentum-dependent cuts on this variable are reflected in Table 5.7 and depicted in Fig. 5.8.

Momentum range (GeV)	Corr. Time of Flight (ns)
$0.00 < P \leq 0.50$	$-0.75 \leq \Delta T < 0.80$
$0.50 < P \leq 1.00$	$-0.55 \leq \Delta T < 0.60$
$1.00 < P \leq 1.50$	$-0.55 \leq \Delta T < 0.65$
$1.50 < P \leq 2.00$	$-0.50 \leq \Delta T < 0.54$
$2.00 < P \leq 2.50$	$-0.50 \leq \Delta T < 0.45$
$2.50 < P \leq 5.00$	$-0.50 \leq \Delta T < 0.50$

Table 5.7: TOF cuts on ΔT to identify simulation reconstructed π^-. Values taken from Ref. [18].

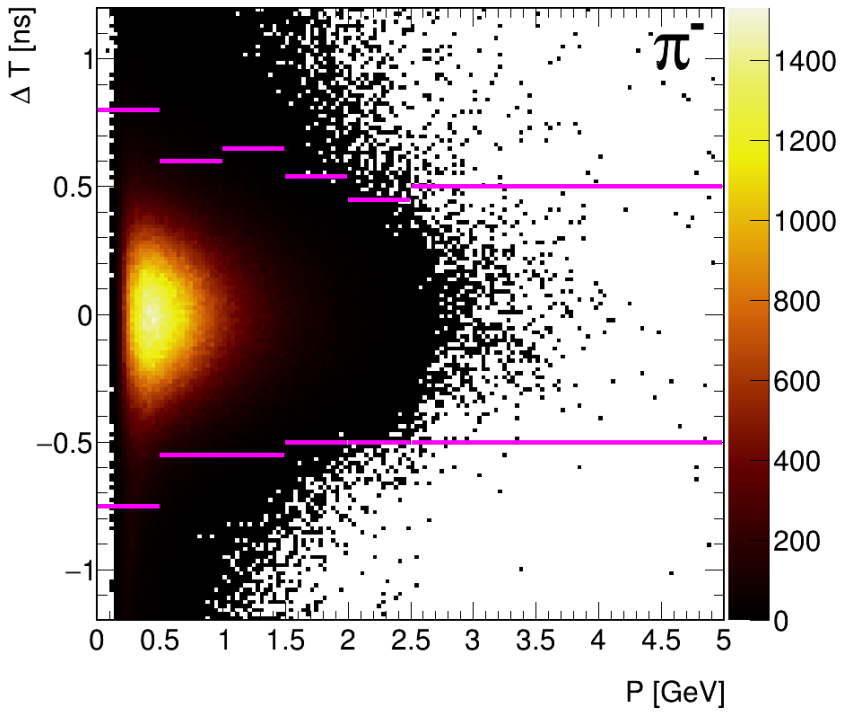

Figure 5.8: Plot of ΔT vs momentum of simulation reconstructed π^-. Horizontal lines represent ΔT cut to identify π^-, according to Table 5.7

.

PHOTONS IDENTIFICATION

To identify photons, the same process of identification and energy-momentum corrections of Section 4.3 is followed. The only difference corresponds to the energy correction factors.

As a reminder, the correction on the reconstructed photon's energy is for bringing the π^0 mass closer to its nominal PDG value. The process to obtain the correction factors is detailed in Ref. [20], and they are applied as:

$$E'_\gamma = \frac{E_\gamma}{k}, \tag{5.8}$$

where E'_γ is the corrected photon energy, $E_\gamma = \max\left(E_{tot}, E_{in} + E_{out}\right)/0.272$ is the energy of the reconstructed photon, and k is the correction factor, which depends on the uncorrected energy:

$$k(E_\gamma) = k_1 + \frac{k_2}{E_\gamma} + \frac{k_3}{E_\gamma^2}, \tag{5.9}$$

where parameters $k_{1,2,3}$ are detailed in Table 5.8. For the reconstructed photons, these values do not depend on the target.

k_1	k_2	k_3
1.0×10^0	5.0×10^{-3}	-5.2×10^{-3}

Table 5.8: Reconstructed photon's energy correction factors. Taken from Ref. [20].

OVERVIEW OF CUTS

Similar to the previous section of generated events, the target type is predetermined by the choice of simulation file. On the other hand, the cuts used to filter the data that are precisely maintained to filter the simulation reconstructed events are:

- DIS kinematical cuts. (Eq. 4.26.)
- Cut in the invariant mass of the neutral pions. (Eq. 4.32.)
- Exclusion of neutral kaons cut. (Eq. 4.36.)

OMEGA RECONSTRUCTION AND BACKGROUND SUBTRACTION

Following the same procedure of Sections 4.8 and 5.2, event-mixing is the nominal method for background subtraction. The technique remains the same as the one described in Section 4.11.2, only that now artificial ω mesons are formed from the reconstructed ω mesons, as can be seen in Fig. 5.9.

Figure 5.10 corresponds to an example of the background subtraction procedure. The number of ω mesons is calculated by integrating the subtracted-background distribution over the obtained $\mu \pm 3\sigma$ range. The results of this integration can be seen in Fig. 5.11. For more information, the complete process for all targets and all kinematical bins is presented can be found in Section A.2.3.

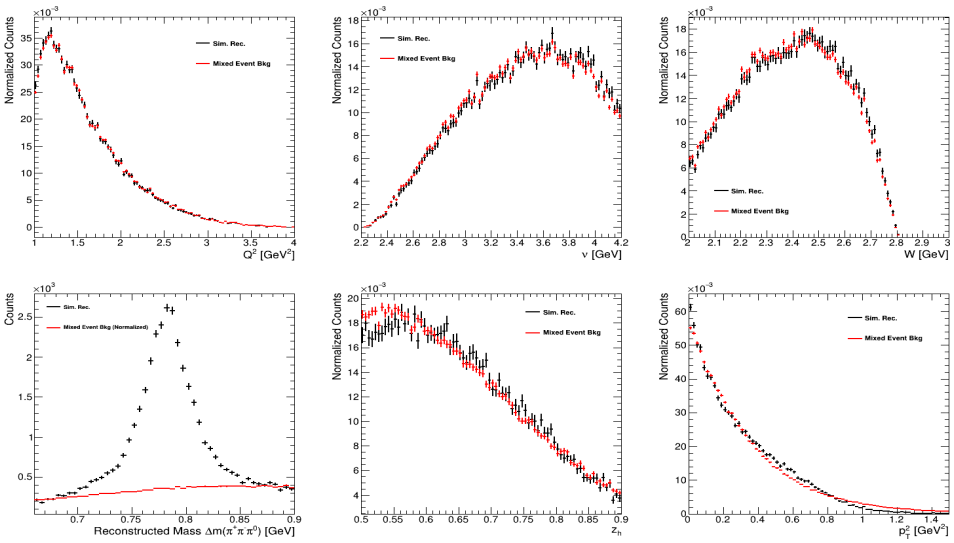

Figure 5.9: Comparison plots between simulation reconstructed of carbon (black) and mixed event background (red) for distinct kinematical variables. From left to right, the upper row corresponds to the electron distributions Q^2, ν, and W, while the lower row presents the ω meson distributions $\Delta m_{\pi^+\pi^-\pi^0}$, z_h, and p_T^2.

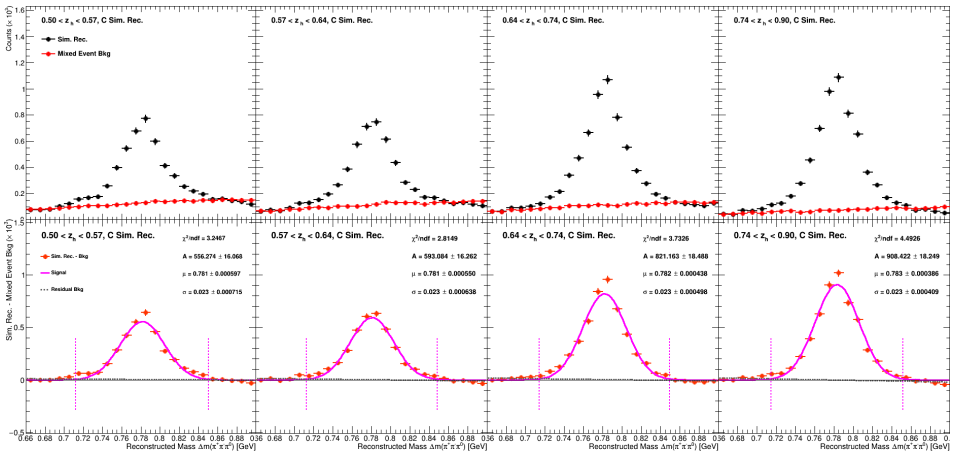

Figure 5.10: Signal extraction procedure after the generation of mixed event background, using reconstructed events from C simulations for each z_h bin. In the upper row, the mixed event background (red) is normalized to match the data (black). In the lower row, the background-subtracted distribution is fitted with a Gaussian (magenta) and a first-order polynomial (gray). The χ^2/ndf of the composite fit is shown. Vertical lines correspond to the $\mu \pm 3\sigma$ range used to integrate the number of ω mesons.

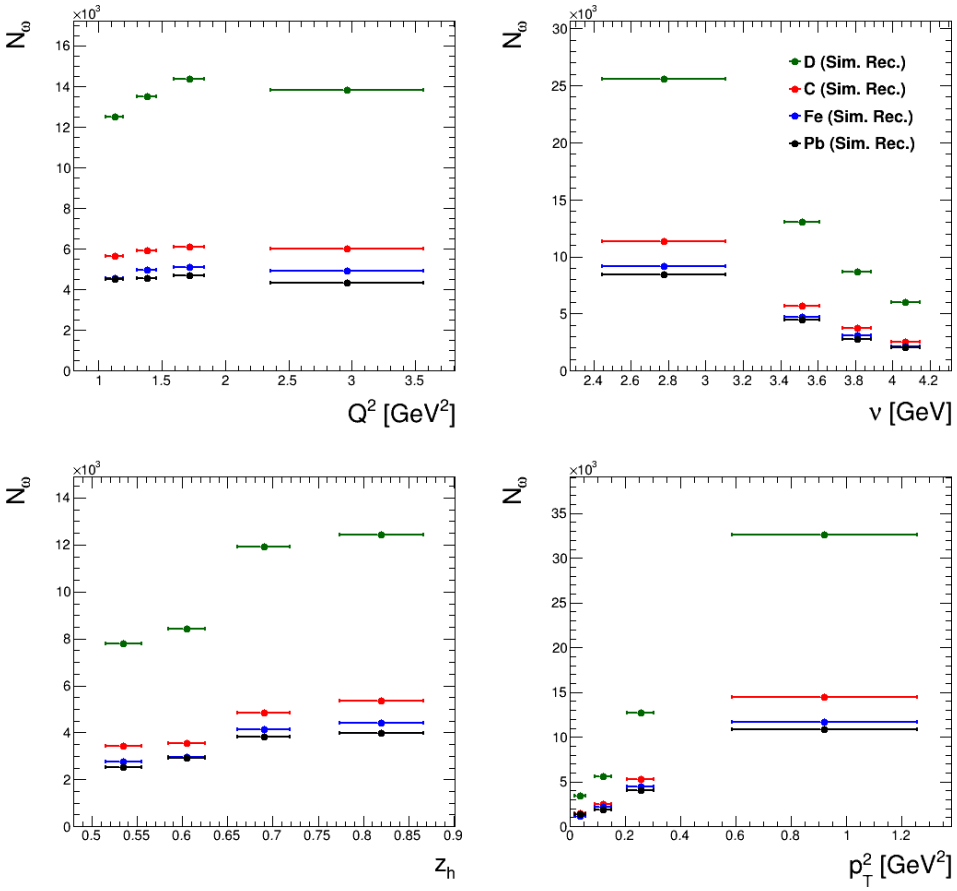

Figure 5.11: Extracted number of reconstructed ω mesons after background subtraction through event mixing, depending on each kinematical variable and target.

5.4 COMPARISON BETWEEN DATA AND SIMULATIONS

Figure 5.12 represents a comparison between one-dimensional distributions from data and the reconstructed simulations. The top three panels of the figure present the electron distributions. In them, a great agreement can be seen for Q^2, however, a fair agreement with slight differences are shown for the ν and W distributions, which may caused by the MC generator LEPTO. On the other hand, in the lower panels of the figure, the data and reconstructed simulations show a great agreement in the z_h distributions of the ω mesons, but not so much for the p_T^2 distribution. The last panel, which refers to the Δm distribution, accurately reflects that only events with ω mesons have been generated and reconstructed, presenting a smaller combinatorial background when compared to the real data.

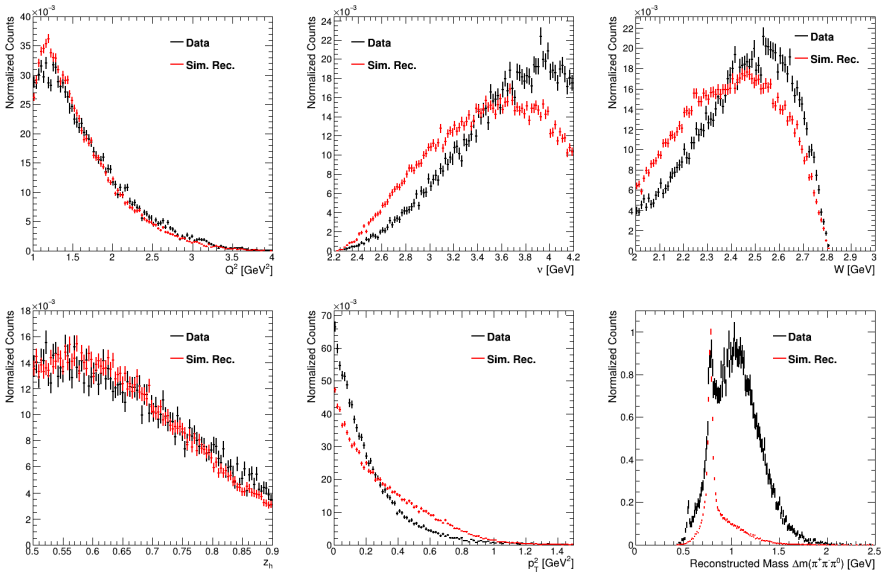

Figure 5.12: Comparison between data (black) and simulation reconstructed events (red). From left to right, the top row shows the distributions of the electron variables: Q^2, ν and W; and the bottom row shows the distributions of the ω meson variables: z_h, p_T^2 and Δm.

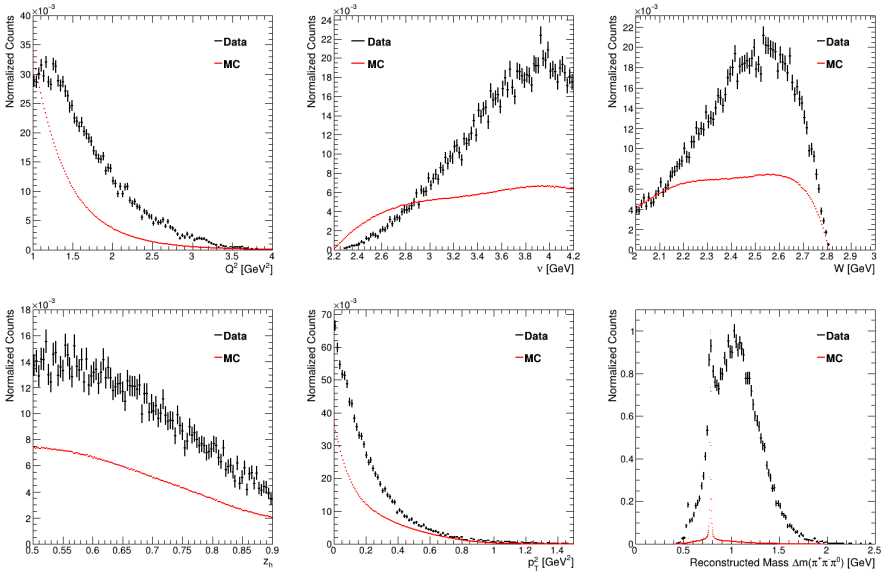

Figure 5.13: Comparison between data (black) and simulation generated events (red). From left to right, the top row shows the distributions of the electron variables: Q^2, ν and W; and the bottom row shows the distributions of the ω meson variables: z_h, p_T^2 and Δm.

5.5 ACCEPTANCE CORRECTION

In the detection of high-energy particles, many external and geometrical factors can affect and limit the measurements. For example: the different sizes, shapes, position of the experiment's nuclear targets; the edges of the detectors' components; inefficient wires; false track reconstructions, etc. To reduce the impact of these factors, one can generate events and reconstruct their decays and interactions with the different parts of the experimental equipment–already described in the previous sections. With these new datasets, one can define the probability $A_p(\vec{x})$ that the detector accepts the generated particle p at a given bin $(\vec{x})$ as [68]:

$$A_p(\vec{x}) = \frac{N_p^{rec}(\vec{x})}{N_p^{gen}(\vec{x})} \tag{5.10}$$

where $N_p^{rec}(\vec{x})$ is the number of reconstructed or *accepted* particles in a bin $(\vec{x})$, and $N_p^{gen}(\vec{x})$ is the number of generated or *thrown* particles in a bin $(\vec{x})$. This term is known as the Acceptance Correction Factor, and its statistical error is given by the Poisson distribution[1]:

$$\sigma_A(\vec{x}) = \sqrt{\frac{A_p(\vec{x})\left(1 - A_p(\vec{x})\right)}{N_p^{gen}(\vec{x}) - 1}}. \tag{5.11}$$

Figure 5.14 represents the Acceptance Correction Factors of electrons depending on Q^2 and ν, while Table 5.9 gives the integrated electron correction factors to be applied for all bins of the ω meson variables, such as z_h and p_T^2. Most importantly, Figure 5.15 presents the Acceptance Correction Factors of the ω mesons depending on the four variables of interest: Q^2, ν, z_h, and p_T^2.

Target	Integrated A_{e^-}
D	$0.32786 \pm 7.832 \times 10^{-5}$
C	$0.32869 \pm 1.163 \times 10^{-4}$
Fe	$0.32483 \pm 1.280 \times 10^{-4}$
Pb	$0.32518 \pm 1.336 \times 10^{-4}$

Table 5.9: Integrated Acceptance Correction Factors of DIS electrons, for each target.

1 Technically, this calculation is easily done with ROOT [51] by using the option `"B"`–binomial error–when dividing histograms with the `Divide()` member function.

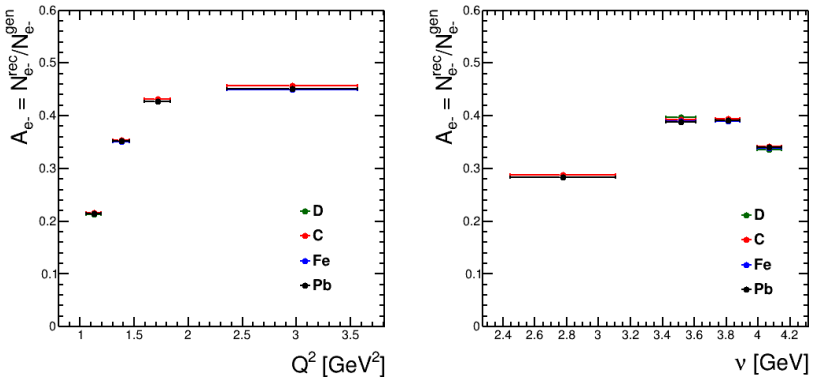

Figure 5.14: Acceptance Correction Factors of DIS electrons depending on Q^2 and ν, for each target.

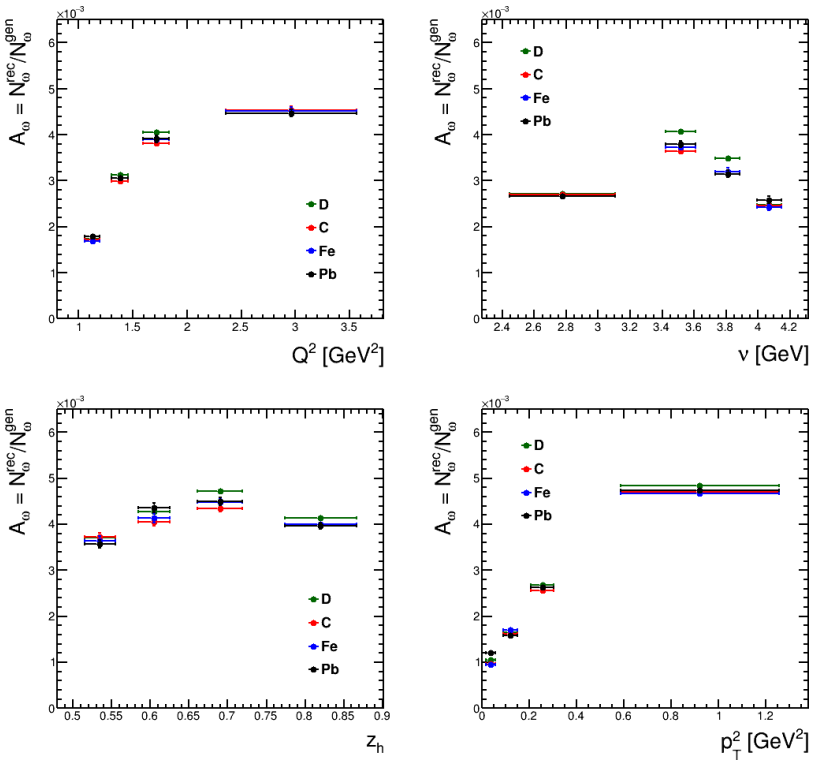

Figure 5.15: Acceptance Correction Factors of the ω mesons depending on Q^2, ν, z_h and p_T^2, for each target.

Consequently, the correction factor is applied to the number of detected particles on a bin-by-bin basis:

$$N_p^{corr}(\vec{x}) = \frac{N_p^{data}(\vec{x})}{A_p(\vec{x})}. \tag{5.12}$$

This implies that the new Acceptance Corrected Multiplicity Ratio, ${R'_A}^h$, should be:

$$ {R'_A}^h(Q^2,\nu,z_h,p_T^2) \equiv \frac{\left(\frac{N_h^{corr}(Q^2,\nu,z_h,p_T^2)}{N_e^{corr}(Q^2,\nu)}\right)_A}{\left(\frac{N_h^{corr}(Q^2,\nu,z_h,p_T^2)}{N_e^{corr}(Q^2,\nu)}\right)_D}, \tag{5.13} $$

which can be easily rewritten as:

$$ \Rightarrow {R'_A}^h(Q^2,\nu,z_h,p_T^2) = \Gamma_h(Q^2,\nu,z_h,p_T^2)\, R_A^h(Q^2,\nu,z_h,p_T^2), \tag{5.14} $$

where $R_A^h(Q^2,\nu,z_h,p_T^2)$ is the previously defined and uncorrected Multiplicity Ratio (MR), and $\Gamma_h(Q^2,\nu,z_h,p_T^2)$ corresponds to the ratio of Acceptance Correction Factors.

$$ \Gamma_h(Q^2,\nu,z_h,p_T^2) \equiv \frac{\left(\frac{A_e(Q^2,\nu)}{A_h(Q^2,\nu,z_h,p_T^2)}\right)_A}{\left(\frac{A_e(Q^2,\nu)}{A_h(Q^2,\nu,z_h,p_T^2)}\right)_D}, \tag{5.15} $$

which is represented in Fig. 5.16.

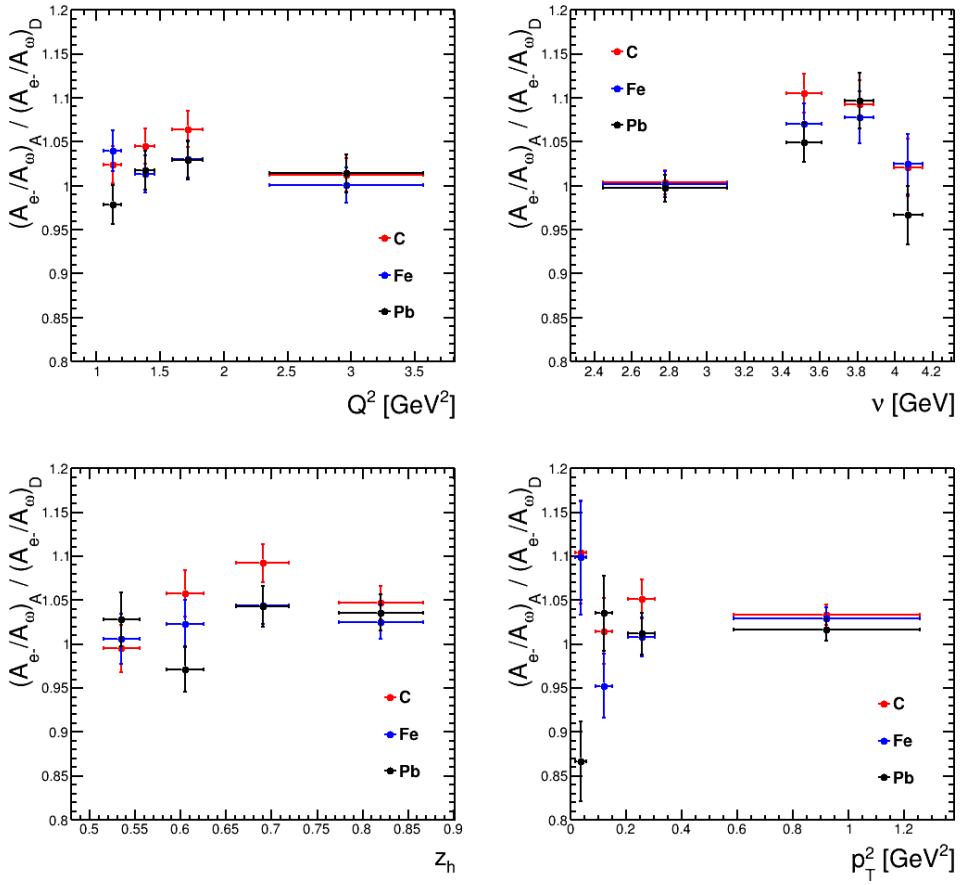

Figure 5.16: Ratio of Acceptance Correction Factors of the ω mesons depending on Q^2, ν, z_h and p_T^2, for each target.

6 RESULTS AND DISCUSSION

The objective of this chapter is to report the results obtained for the Hadronic Multiplicity Ratio (MR) of the ω meson in Section 6.1, and to discuss how these results indicate a promising future for the upcoming collaborations and experiments in Section 6.3.

6.1 MULTIPLICITY RATIO RESULTS

To recapitulate, the observable of interest is the Multiplicity Ratio (MR), for which its definition can be found in Eq. 2.40. An important component of this observable is the number of DIS electrons, which was extracted in Section 4.10, and the Acceptance Corrections, which were calculated in Chapter 5 upon the generation and reconstruction of MC simulations.

The following figures represent the obtained results of one-dimensional MRs as a function of the nuclear targets C, Fe and Pb, and the kinematical variables Q^2, ν, z_h and p_T^2.

- Figure 6.1 represents the ω MR obtained after the data and background fitting method described in Section 4.11.1.
- Figure 6.2 represents the ω MR obtained after background subtraction through event mixing, described in Section 4.11.2.
- Figure 6.3 represents an overlayed comparison of both ω MR results obtained with background fitting and event mixing.
- Figure 6.4 represents an overlayed comparison of the ω MR results obtained with event mixing, with and without the application of Acceptance Correction, described in Section 5.5.
- Figure 6.5 represents the final ω MR results obtained with event mixing and Acceptance Correction.

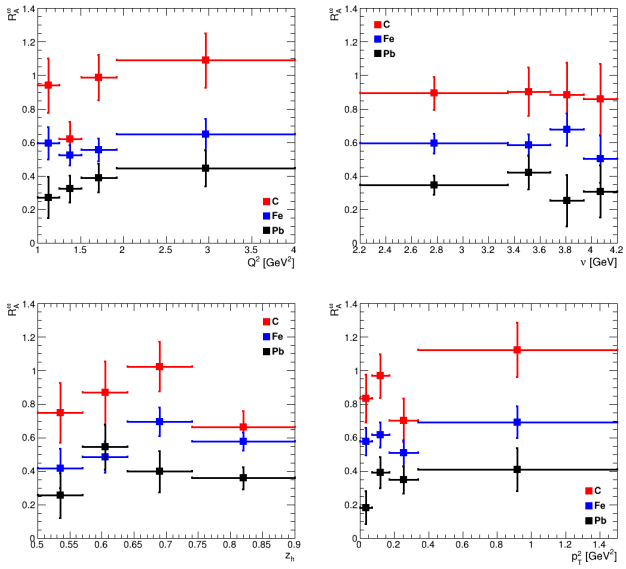

Figure 6.1: Multiplicity Ratios of the ω meson as a function of the nuclear targets C (red), Fe (blue) and Pb (black), and the kinematical variables Q^2, ν, z_h and p_T^2. These results were particularly obtained by extracting the number of ω mesons after the data and background fitting method described in Section 4.11.1. The presented MRs are not Acceptance corrected.

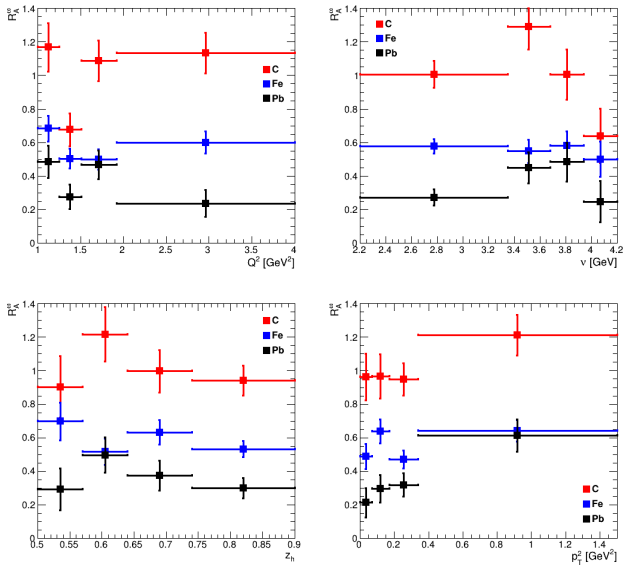

Figure 6.2: Multiplicity Ratios of the ω meson as a function of the nuclear targets C (red), Fe (blue) and Pb (black), and the kinematical variables Q^2, ν, z_h and p_T^2. These results were particularly obtained by extracting the number of ω mesons after the event mixing method described in Section 4.11.2. The presented MRs are not Acceptance corrected.

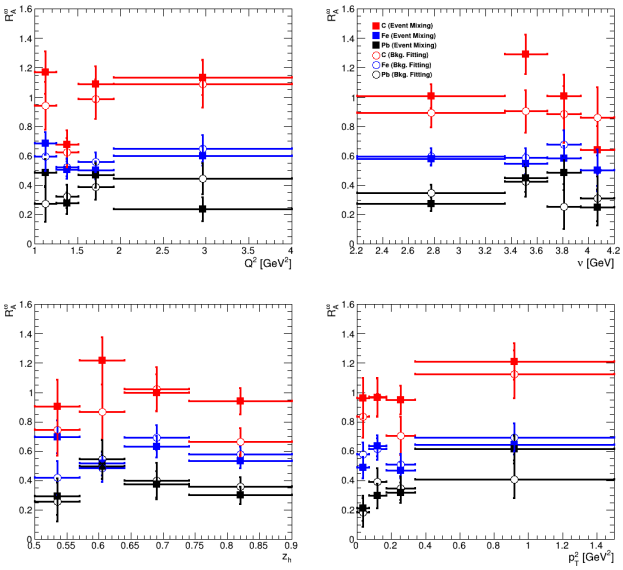

Figure 6.3: Multiplicity Ratios of the ω meson as a function of the nuclear targets C (red), Fe (blue) and Pb (black), and the kinematical variables Q^2, ν, z_h and p_T^2. This plot represents a comparison between the data and background fitting method (hollow circles) and the event mixing method (solid squares). The presented MRs are not Acceptance corrected.

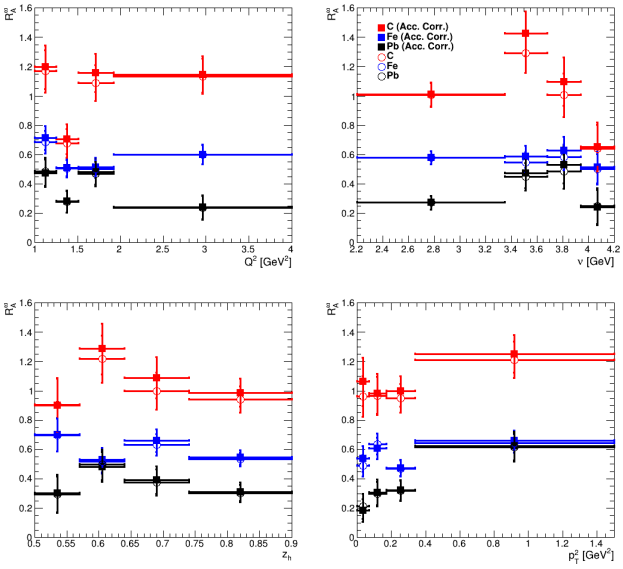

Figure 6.4: Multiplicity Ratios of the ω meson as a function of the nuclear targets C (red), Fe (blue) and Pb (black), and the kinematical variables Q^2, ν, z_h and p_T^2. These results were particularly obtained by extracting the number of ω mesons after the event mixing method described in Section 4.11.2. This plot represents a comparison uncorrected MR (hollow circles) and acceptance-corrected MR (solid squares).

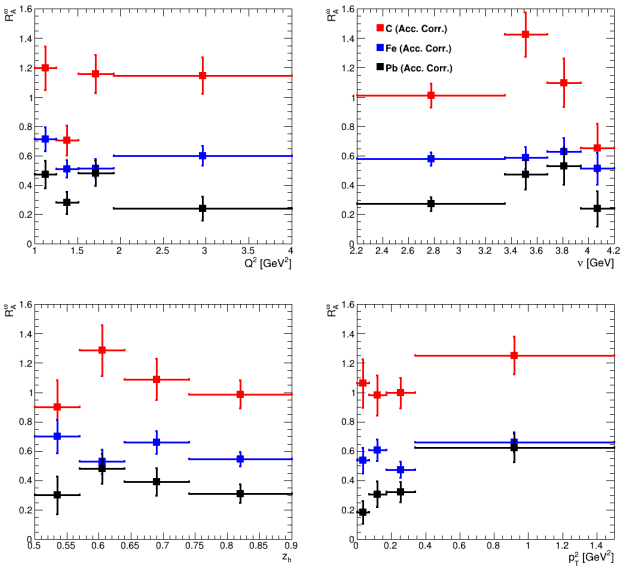

Figure 6.5: Acceptance-corrected Multiplicity Ratios of the ω meson as a function of the nuclear targets C (red), Fe (blue) and Pb (black), and the kinematical variables Q^2, ν, z_h and p_T^2. These results were particularly obtained by extracting the number of ω mesons after the event mixing method described in Section 4.11.2, and were subsequently corrected with the Acceptance Correction Factors described in Section 5.5.

Fig. 6.5 presents one-dimensional Multiplicity Ratio (MR) of the ω meson depending on the kinematical variables Q^2, ν, z_h, and p_T^2. Even though there are 4 bins and high statistical uncertainties, one can see in all the panels a strong dependence on the nuclear size: it is always true that the MR for Carbon is greater than the MR for Iron, and the MR for Iron is greater than the MR for Lead. In conclusion, the nuclear environment does attenuate the production of the ω meson.

The top left panel of Fig. 6.5 pictures how the MR subtlety decreases when increasing in Q^2. This result is in agreement with previous analyses on the hadronization of lighter hadrons, such as the charged pions [18].

As seen earlier, ν is a variable that represents the energy of the virtual-hadron that interacts with a quark from the target. Generally, one would expect more particles to come out when increasing the energy scale of the interaction. However, in top right panel of Fig. 6.5, a plot of MR vs. ν, the trend is unclear. Contrary to expectations, the MR of the first bin is greater than the MR of the last bin for all target runs.

The bottom left panel of Fig. 6.5 is a plot of MR vs. z_h, where, excluding the first bin, the MR seems to decrease when increasing in z_h for Carbon and Lead, which agrees with the observed behavior in the charged pions results [18]. However, when considering the first bin into the picture and Iron results, the trend is unclear.

As seen earlier, the kinematical variable p_T^2 represents the transversal momentum of the measured hadron with respect to the virtual photon direction. This variable should be zero in the case of no further secondary interactions with the nuclear medium after the virtual photon-quark interaction. However, an increase in p_T^2 represents secondary contributions from scatterings with the nuclear medium, deviating the direction of the outgoing hadron (or prehadron). As it can be seen in the bottom right panel of Fig. 6.5, the MR increases with p_T^2 for all targets. Therefore, the production of the ω meson is enhanced by secondary scatterings with the nuclear medium: the *Cronin effect* holds [69].

6.2 NEXT STEPS

The present section corresponds to the sequential steps for the approval of the analysis as a CLAS Analysis Note. The study will be peer-reviewed for its publication in a scientific journal.

First, it has been decided to work together with collaborator Orlando Soto and to merge his analysis of the hadronization of the η meson [21] with the current analysis. This is because of the similarities between the η and ω mesons, such as sharing the same three-pion decay channel, and the similarities between both analyses such as the exact particle ID cuts and background subtraction methods.

As a next step, radiative corrections must be calculated to cover the DIS electron production, such as the Coulomb Corrections [70] and External corrections [71]. On the other hand, to estimate the SIDIS radiative corrections in the hadron production, the HAPRAD software will be used [72]. The software is prepared to correct the production of final state particles, such as charged pions and photons. With these results, it is expected to estimate the impact of corrections for composite particles such as the η and ω mesons.

Statistical uncertainties result from fluctuations arising from measurements based on a finite set of observations. On the other hand, systematic uncertainties correspond to uncertainties associated with the nature of the measurement apparatus, assumptions made by the experimenter, or the model used to make inferences based on the observed data. The latter are often significant contributions to the overall uncertainty in a measurement, in many cases being comparable to the statistical uncertainties. In the joint analysis of η and ω hadronization, several sources of systematic error will be discussed and evaluated. The following sources of uncertainties will be considered: Particle ID, Vertex cuts, Acceptance Correction, and Radiative Corrections.

6.3 OUTLOOK FOR 12 GEV

The results presented in this thesis are the first hadronization studies of the ω meson in the world and indicate a promising future for future hadronization experiments in nuclear environment.

The future is filled with numerous exciting physics programs, projects, and new and improved facilities. During the last decade, the CEBAF accelerator and the CLAS detector have been maintained and upgraded to form CLAS12 [73], a new plan to reach electron energies up to 12 GeV and 10 times increased luminosity. These improvements will make possible for a brand new multidimensional analysis of the ω meson's electroproduction in nuclear environment. It is also worth mentioning other collaborations such as the Electron-Ion Collider (EIC) [74], which was approved for construction at the BNL, and the next run of the Large Hadron Collider (LHC), which provides a new program for the study of heavy ions. In prospective, each new nuclear physics program opens new doors to discover and answer the big questions of QCD.

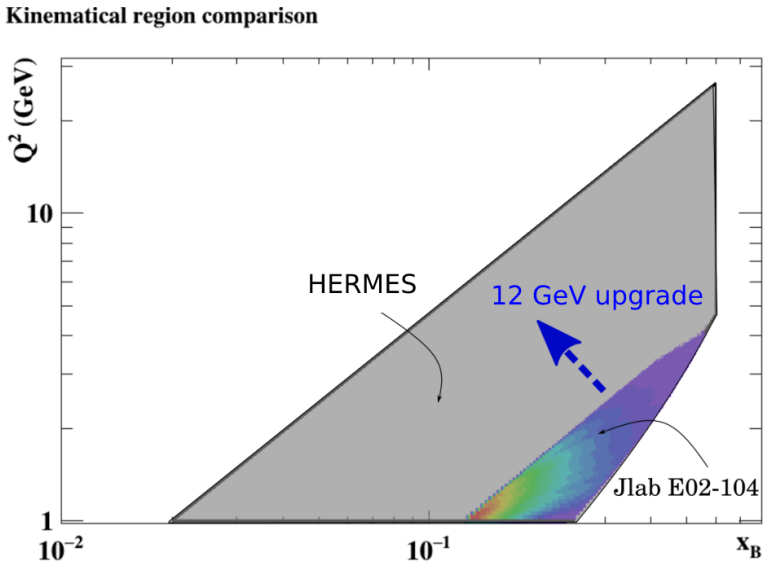

Figure 6.6: Increase of phase space with the CLAS 12 GeV upgrade. Plot taken from Ref. [21].

A

SIGNAL EXTRACTION

A.1 SIGNAL AND BACKGROUND FITTING

This section presents the signal and background fit procedure to extract the ω yields over the different datasets and kinematical bins covered in this work. A detailed explanation of the procedure can be found in Section 4.11.1.

In each of the following panels, the upper plot corresponds to the model of Eq. 4.43 (blue) being fitted to the data (black), with its signal (red) and background (gray) components depicted. The central vertical line correspond to the obtained μ value, while the lateral lines delimit the $\mu \pm 3\sigma$ range. Lower plots are the subsequent pull distributions (magenta) of each fit, with red horizontal lines highlighting a difference of 3 standard deviations away from data.

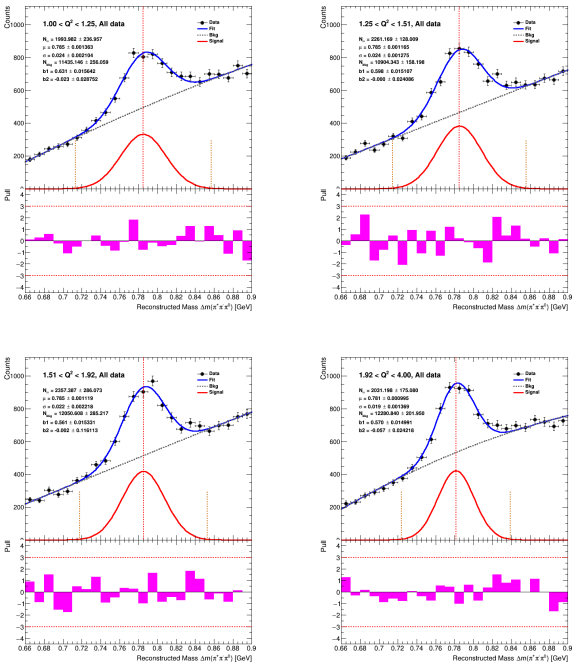

Figure A.1: Background subtraction through a signal and background fit on all data, for each Q^2 bin. A detailed explanation can be found at Sections 4.11.1 and A.1.

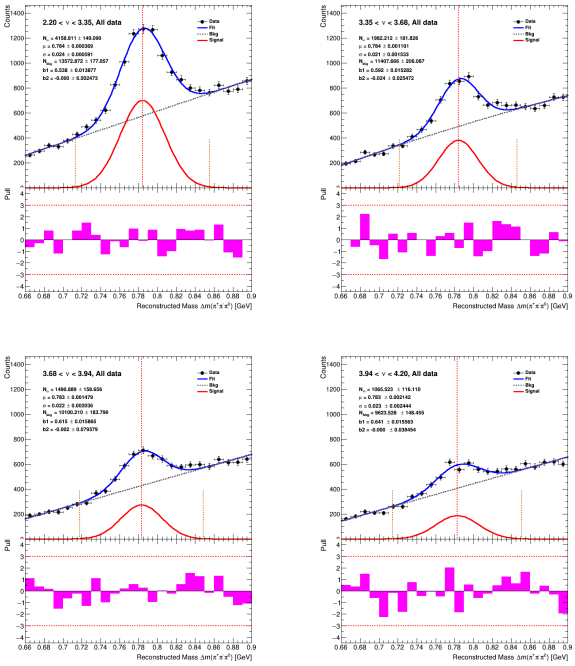

Figure A.2: Background subtraction through a signal and background fit on all data, for each Q^2 bin. A detailed explanation can be found at Sections 4.11.1 and A.1.

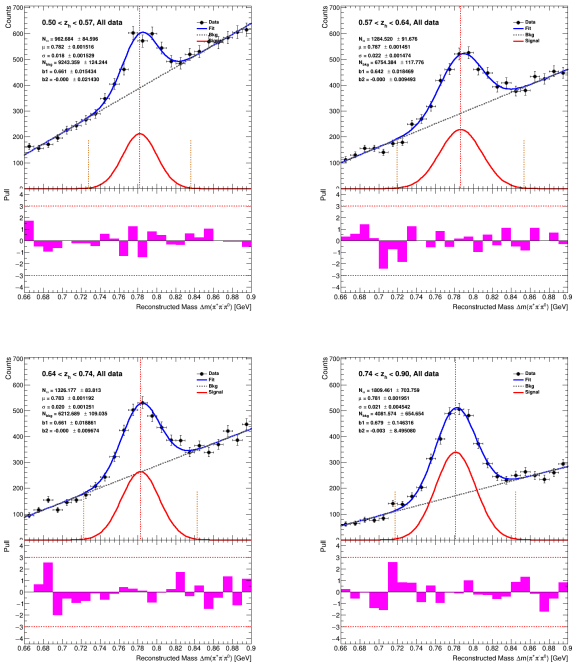

Figure A.3: Background subtraction through a signal and background fit on all data, for each Q^2 bin. A detailed explanation can be found at Sections 4.11.1 and A.1.

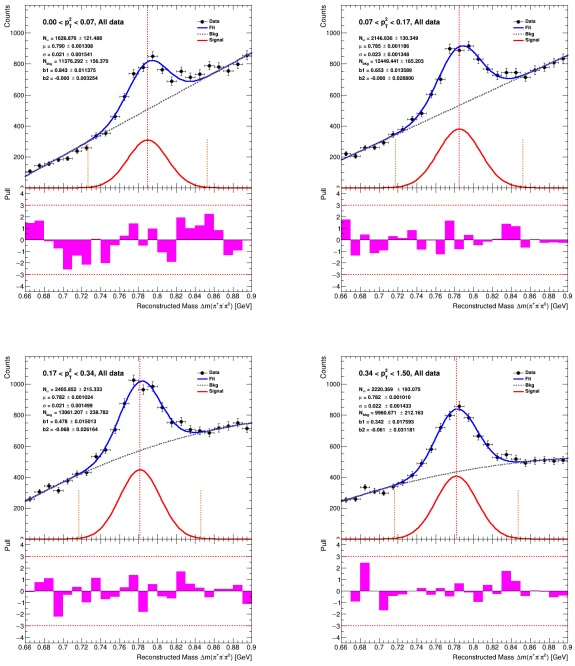

Figure A.4: Background subtraction through a signal and background fit on all data, for each Q^2 bin. A detailed explanation can be found at Sections 4.11.1 and A.1.

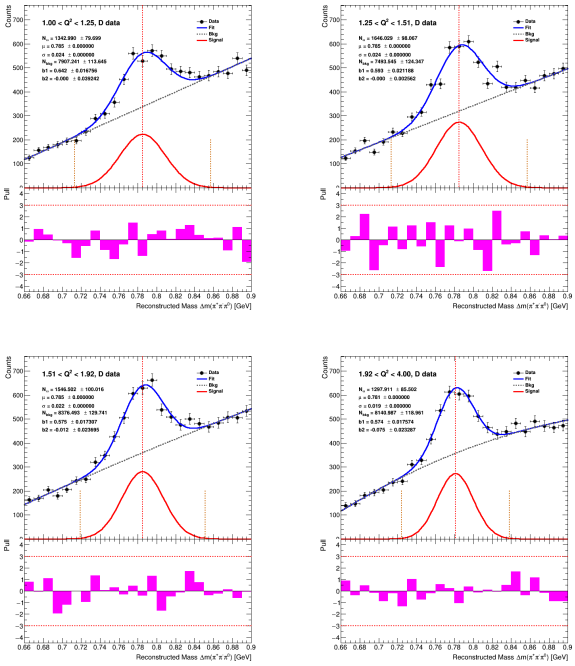

Figure A.5: Background subtraction through a signal and background fit on D data, for each Q^2 bin. A detailed explanation can be found at Sections 4.11.1 and A.1.

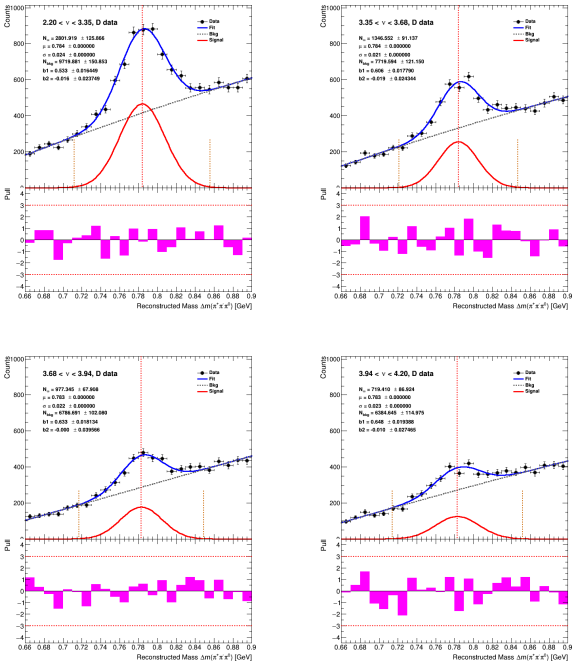

Figure A.6: Background subtraction through a signal and background fit on D data, for each ν bin. A detailed explanation can be found at Sections 4.11.1 and A.1.

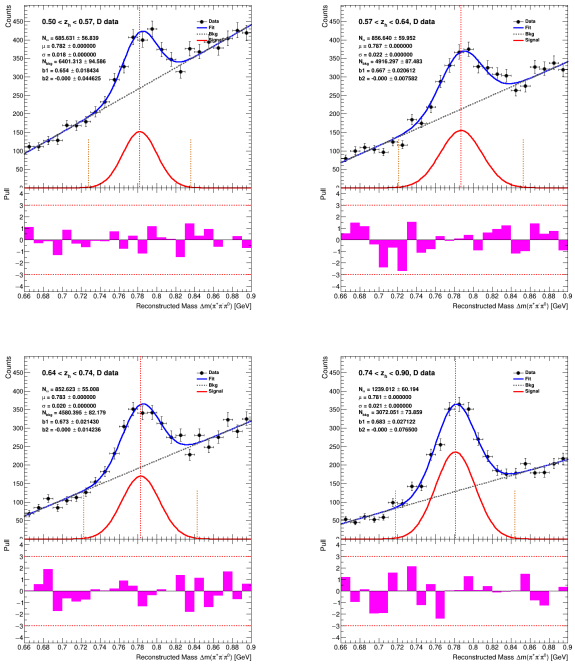

Figure A.7: Background subtraction through a signal and background fit on D data, for each z_h bin. A detailed explanation can be found at Sections 4.11.1 and A.1.

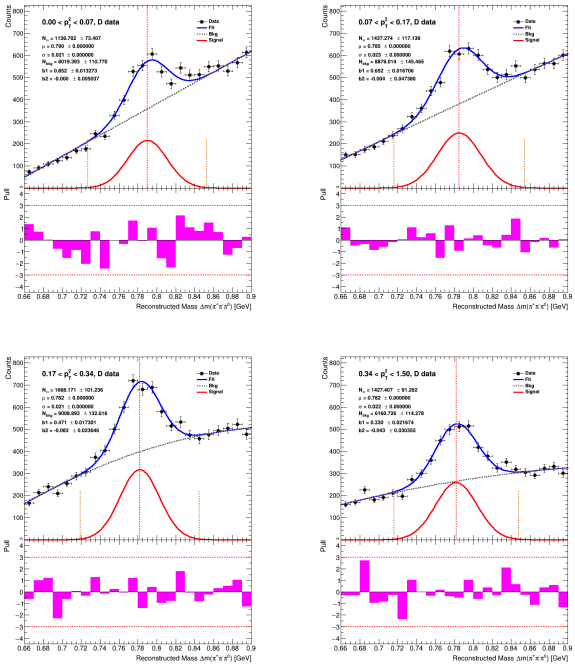

Figure A.8: Background subtraction through a signal and background fit on D data, for each p_T^2 bin. A detailed explanation can be found at Sections 4.11.1 and A.1.

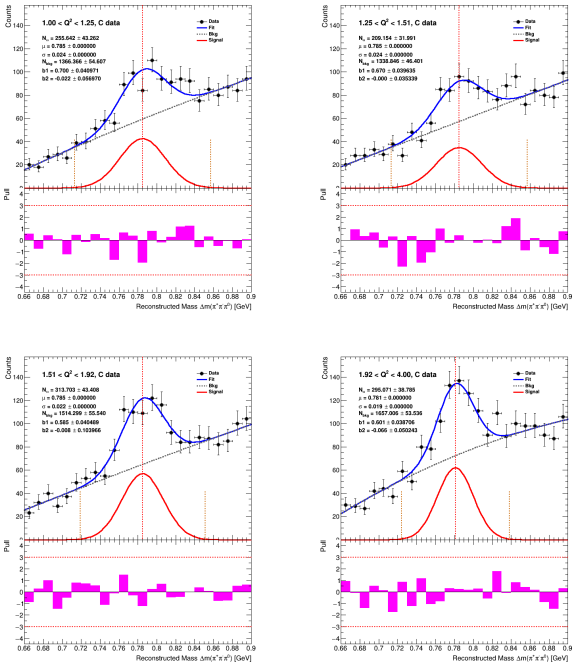

Figure A.9: Background subtraction through a signal and background fit on C data, for each Q^2 bin. A detailed explanation can be found at Sections 4.11.1 and A.1.

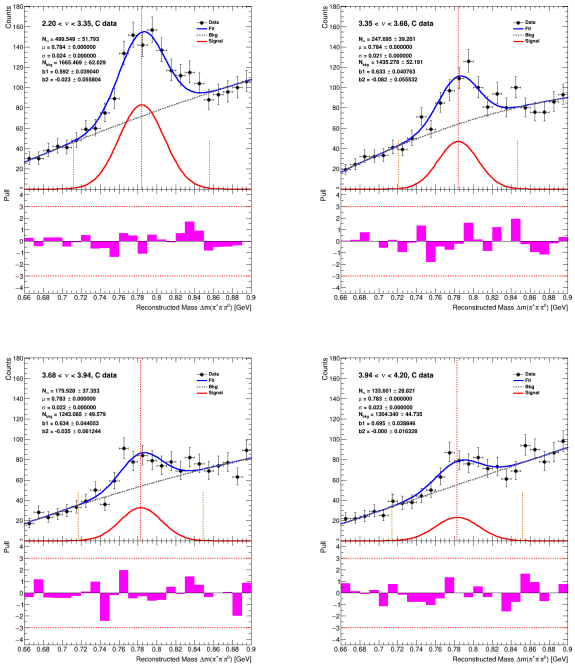

Figure A.10: Background subtraction through a signal and background fit on C data, for each ν bin. A detailed explanation can be found at Sections 4.11.1 and A.1.

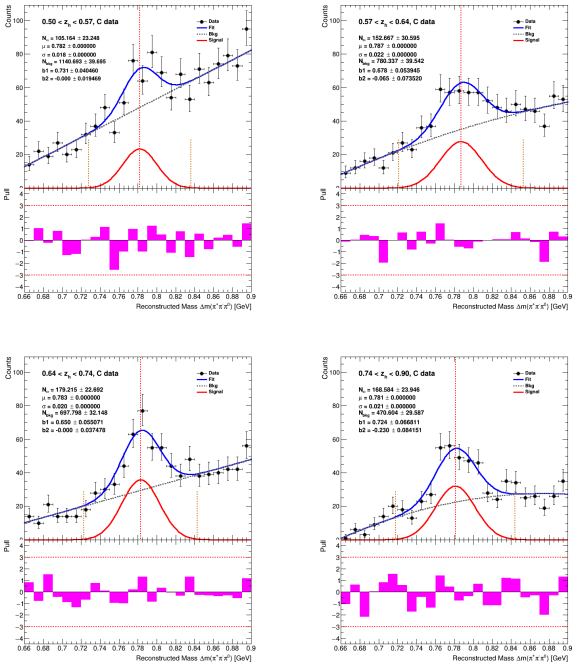

Figure A.11: Background subtraction through a signal and background fit on C data, for each z_h bin. A detailed explanation can be found at Sections 4.11.1 and A.1.

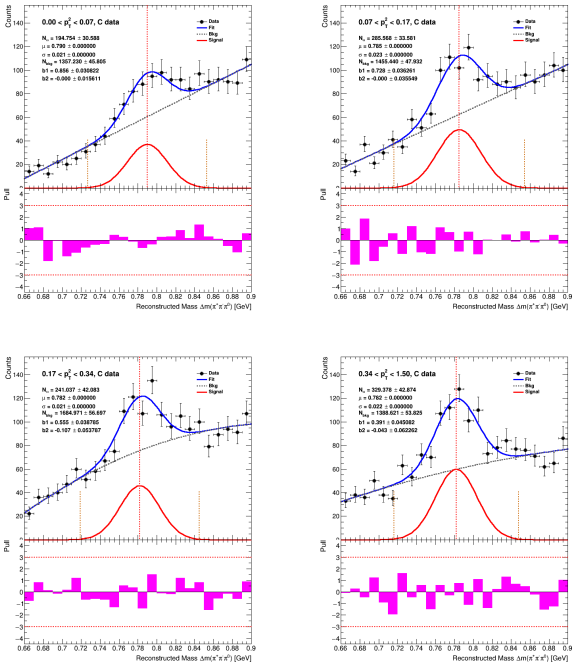

Figure A.12: Background subtraction through a signal and background fit on C data, for each p_T^2 bin. A detailed explanation can be found at Sections 4.11.1 and A.1.

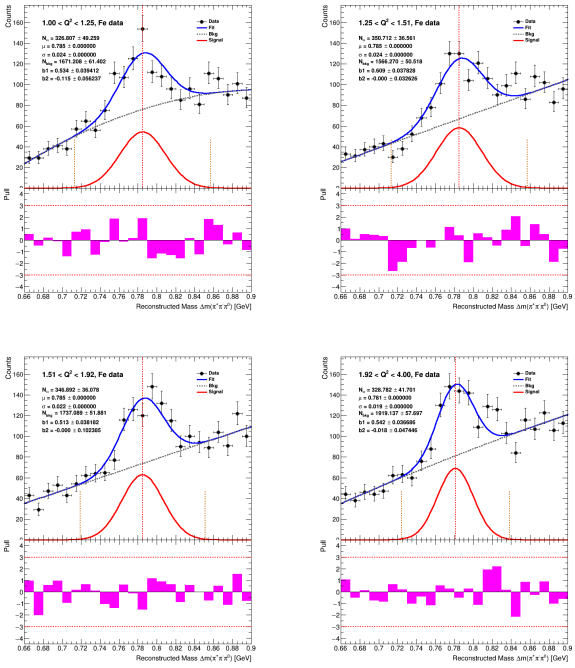

Figure A.13: Background subtraction through a signal and background fit on Fe data, for each Q^2 bin. A detailed explanation can be found at Sections 4.11.1 and A.1.

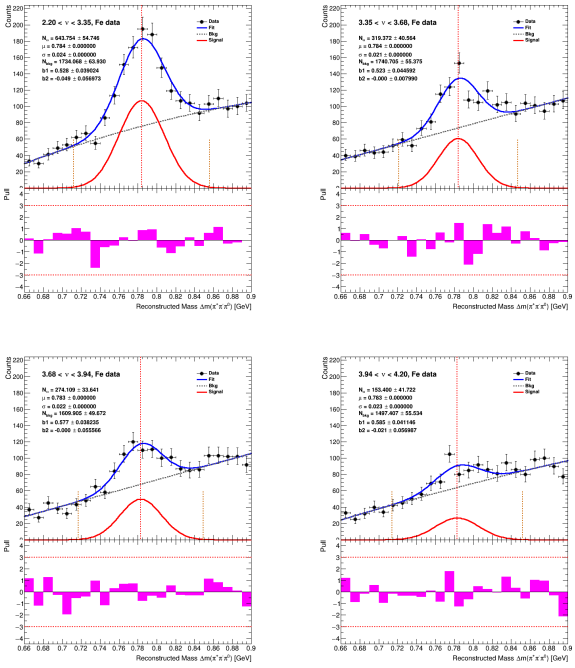

Figure A.14: Background subtraction through a signal and background fit on Fe data, for each ν bin. A detailed explanation can be found at Sections 4.11.1 and A.1.

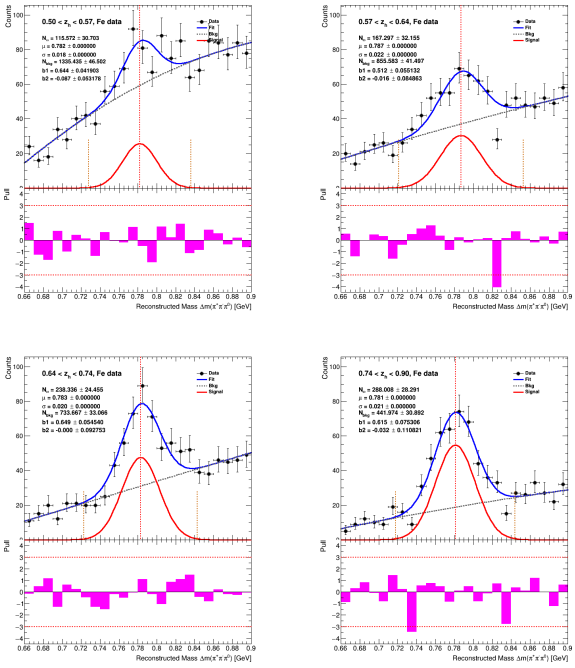

Figure A.15: Background subtraction through a signal and background fit on Fe data, for each z_h bin. A detailed explanation can be found at Sections 4.11.1 and A.1.

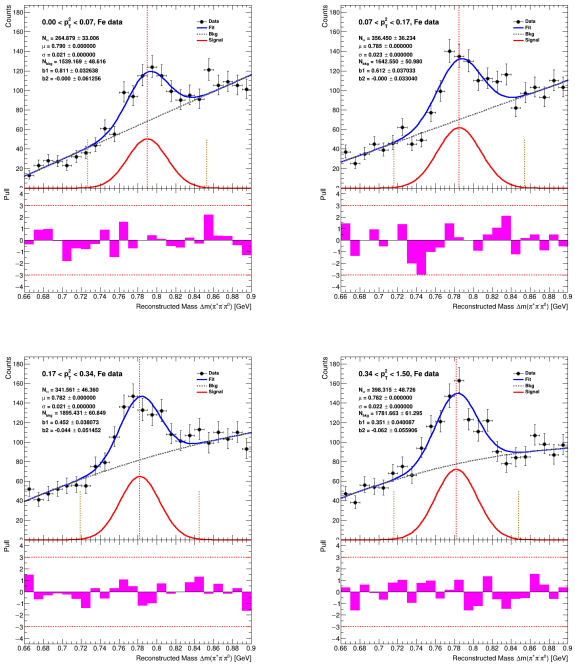

Figure A.16: Background subtraction through a signal and background fit on Fe data, for each p_T^2 bin. A detailed explanation can be found at Sections 4.11.1 and A.1.

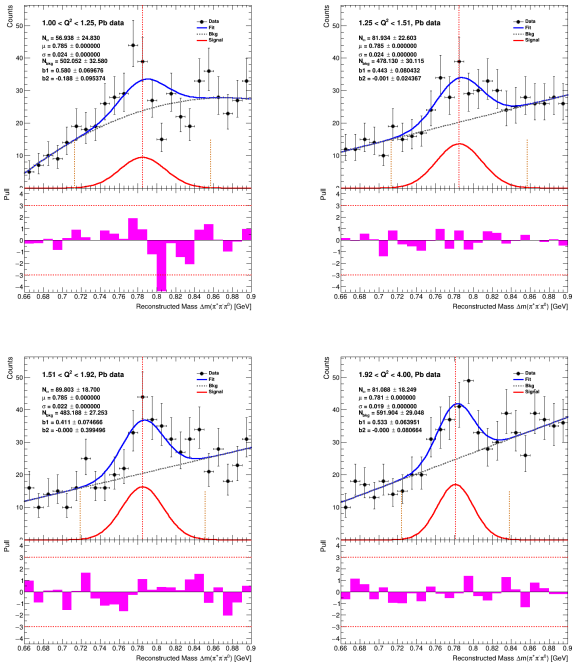

Figure A.17: Background subtraction through a signal and background fit on Pb data, for each Q^2 bin. A detailed explanation can be found at Sections 4.11.1 and A.1.

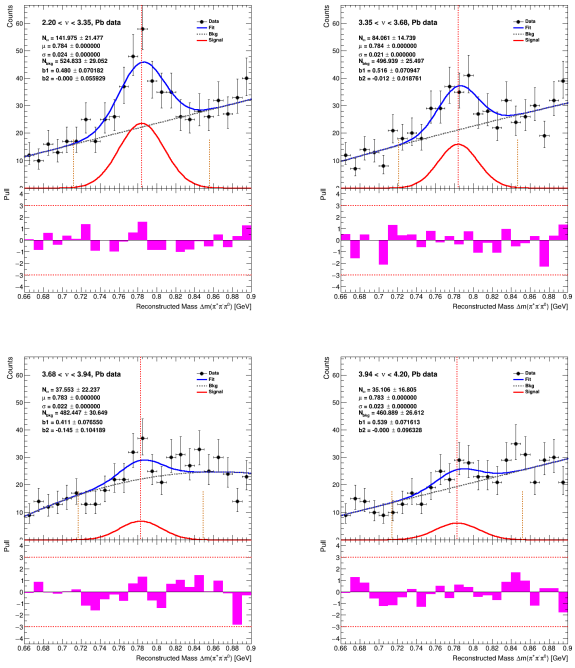

Figure A.18: Background subtraction through a signal and background fit on Pb data, for each ν bin. A detailed explanation can be found at Sections 4.11.1 and A.1.

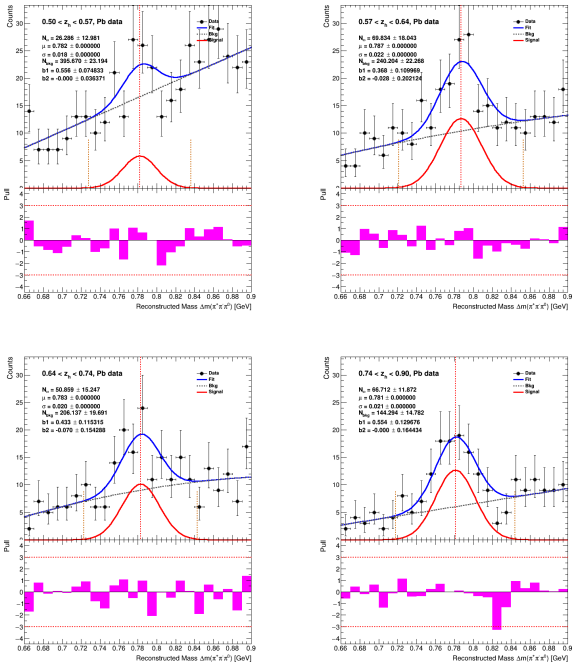

Figure A.19: Background subtraction through a signal and background fit on Pb data, for each z_h bin. A detailed explanation can be found at Sections 4.11.1 and A.1.

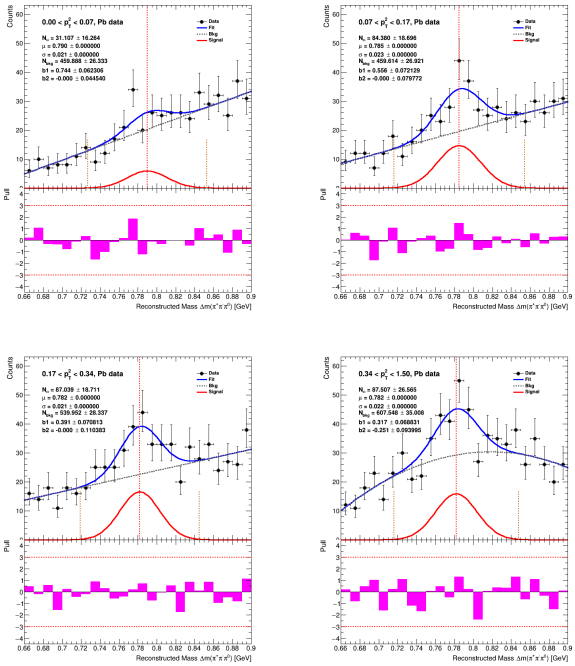

Figure A.20: Background subtraction through a signal and background fit on Pb data, for each p_T^2 bin. A detailed explanation can be found at Sections 4.11.1 and A.1.

A.2 EVENT-MIXING METHOD

This section presents the extraction of ω yields through mixed event background subtraction over the different datasets and kinematical bins covered by this analysis. A detailed explanation of the procedure can be found in Section 4.11.2.

In each of the following figures, the upper row of panels correspond to the data's invariant mass difference distributions (black), with a normalized mixed event background (red). The subtraction of both distributions is presented in the lower row of plots. This resulting background-subtracted distribution is fitted with a Gaussian (magenta) to describe the central signal region and a first-order polynomial (gray) to describe the residual background. The χ^2/ndf of the composite fit is shown. Vertical lines correspond to the $\mu \pm 3\sigma$ range used to integrate the number of ω mesons.

A.2.1 On Data

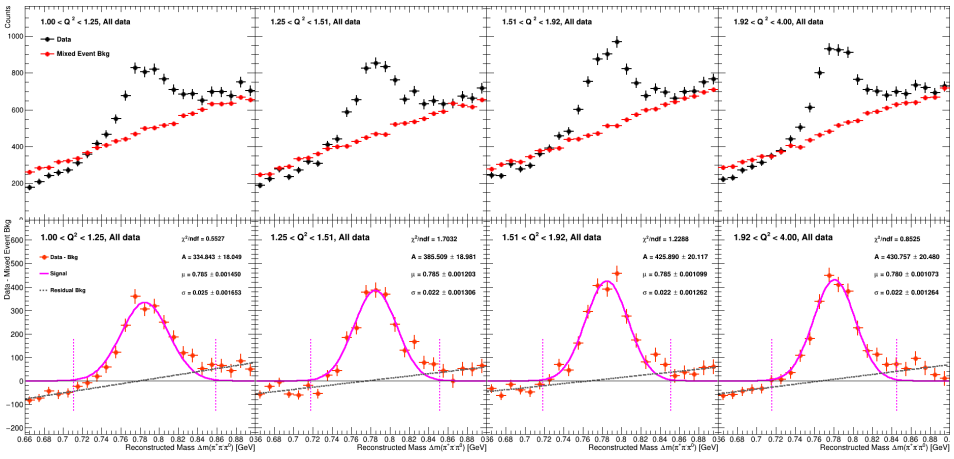

Figure A.21: Background subtraction through event-mixing on all data, for each bin in Q^2. A detailed explanation can be found at Sections 4.11.2 and A.2.

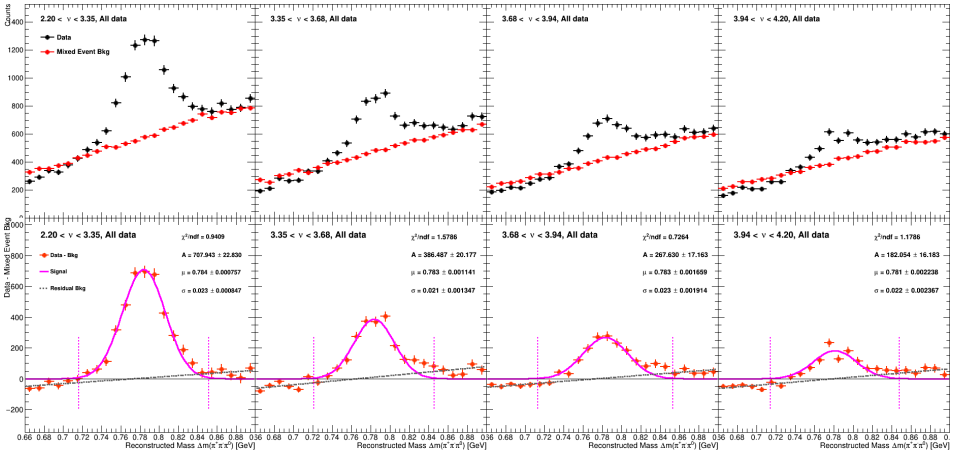

Figure A.22: Background subtraction through event-mixing on all data, for each bin in ν. A detailed explanation can be found at Sections 4.11.2 and A.2.

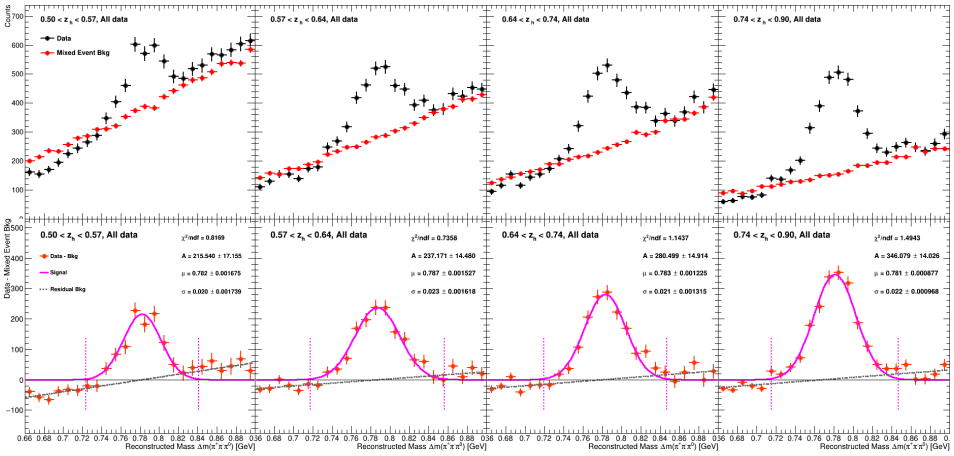

Figure A.23: Background subtraction through event-mixing on all data, for each bin in z_h. A detailed explanation can be found at Sections 4.11.2 and A.2.

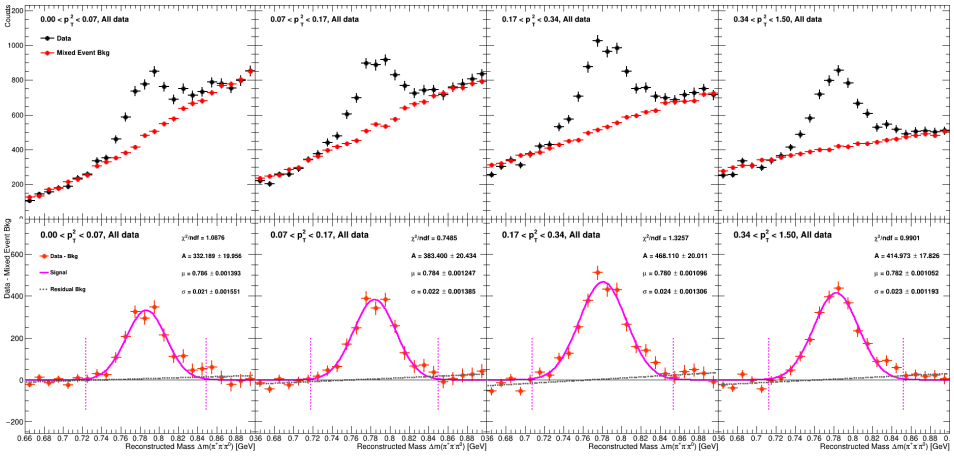

Figure A.24: Background subtraction through event-mixing on all data, for each bin in p_T^2. A detailed explanation can be found at Sections 4.11.2 and A.2.

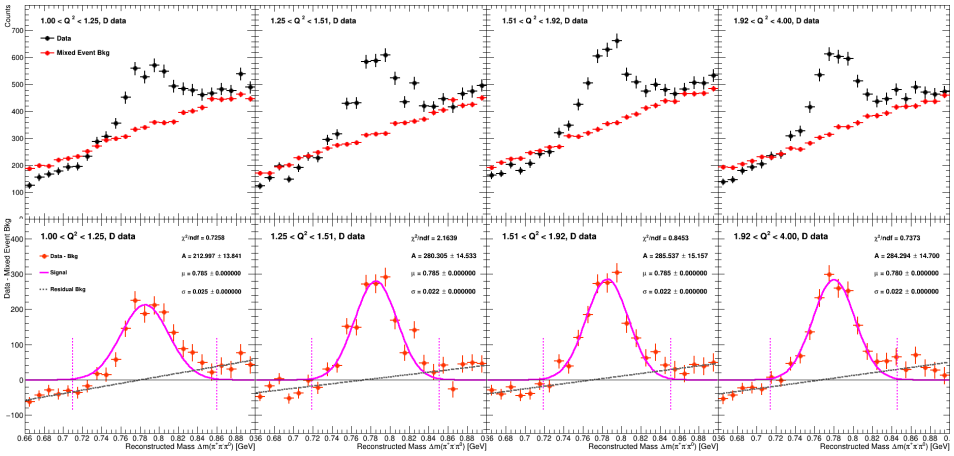

Figure A.25: Background subtraction through event-mixing on D data, for each bin in Q^2. A detailed explanation can be found at Sections 4.11.2 and A.2.

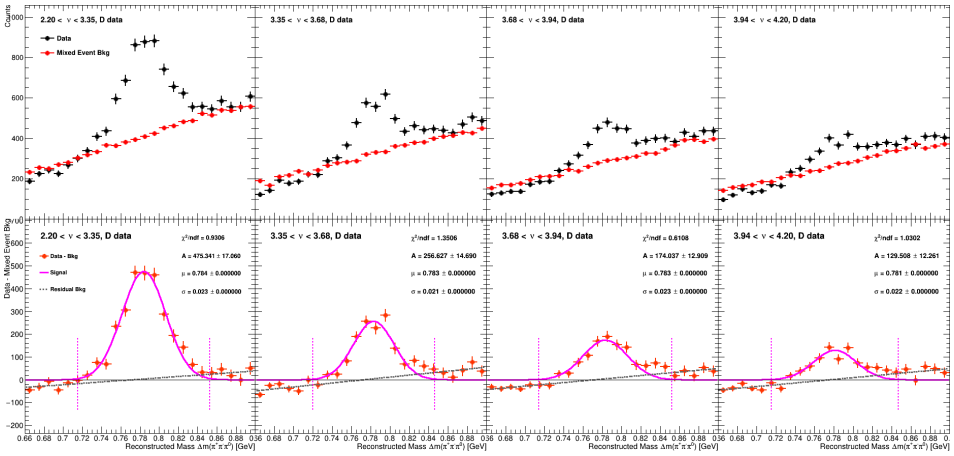

Figure A.26: Background subtraction through event-mixing on D data, for each bin in ν. A detailed explanation can be found at Sections 4.11.2 and A.2.

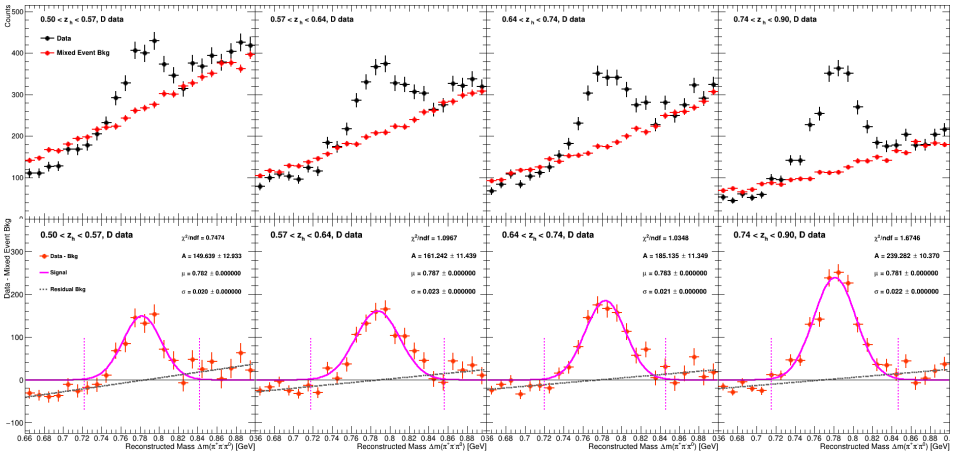

Figure A.27: Background subtraction through event-mixing on D data, for each bin in z_h. A detailed explanation can be found at Sections 4.11.2 and A.2.

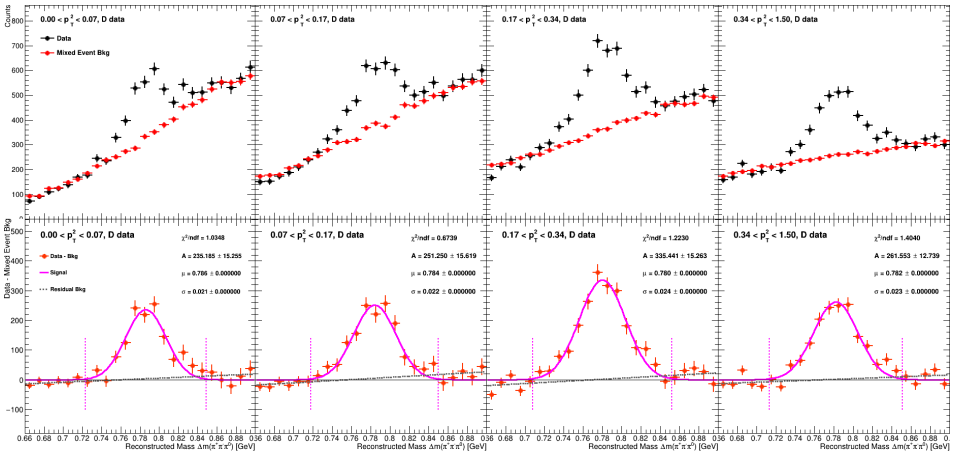

Figure A.28: Background subtraction through event-mixing on D data, for each bin in p_T^2. A detailed explanation can be found at Sections 4.11.2 and A.2.

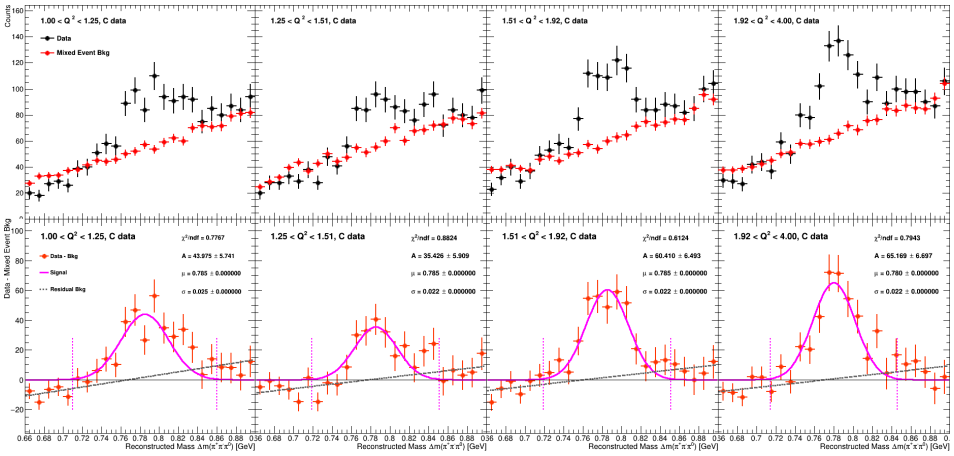

Figure A.29: Background subtraction through event-mixing on C data, for each bin in Q^2. A detailed explanation can be found at Sections 4.11.2 and A.2.

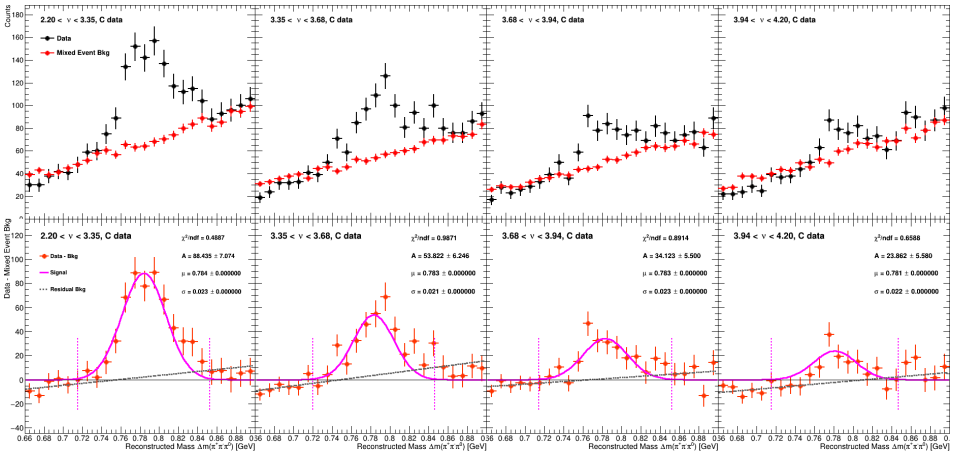

Figure A.30: Background subtraction through event-mixing on C data, for each bin in ν. A detailed explanation can be found at Sections 4.11.2 and A.2.

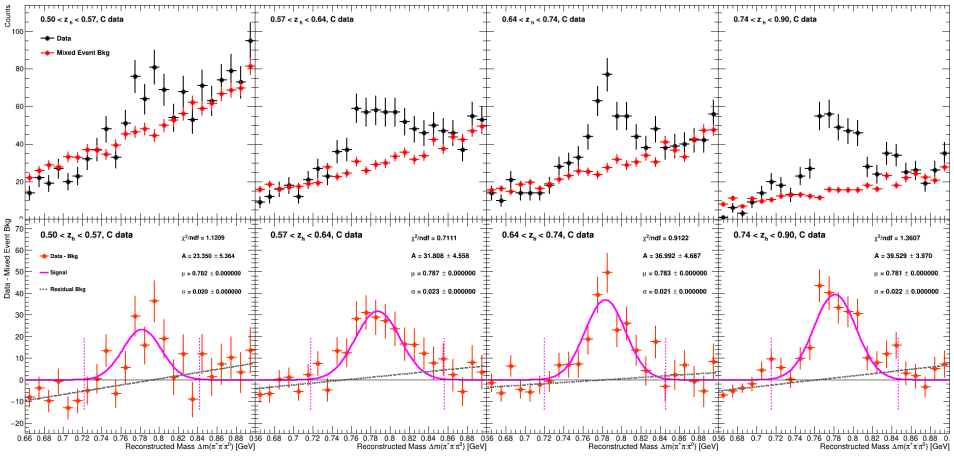

Figure A.31: Background subtraction through event-mixing on C data, for each bin in z_h. A detailed explanation can be found at Sections 4.11.2 and A.2.

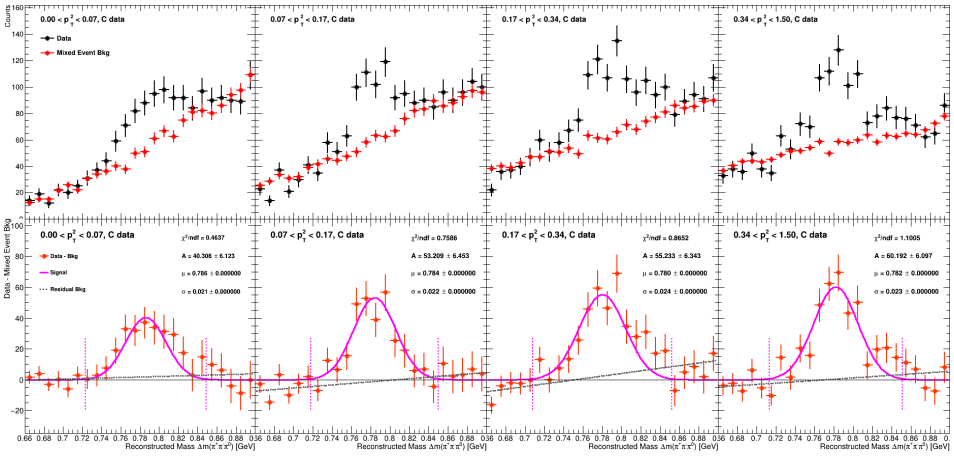

Figure A.32: Background subtraction through event-mixing on C data, for each bin in p_T^2. A detailed explanation can be found at Sections 4.11.2 and A.2.

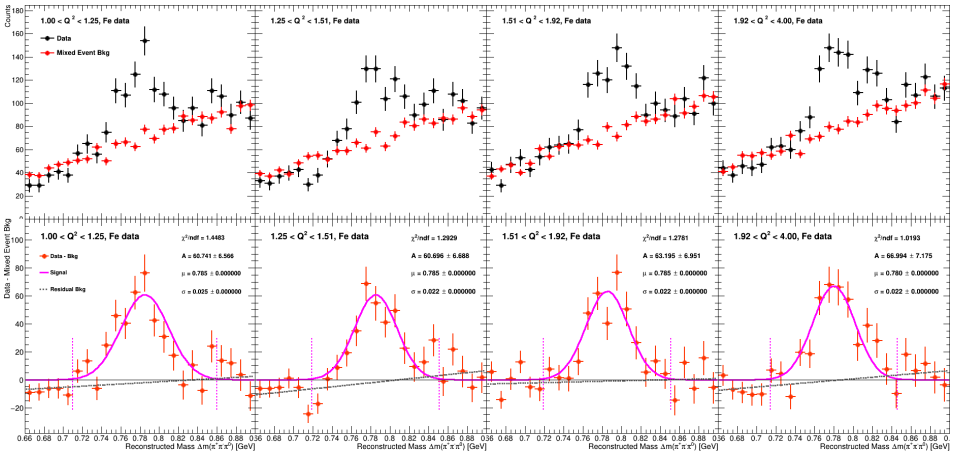

Figure A.33: Background subtraction through event-mixing on Fe data, for each bin in Q^2. A detailed explanation can be found at Sections 4.11.2 and A.2.

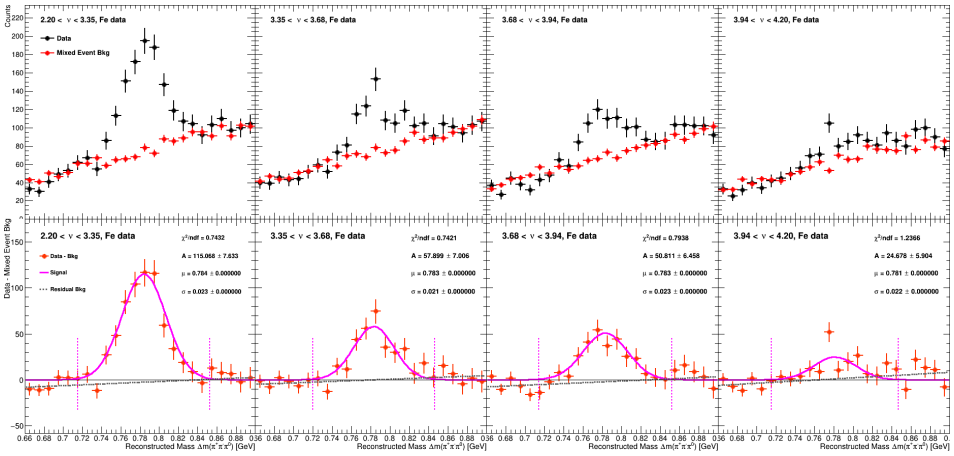

Figure A.34: Background subtraction through event-mixing on Fe data, for each bin in ν. A detailed explanation can be found at Sections 4.11.2 and A.2.

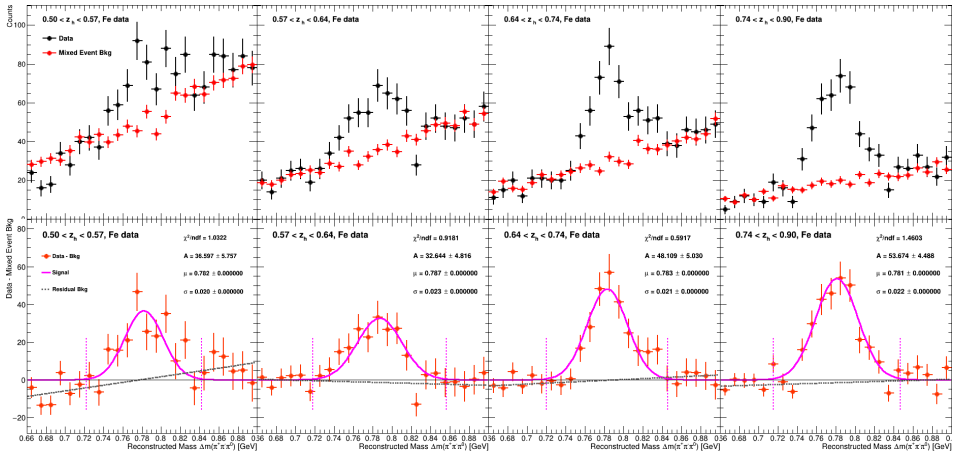

Figure A.35: Background subtraction through event-mixing on Fe data, for each bin in z_h. A detailed explanation can be found at Sections 4.11.2 and A.2.

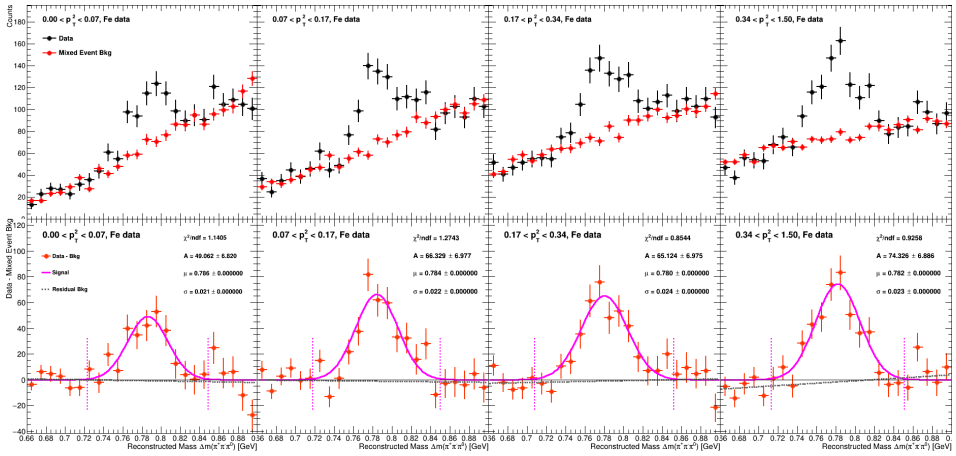

Figure A.36: Background subtraction through event-mixing on Fe data, for each bin in p_T^2. A detailed explanation can be found at Sections 4.11.2 and A.2.

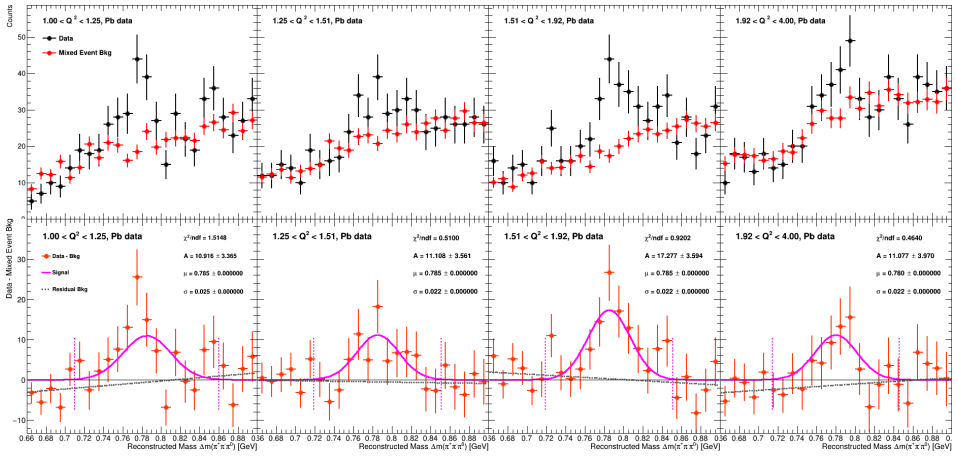

Figure A.37: Background subtraction through event-mixing on Pb data, for each bin in Q^2. A detailed explanation can be found at Sections 4.11.2 and A.2.

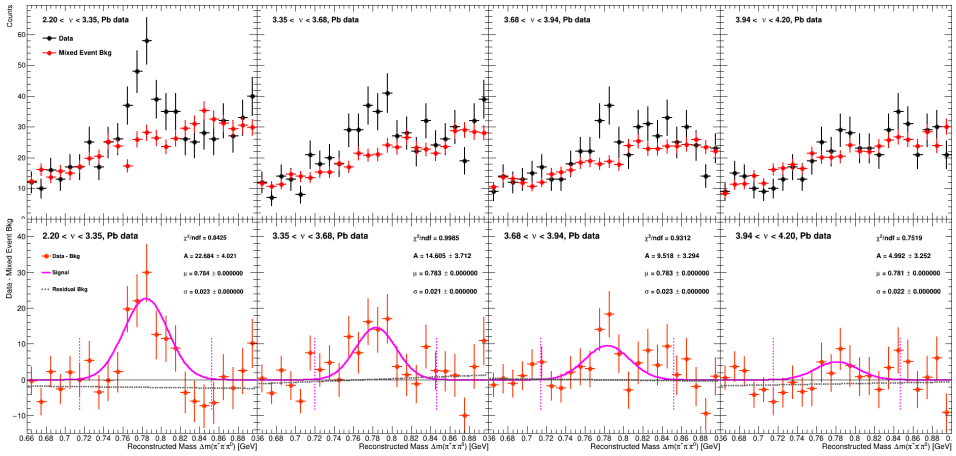

Figure A.38: Background subtraction through event-mixing on Pb data, for each bin in ν. A detailed explanation can be found at Sections 4.11.2 and A.2.

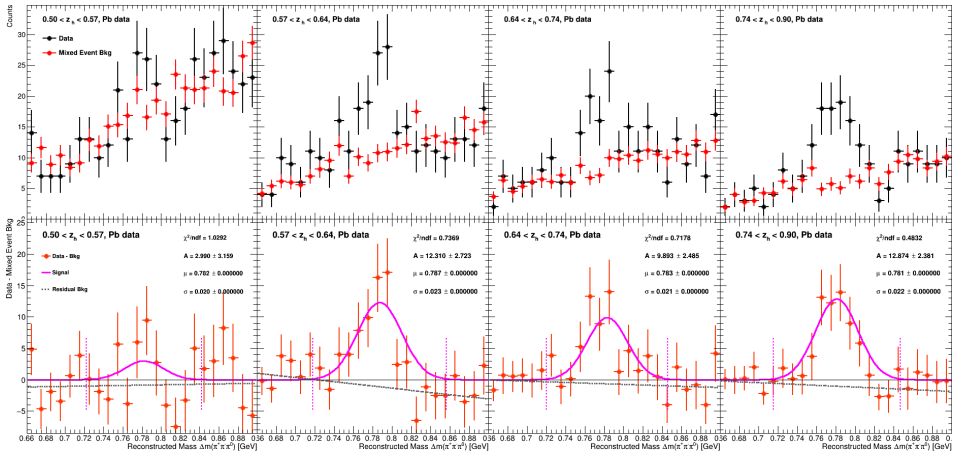

Figure A.39: Background subtraction through event-mixing on Pb data, for each bin in z_h. A detailed explanation can be found at Sections 4.11.2 and A.2.

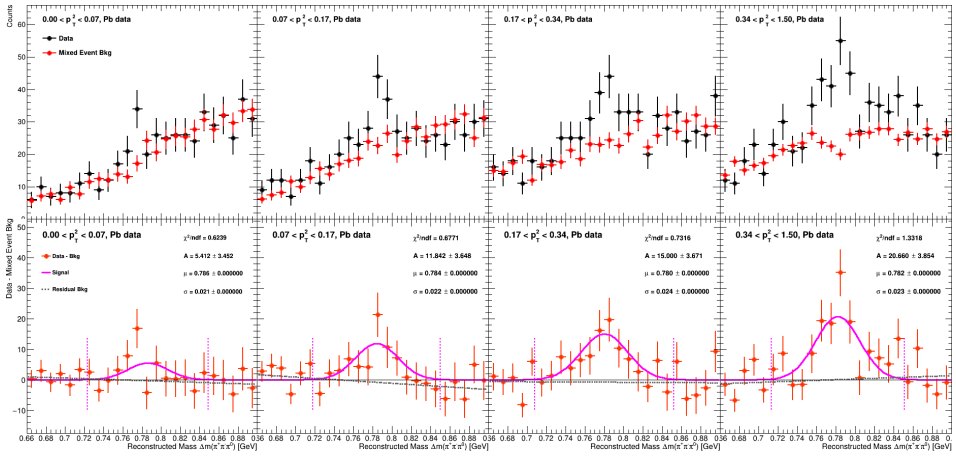

Figure A.40: Background subtraction through event-mixing on Pb data, for each bin in p_T^2. A detailed explanation can be found at Sections 4.11.2 and A.2.

A.2.2 *On Generated Simulations*

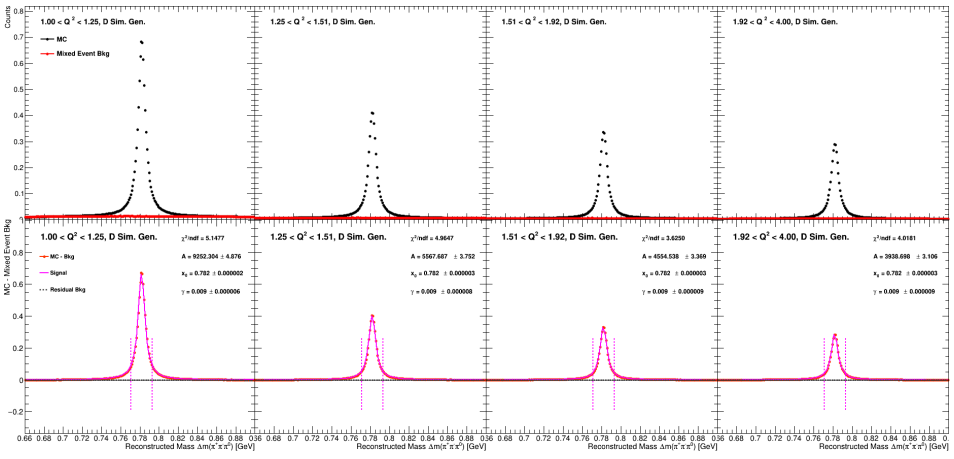

Figure A.41: Background subtraction through event-mixing on MC generated simulations of D, for each bin in Q^2. A detailed explanation can be found at Sections 4.11.2 and A.2.

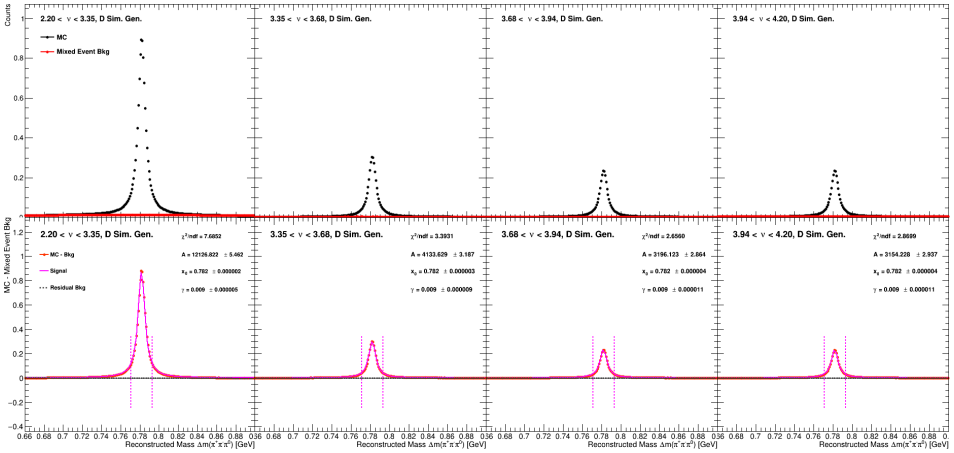

Figure A.42: Background subtraction through event-mixing on MC generated simulations of D, for each bin in ν. A detailed explanation can be found at Sections 4.11.2 and A.2.

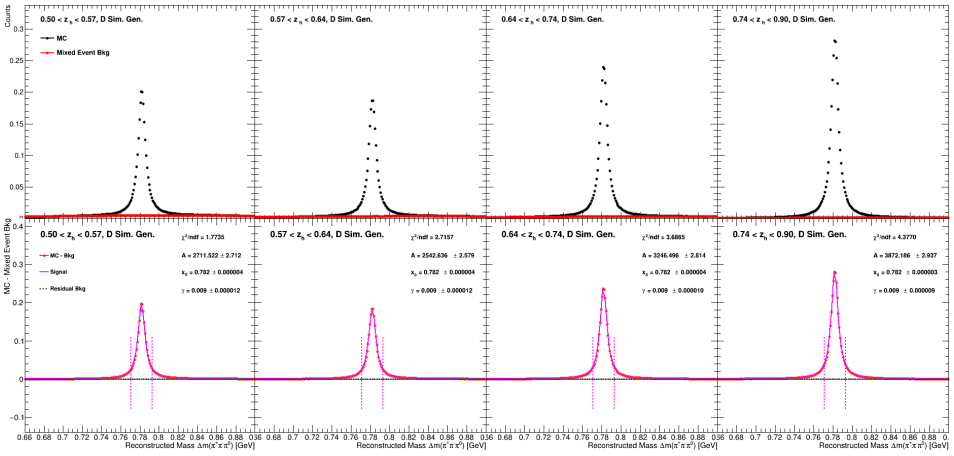

Figure A.43: Background subtraction through event-mixing on MC generated simulations of D, for each bin in z_h. A detailed explanation can be found at Sections 4.11.2 and A.2.

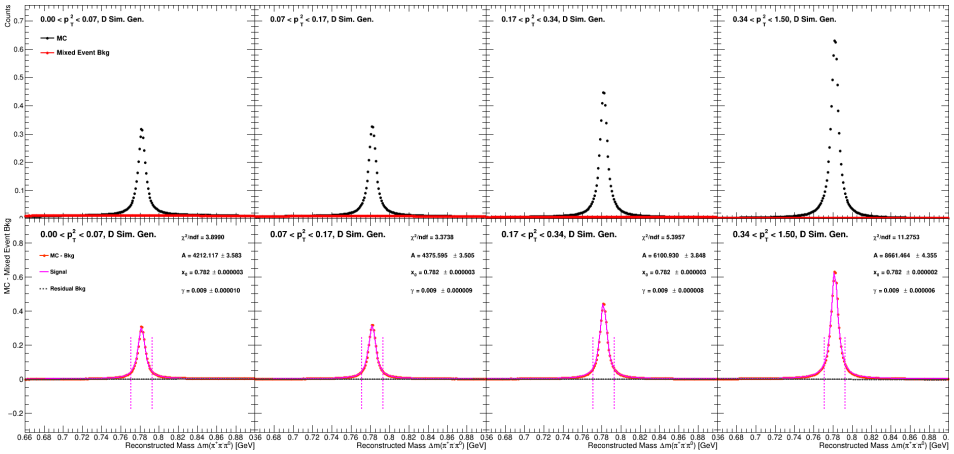

Figure A.44: Background subtraction through event-mixing on MC generated simulations of D, for each bin in p_T^2. A detailed explanation can be found at Sections 4.11.2 and A.2.

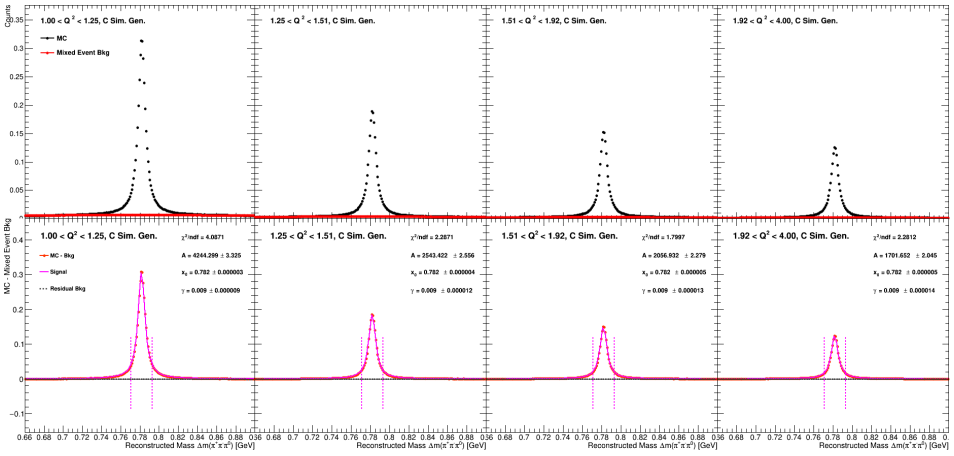

Figure A.45: Background subtraction through event-mixing on MC generated simulations of C, for each bin in Q^2. A detailed explanation can be found at Sections 4.11.2 and A.2.

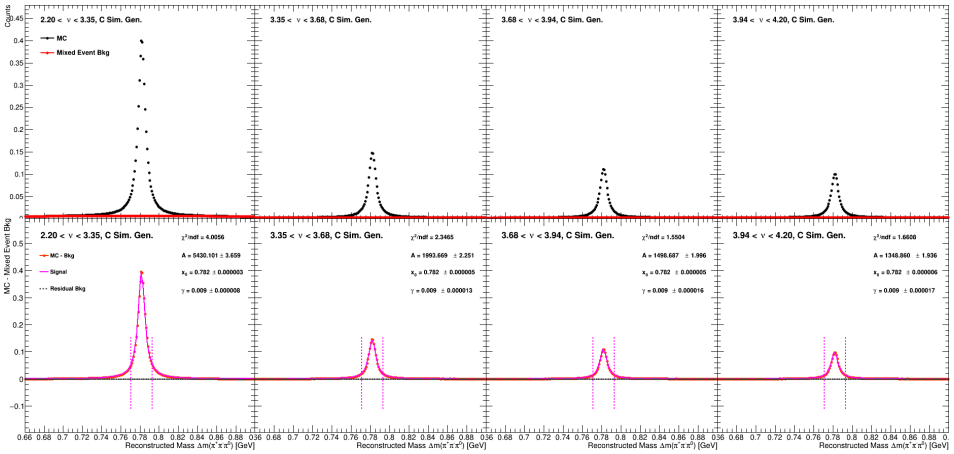

Figure A.46: Background subtraction through event-mixing on MC generated simulations of C, for each bin in ν. A detailed explanation can be found at Sections 4.11.2 and A.2.

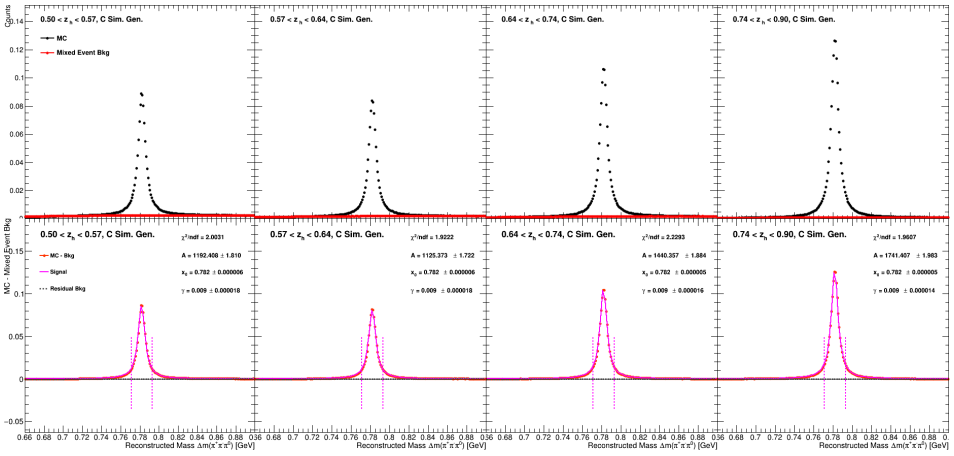

Figure A.47: Background subtraction through event-mixing on MC generated simulations of C, for each bin in z_h. A detailed explanation can be found at Sections 4.11.2 and A.2.

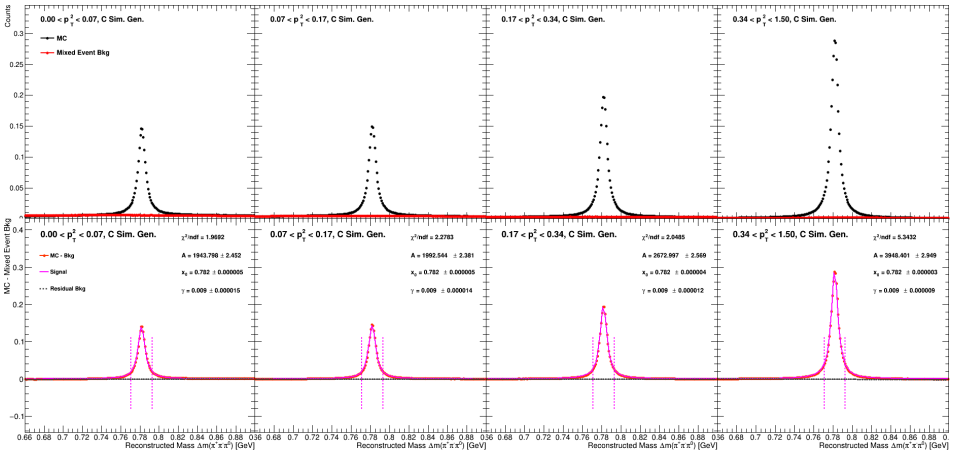

Figure A.48: Background subtraction through event-mixing on MC generated simulations of C, for each bin in p_T^2. A detailed explanation can be found at Sections 4.11.2 and A.2.

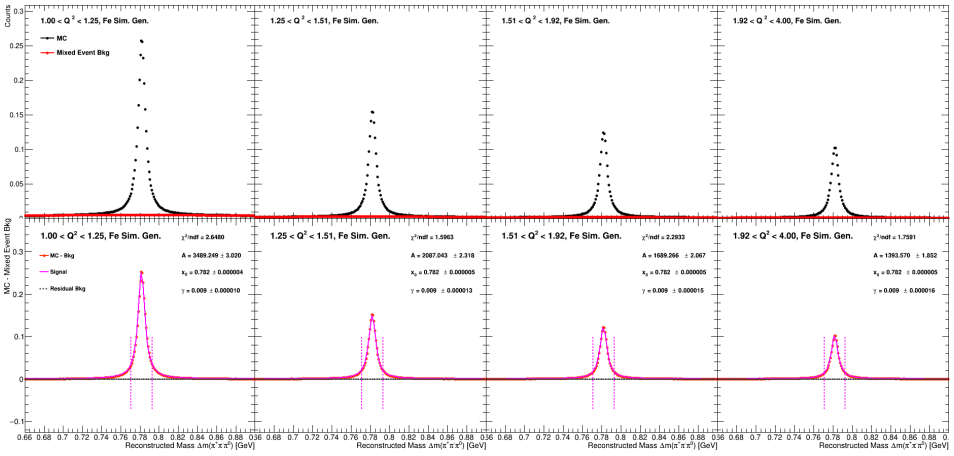

Figure A.49: Background subtraction through event-mixing on MC generated simulations of Fe, for each bin in Q^2. A detailed explanation can be found at Sections 4.11.2 and A.2.

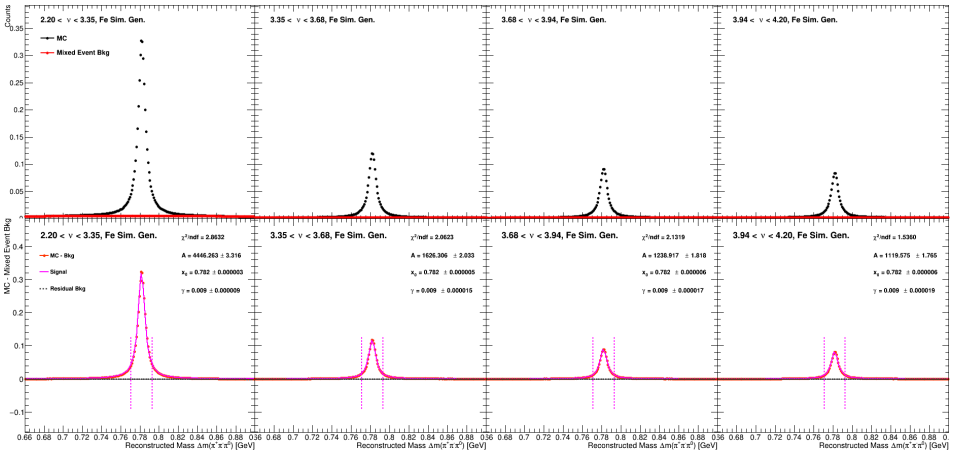

Figure A.50: Background subtraction through event-mixing on MC generated simulations of Fe, for each bin in ν. A detailed explanation can be found at Sections 4.11.2 and A.2.

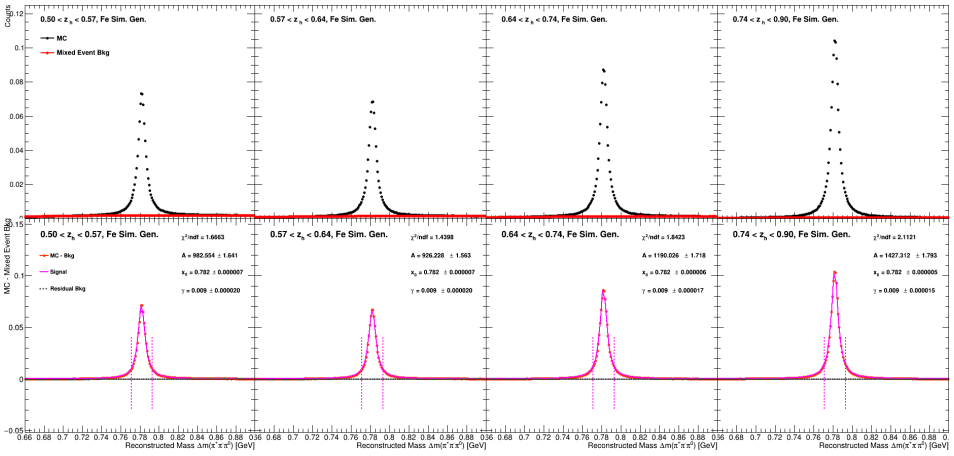

Figure A.51: Background subtraction through event-mixing on MC generated simulations of Fe, for each bin in z_h. A detailed explanation can be found at Sections 4.11.2 and A.2.

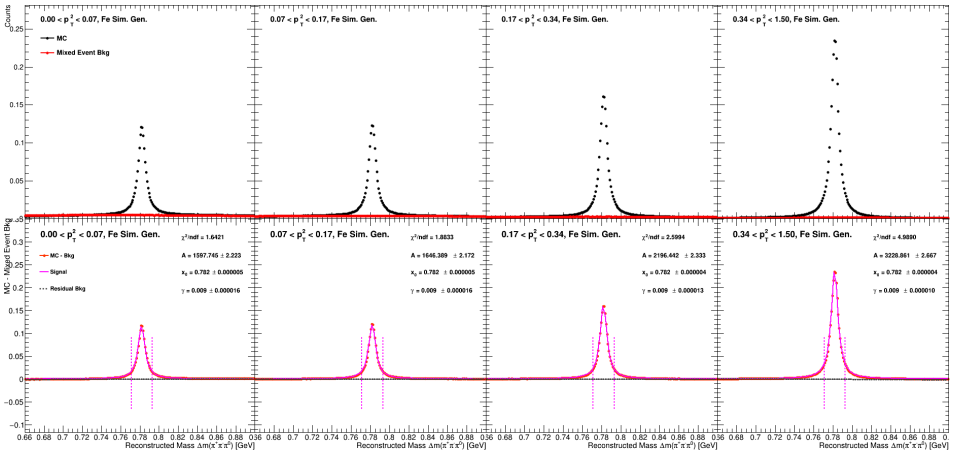

Figure A.52: Background subtraction through event-mixing on MC generated simulations of Fe, for each bin in p_T^2. A detailed explanation can be found at Sections 4.11.2 and A.2.

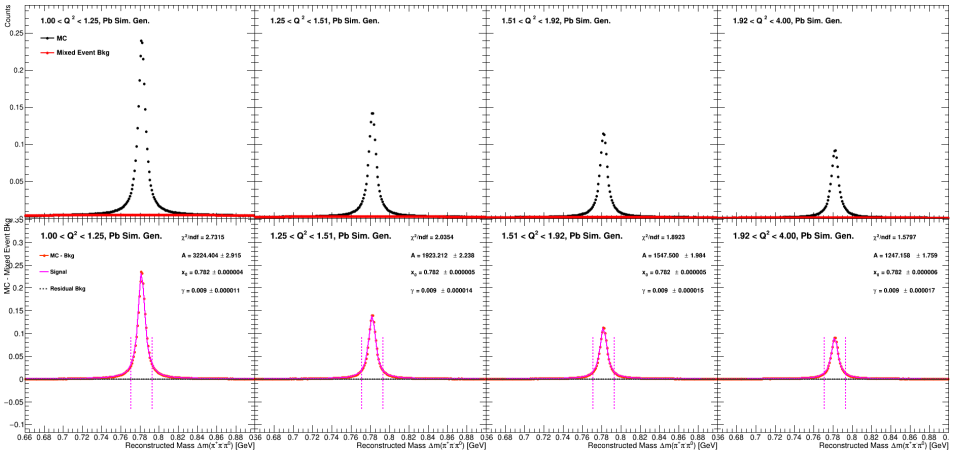

Figure A.53: Background subtraction through event-mixing on MC generated simulations of Pb, for each bin in Q^2. A detailed explanation can be found at Sections 4.11.2 and A.2.

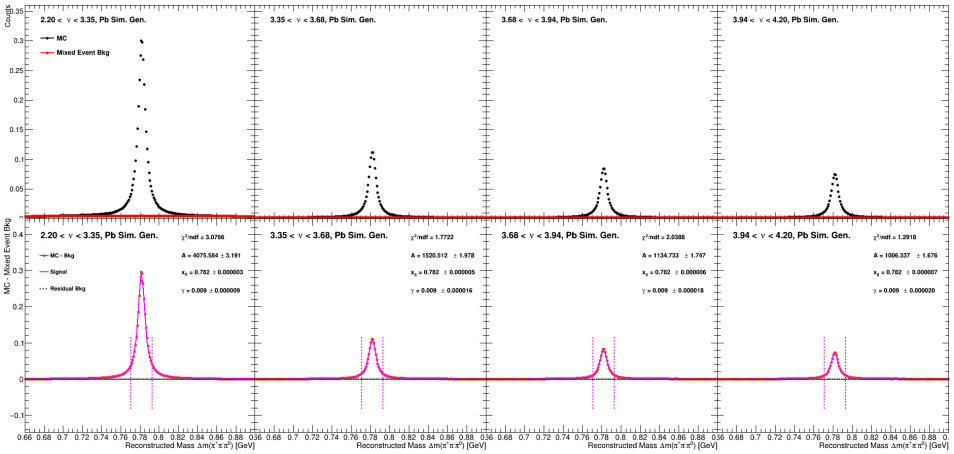

Figure A.54: Background subtraction through event-mixing on MC generated simulations of Pb, for each bin in ν. A detailed explanation can be found at Sections 4.11.2 and A.2.

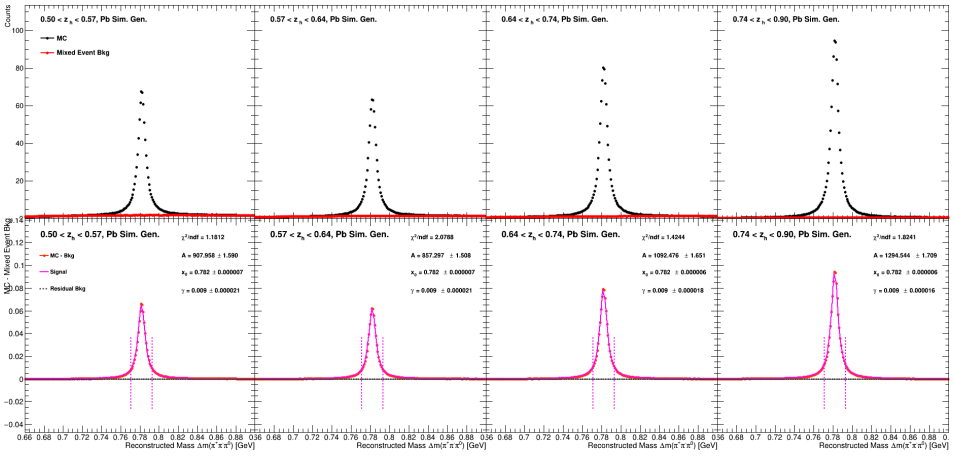

Figure A.55: Background subtraction through event-mixing on MC generated simulations of Pb, for each bin in z_h. A detailed explanation can be found at Sections 4.11.2 and A.2.

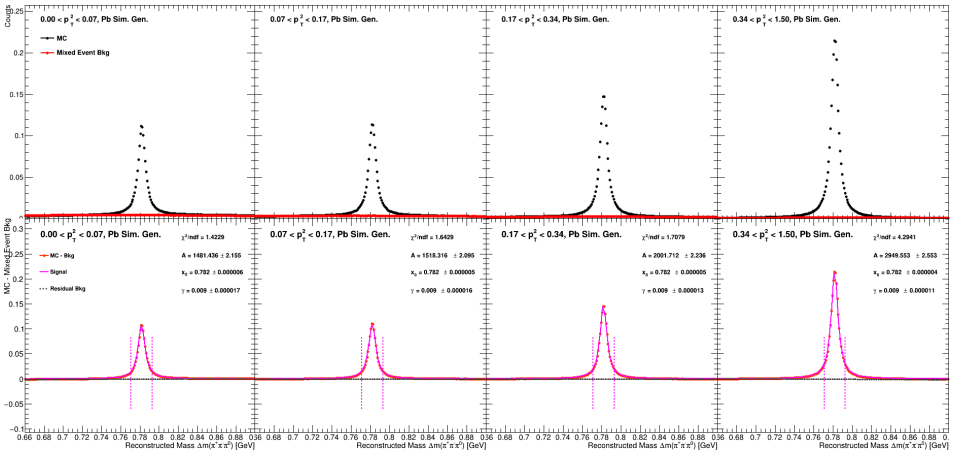

Figure A.56: Background subtraction through event-mixing on MC generated simulations of Pb, for each bin in p_T^2. A detailed explanation can be found at Sections 4.11.2 and A.2.

A.2.3 On Reconstructed Simulations

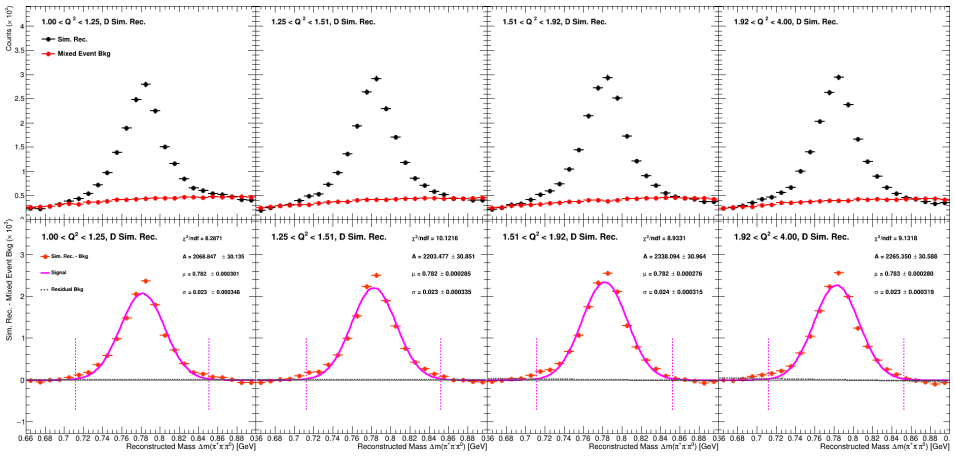

Figure A.57: Background subtraction through event-mixing on MC reconstructed simulations of D, for each bin in Q^2. A detailed explanation can be found at Sections 4.11.2 and A.2.

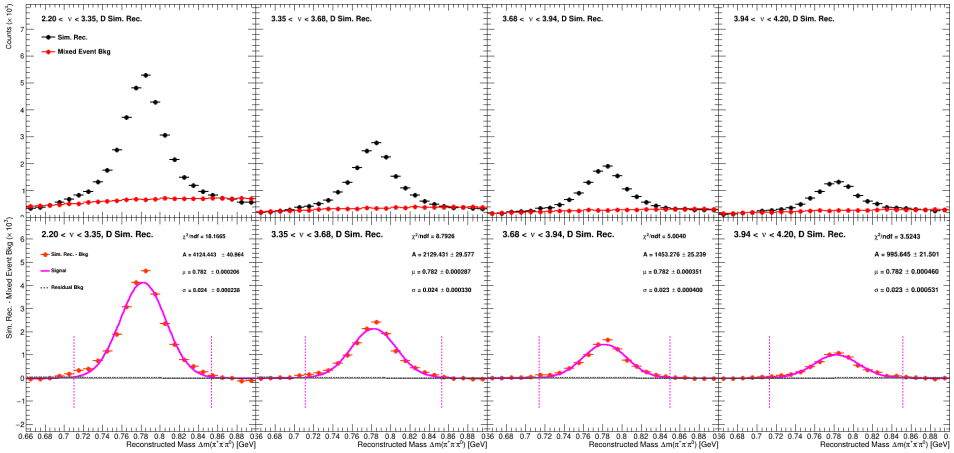

Figure A.58: Background subtraction through event-mixing on MC reconstructed simulations of D, for each bin in ν. A detailed explanation can be found at Sections 4.11.2 and A.2.

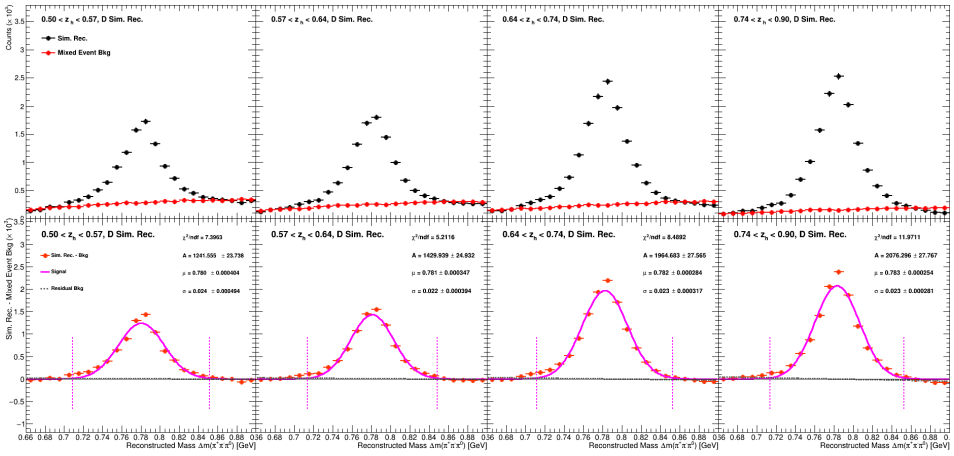

Figure A.59: Background subtraction through event-mixing on MC reconstructed simulations of D, for each bin in z_h. A detailed explanation can be found at Sections 4.11.2 and A.2.

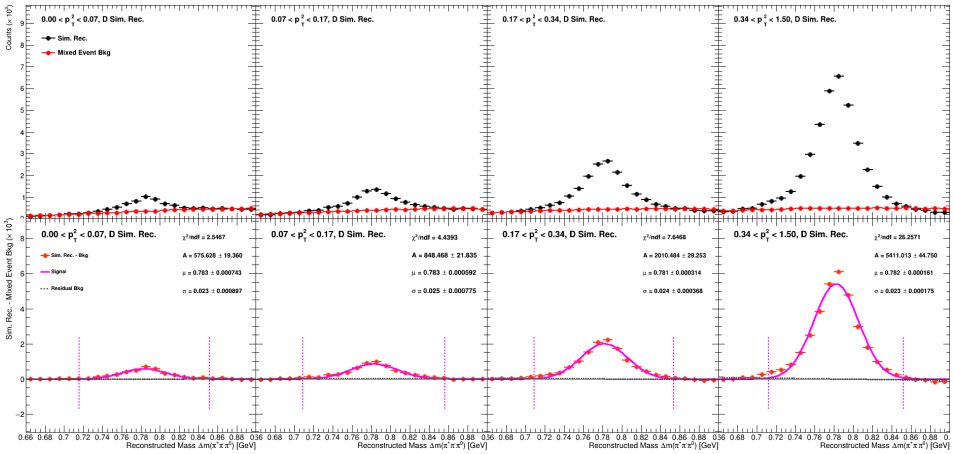

Figure A.60: Background subtraction through event-mixing on MC reconstructed simulations of D, for each bin in p_T^2. A detailed explanation can be found at Sections 4.11.2 and A.2.

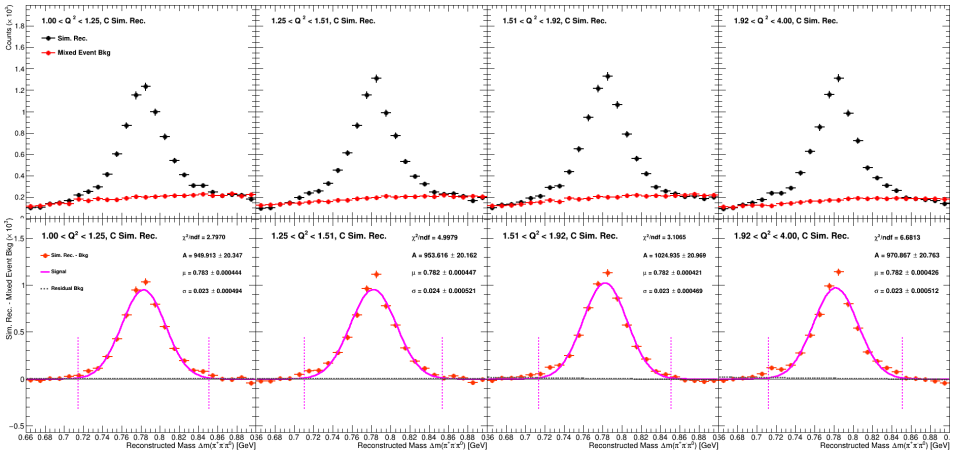

Figure A.61: Background subtraction through event-mixing on MC reconstructed simulations of C, for each bin in Q^2. A detailed explanation can be found at Sections 4.11.2 and A.2.

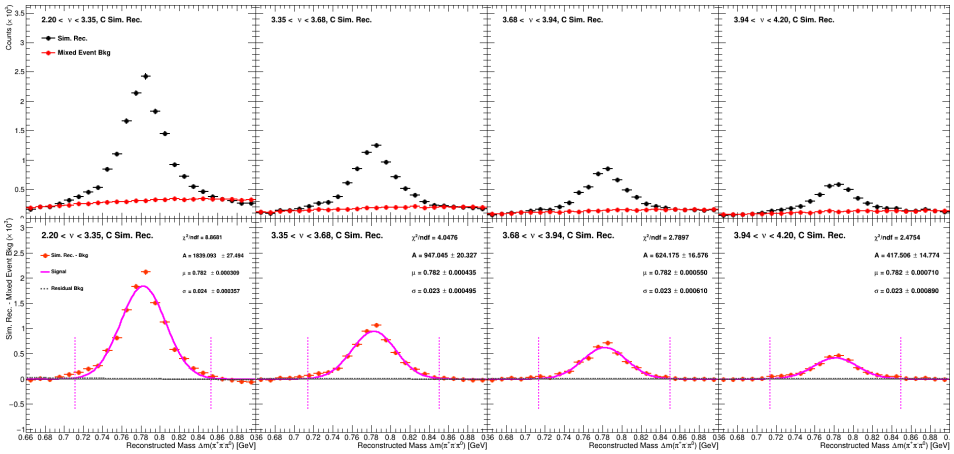

Figure A.62: Background subtraction through event-mixing on MC reconstructed simulations of C, for each bin in ν. A detailed explanation can be found at Sections 4.11.2 and A.2.

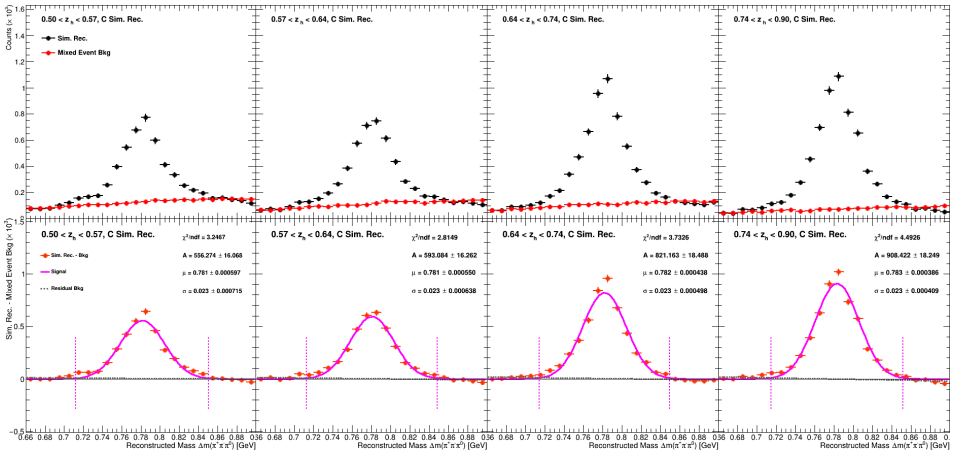

Figure A.63: Background subtraction through event-mixing on MC reconstructed simulations of C, for each bin in z_h. A detailed explanation can be found at Sections 4.11.2 and A.2.

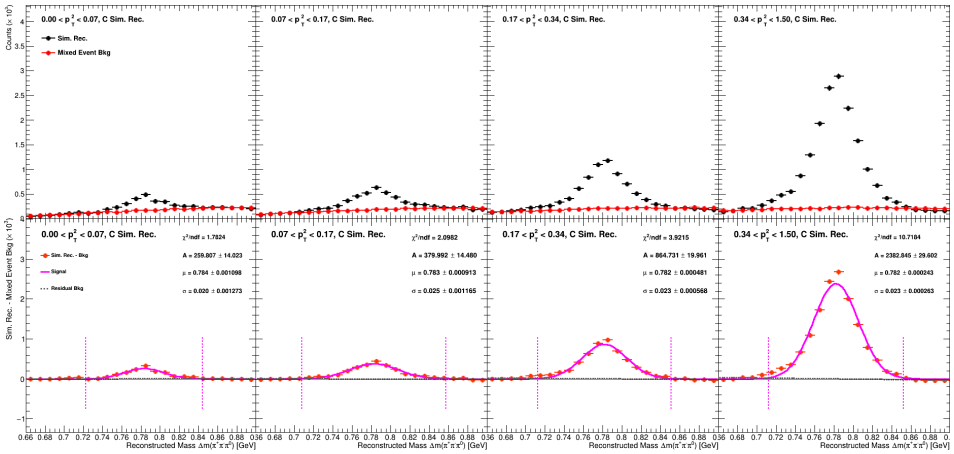

Figure A.64: Background subtraction through event-mixing on MC reconstructed simulations of C, for each bin in p_T^2. A detailed explanation can be found at Sections 4.11.2 and A.2.

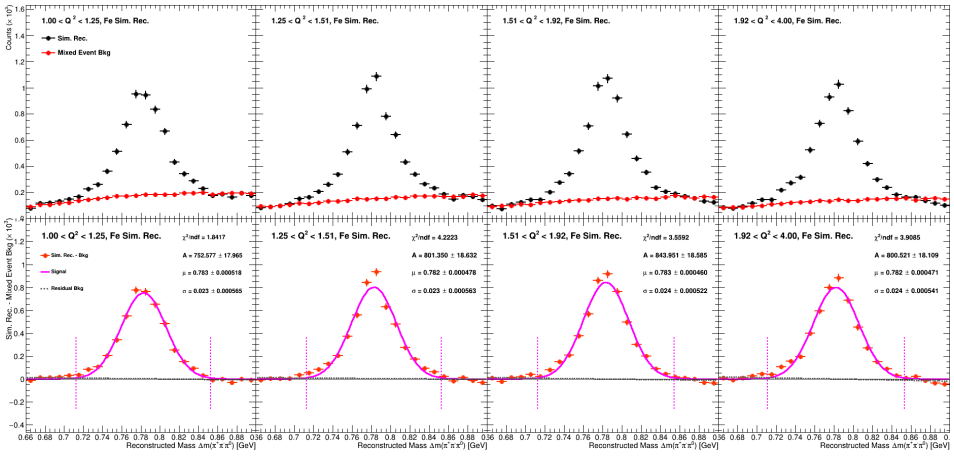

Figure A.65: Background subtraction through event-mixing on MC reconstructed simulations of Fe, for each bin in Q^2. A detailed explanation can be found at Sections 4.11.2 and A.2.

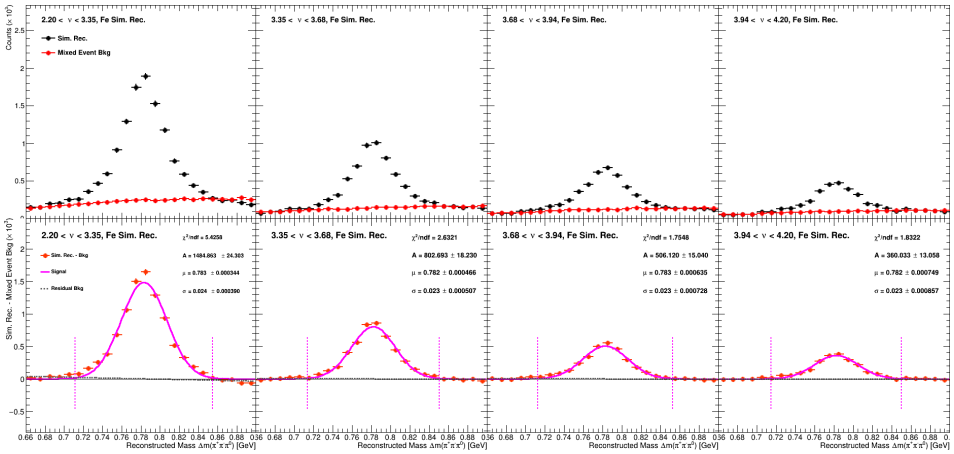

Figure A.66: Background subtraction through event-mixing on MC reconstructed simulations of Fe, for each bin in ν. A detailed explanation can be found at Sections 4.11.2 and A.2.

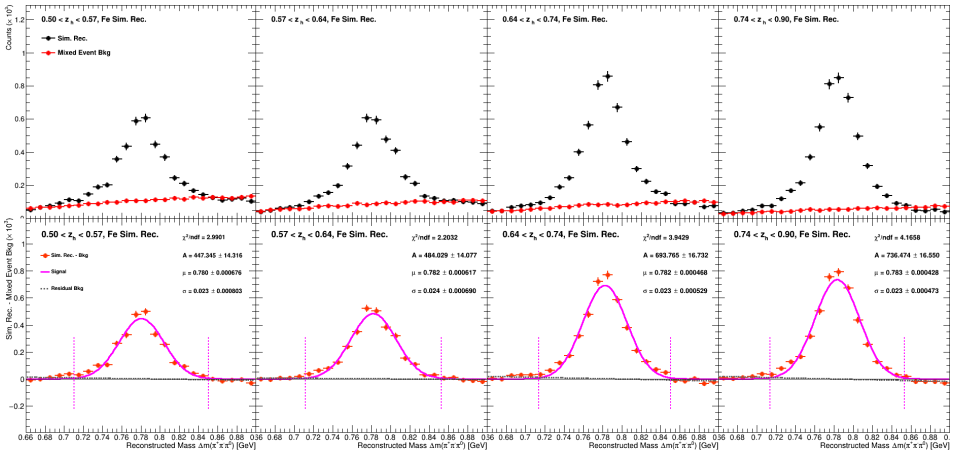

Figure A.67: Background subtraction through event-mixing on MC reconstructed simulations of Fe, for each bin in z_h. A detailed explanation can be found at Sections 4.11.2 and A.2.

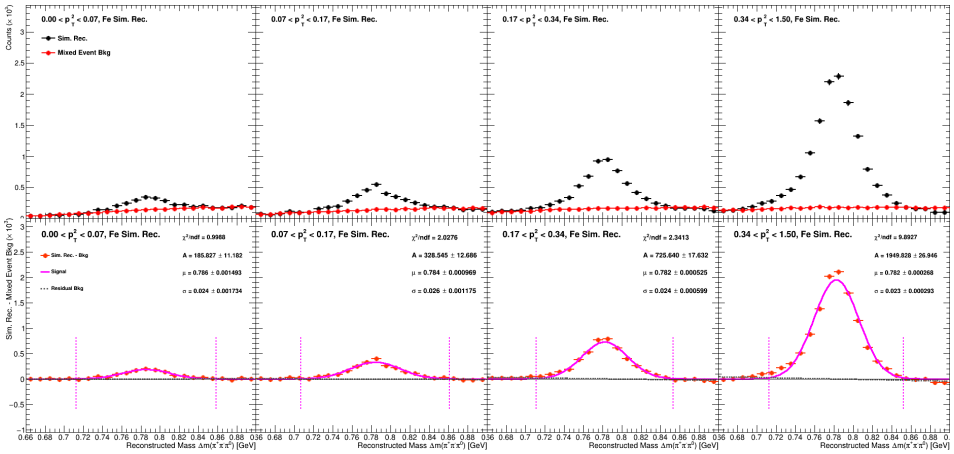

Figure A.68: Background subtraction through event-mixing on MC reconstructed simulations of Fe, for each bin in p_T^2. A detailed explanation can be found at Sections 4.11.2 and A.2.

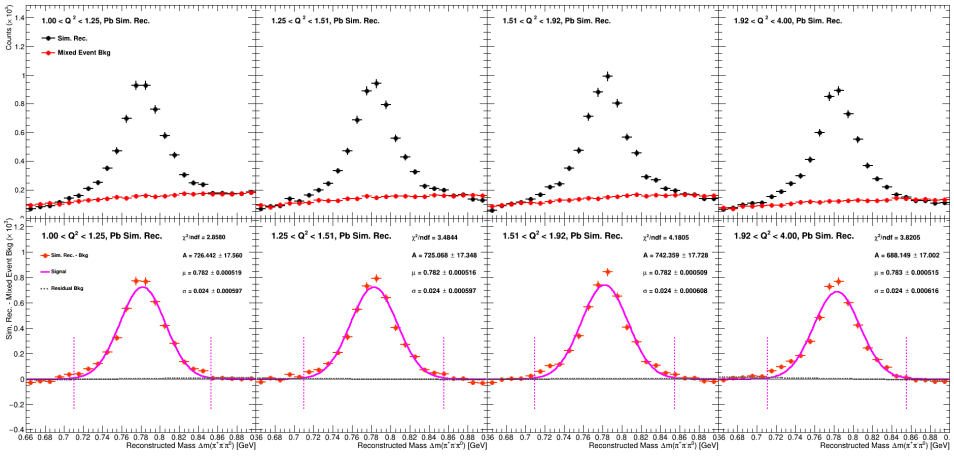

Figure A.69: Background subtraction through event-mixing on MC reconstructed simulations of Pb, for each bin in Q^2. A detailed explanation can be found at Sections 4.11.2 and A.2.

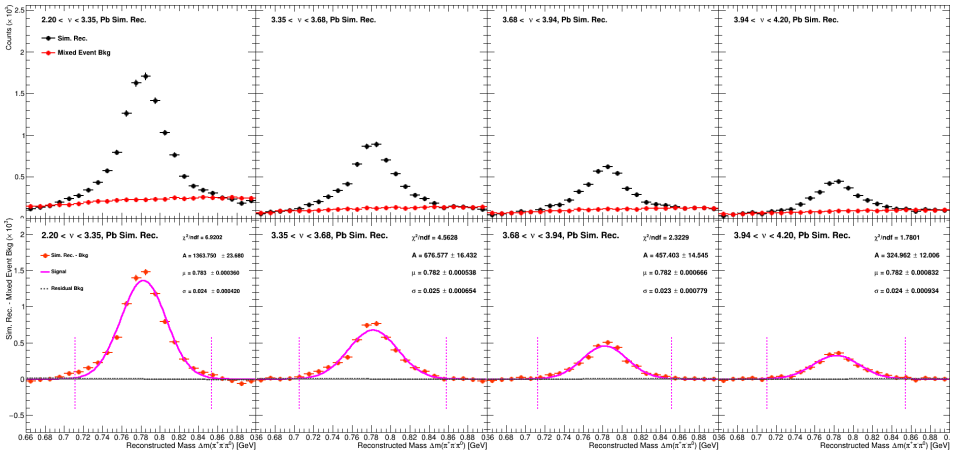

Figure A.70: Background subtraction through event-mixing on MC reconstructed simulations of Pb, for each bin in ν. A detailed explanation can be found at Sections 4.11.2 and A.2.

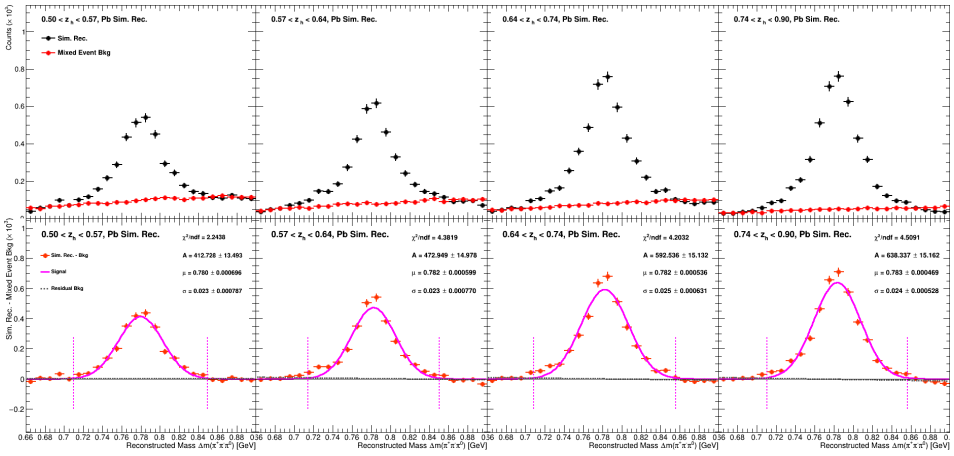

Figure A.71: Background subtraction through event-mixing on MC reconstructed simulations of Pb, for each bin in z_h. A detailed explanation can be found at Sections 4.11.2 and A.2.

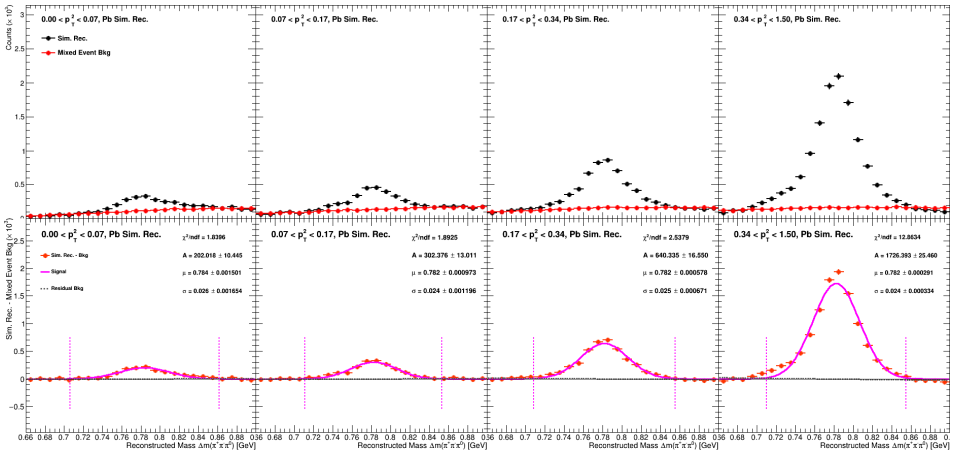

Figure A.72: Background subtraction through event-mixing on MC reconstructed simulations of Pb, for each bin in p_T^2. A detailed explanation can be found at Sections 4.11.2 and A.2.

LIST OF FIGURES

LIST OF TABLES

ACRONYMS

CLAS CEBAF Large Acceptance Spectrometer

CEBAF Continous Electron Beam Accelerator Facility

TJNAF Thomas Jefferson National Accelerator Facility

JLAB Jefferson Lab

DIS Deep-Inelastic Scattering

SIDIS Semi-Inclusive Deep-Inelastic Scattering

DC Drift Chambers

EC Electromagnetic Calorimeters

LAC Large-Angle Calorimeter

SC Scintillator Counters

CC Cherenkov Counters

TOF Time of Flight

QCD Quantum Chromodynamics

QED Quantum Electrodynamics

PDG Particle Data Group

HERMES HERA Measurements of Spin

SLAC Stanford Linear Accelerator Center

DESY Deutsches Elektronen-Synchrotron

LHC Large Hadron Collider

ATLAS A Toroidal LHC Apparatus

HEP High-Energy Physics

MC Monte Carlo

BOS Bank Object System

PMT Photomultiplier Tubes

EIC Electron-Ion Collider

CERN European Organization for Nuclear Research

MR Multiplicity Ratio

EMC European Muon Collaboration

RF Radio-Frequency

E665 Experiment-665 of Fermilab

PDFs Parton Distribution Functions

DAQ Data Acquisition System

CHL Central Helium Liquefier

PID Particle Identification

QPM Quark-Parton Model

CDF Collider Detector at Fermilab

BNL Brookhaven National Laboratory

BIBLIOGRAPHY

[1] P. Higgs. "Broken Symmetries and the Masses of Gauge Bosons." In: *Phys. Rev. Lett.* 13 (1964), p. 508. DOI: 10.1103/PhysRevLett.13.508.

[2] ATLAS Collaboration (G. Add *et al.*) "Observation of a new particle in the search for the Standard Model Higgs boson with the ATLAS detector at the LHC." In: *Phys. Lett. B* 716 (2012), pp. 1–29. DOI: 10.1016/j.physletb.2012.08.020.

[3] CMS Collaboration (S. Chatrchyan *et al.*) "Observation of a new boson at a mass of 125 GeV with the CMS experiment at the LHC." In: *Phys. Lett. B* 716 (2012), pp. 30–61. DOI: 10.1016/j.physletb.2012.08.021.

[4] SLAC Collaboration (L. S. Osborne *et al.*) "Electroproduction of Hadrons from Nuclei." In: *Phys. Rev. Lett.* 40 (1978), p. 1624. DOI: 10.1103/PhysRevLett.40.1624.

[5] EMC Collaboration (J. Ashman *et al.*) "Comparison of forward hadrons produced in muon interactions on nuclear targets and deuterium." In: *Z. Phys. C - Particles and Fields* 52 (1991), pp. 1–11. DOI: 10.1007/BF01412322.

[6] M. R. Adams *et al.* "Scaled energy (z) distributions of charged hadrons observed in deep-inelastic muon scattering at 490 GeV from xenon and deuterium targets." In: *Phys. Rev. D* 50 (1994), p. 1836. DOI: 10.1103/PhysRevD.50.1836.

[7] HERMES Collaboration (A. Airapetian *et al.*) "Hadron formation in deep-inelastic positron scattering in a nuclear environment." In: *Eur. Phys. J. C* 20 (2001), pp. 479–486. DOI: 10.1007/s100520100697.

[8] HERMES Collaboration (A. Airapetian *et al.*) "Quark fragmentation to $\pi^{\pm}$, π^{0}, $K^{\pm}$, p and $\bar{p}$ in the nuclear environment." In: *Phys. Lett. B* 577 (2003), pp. 37–46. DOI: 10.1016/j.physletb.2003.10.026.

[9] HERMES Collaboration (A. Airapetian *et al.*) "Hadronization in semi-inclusive deep-inelastic scattering on nuclei." In: *Nucl. Phys. B* 780 (2007), pp. 1–27. DOI: 10.1016/j.nuclphysb.2007.06.004.

[10] HERMES Collaboration (A. Airapetian *et al.*) "Transverse momentum broadening of hadrons produced in semi-inclusive deep-inelastic scattering on nuclei." In: *Phys. Lett. B* 684 (2010), pp. 114–118. DOI: 10.1016/j.physletb.2010.01.020.

[11] HERMES Collaboration (A. Airapetian *et al.*) "Multidimensional study of hadronization in nuclei." In: *Eur. Phys. J. A* 47 (2011), p. 113. DOI: 10.1140/epja/i2011-11113-5.

[12] CLAS Collaboration. "The CEBAF Large Acceptance Spectrometer (CLAS)." In: *Nucl. Instr. and Meth. A* 504 (2003), pp. 513–553. DOI: 10.1016/S0168-9002(03)01001-5.

[13] H. Hakobyan *et al*. "A double-target system for precision measurements of nuclear medium effects." In: *Nucl. Instr. and Meth. A* 592 (2008), pp. 218–223. DOI: 10.1016/j.nima.2008.04.055.

[14] CLAS Collaboration (A. Daniel *et al.*) "Measurement of the nuclear multiplicity ratio for K^0_s hadronization at CLAS." In: *Phys. Lett. B* 706 (2011), p. 26. DOI: 26-31.

[15] H. Hakobyan. "Observation of Quark Propagation Pattern in Nuclear Medium." PhD thesis. Yerevan State University, 2008.

[16] R. Dupré. "Quark Fragmentation and Hadron Formation in Nuclear Matter." PhD thesis. Université de Lyon, 2011.

[17] S. Morán. "Study of Hadronization process for positive pions with CLAS detector." MA thesis. Universidad Técnica Federico Santa María, 2021.

[18] S. Morán *et al*. "Charged-pion multiplicity ratio measurement with EG2 data." CLAS Analysis Note. 2021.

[19] T. Mineeva. "Hadronization Studies via π^0 Electroproduction off D, C, Fe, and Pb." PhD thesis. University of Connecticut, 2013.

[20] T. Mineeva. "Neutral Pion Multiplicity Ratios from SIDIS Lepton-nuclear Scattering." CLAS Analysis Note. 2020.

[21] O. Soto. "Hadronization Studies of eta mesons using the CLAS spectrometer." PhD thesis. Universidad Técnica Federico Santa María, 2018.

[22] Particle Data Group (P. A. Zyla *et al.*) "Review of Particle Physics." In: *Prog. Theor. Exp. Phys.* 2020 (2020). 083C01. DOI: 10.1093/ptep/ptaa104.

[23] V.E. Barnes *et al*. "Observation of a Hyperon with Strangeness Minus Three." In: *Phys. Rev. Lett.* 12 (1964), p. 204. DOI: doi.org/10.1103/PhysRevLett.12.204.

[24] A. De Angelis and M. Pimenta. *Introduction to Particle and Astroparticle Physics*. Springer Nature 2018, 2018. DOI: 10.1007/978-3-319-78181-5.

[25] J. Friedman and H. Kendall. "Deep Inelastic Electron Scattering." In: *Annu. Rev. Nucl. Sci.* 22 (1972), pp. 203–254. DOI: 10.1146/annurev.ns.22.120172.001223.

[26] Y.L. Dokshitzer. "Calculation of structure functions of deep-inelastic scattering and e^+e^- annihilation by perturbation theory in quantum chromodynamics." In: *Sov. Phys. JETP* 46 (1977), pp. 641–653.

[27] V.N. Gribov and L.N. Lipatov. "Deep inelastic *ep* scattering in perturbation theory." In: *Sov. J. Nucl. Phys.* 15 (1972), pp. 438–450.

[28] G. Altarelli and G. Parisi. "Asymptotic freedom in parton language." In: *Nucl. Phys. B* 126 (1977), pp. 298–318. DOI: 10.1016/0550-3213(77)90384-4.

[29] F. Halzen and A. D. Martin. *Quarks and Leptons*. John Wiley & Sons, 1984.

[30] B. Kopeliovich *et al.* "Nuclear hadronization: within or without?" In: *Nucl. Phys. A* 740 (2004), pp. 211–245. DOI: 10.1016/j.nuclphysa.2004.04.110.

[31] B. Kopeliovich *et al.* "Time Evolution of Jets and Perturbative Color Neutralization." In: *Nucl. Phys. A* 782 (2007), pp. 224–233. DOI: 10.1016/j.nuclphysa.2006.10.059.

[32] B. Andersson. *The Lund Model*. Cambridge University Press, 1998.

[33] T. Sjöstrand. "High-energy-physics event generation with PYTHIA 5.7 and JETSET 7.4." In: *Comput. Phys. Commun.* 82 (1994), p. 74. DOI: 10.1016/0010-4655(94)90132-5.

[34] D. Amati and G. Veneziano. "Preconfinement as a property of perturbative QCD." In: *Phys. Lett. B* 83 (1979), p. 87. DOI: 10.1016/0370-2693(79)90896-7.

[35] J. Bellm *et al.* "HERWIG 7.0/HERWIG++ 3.0 release note." In: *Eur. Phys. J. C* 76 (2016), p. 196. DOI: 10.1140/epjc/s10052-016-4018-8.

[36] A. Bialas and T. Chmaj. "Leptoproduction of hadrons from nuclear targets and fragmentation of quarks into hadrons." In: *Phys. Lett. B* 133 (1983), pp. 241–244. DOI: 10.1016/0370-2693(83)90569-5.

[37] EMC Collaboration (J. Aubert *et al.*) "The ratio of the nucleon structure functions F_2^N for iron and deuterium." In: *Phys. Lett. B* 123 (1983), pp. 275–278. DOI: 10.1016/0370-2693(83)90437-9.

[38] C. Leemann, D. Douglas, and G. Krafft. "The Continuouts Electron Beam Accelerator Facility: CEBAF at the Jefferson Laboratory." In: *Annu. Rev. Nucl. Part. Sci.* 51 (2001), pp. 513–540. DOI: 10.1146/annurev.nucl.51.101701.132327.

[39] CLAS Collaboration (M.D. Mestayer *et al.*) "The CLAS drift chamber system." In: *Nucl. Inst. and Meth. A* 449 (2000), pp. 81–111. DOI: 10.1016/S0168-9002(00)00151-0.

[40] CLAS Collaboration (G. Adams *et al.*) "The CLAS Cherenkov detector." In: *Nucl. Inst. and Meth. A* 465 (2001), pp. 414–427. DOI: 10.1016/S0168-9002(00)01313-9.

[41] CLAS Collaboration (E.S. Smith *et al.*) "The time-of-flight system for CLAS." In: *Nucl. Inst. and Meth. A* 432 (1999), pp. 265–298. DOI: 10.1016/S0168-9002(99)00484-2.

[42] CLAS Collaboration (M. Amarian *et al.*) "The CLAS forward electromagnetic calorimeter." In: *Nucl. Inst. and Meth. A* 460 (2001), pp. 239–265. DOI: 10.1016/S0168-9002(00)00996-7.

[43] CLAS Collaboration (M. Anghinolfi *et al.*) "The CLAS electromagnetic calorimeter at large angles." In: *Nucl. Inst. and Meth. A* 537 (2005), pp. 562–570. DOI: 10.1016/j.nima.2004.08.070.

[44] W. Brooks *et al.* "Quark Propagation Through Cold QCD Matter." CLAS Proposal E-02-104. 2002.

[45] K. Hafidi *et al.* "Q^2 Dependence of Nuclear Transparency for Incoherent ρ^0 Electroproduction." CLAS Proposal E-02-110. 2002.

[46] A. El Alaoui. *Hadronization Analysis using EG2 data*. URL: https://userweb.jlab.org/~ahmede/hadro_webpage/.

[47] G.P. Gilfoyle *et al.* "Online RECSIS." CLAS-NOTE 98-017. 1998.

[48] S. Stepanyan. "Simple Event Builder in the framework of RECSIS." CLAS Draft. 1997.

[49] L. Zana. "Search for the onset of Color Transparency through ρ^0 Electroproduction on Nuclei." PhD thesis. University of New Hampshire, 2010.

[50] H. Egiyan. "Single π^+ Electroproduction in the First and Second Resonance Regions using CLAS." PhD thesis. College of William & Mary, 2001.

[51] R. Brun and F. Rademakers. "ROOT - An object oriented data analysis framework." In: *Nucl. Inst. and Meth. A* 389 (1997), pp. 81–86. DOI: 10.1016/S0168-9002(97)00048-X.

[52] L.I. Schiff. "Radiative Correction to the Angular Distribution of Nuclear Recoils from Electron Scattering." In: *Phys. Rev.* 87 (1952), pp. 750–752. DOI: 10.1103/PhysRev.87.750.

[53] ATLAS Collaboration (G. Aad *et al.*) "Measurement of $D^{*\pm}$ meson production in jets from pp collisions at $\sqrt{s} = 7$ TeV with the ATLAS detector." In: *Phys. Rev. D* 85 (2012), p. 052005. DOI: 10.1103/PhysRevD.85.052005.

[54] ATLAS Collaboration (G. Aad *et al.*) "Measurement of the b-hadron production cross section using decays to $D^{*\pm}\mu^{-}X$ final states in pp collisions at $\sqrt{s} = 7$ TeV with the ATLAS detector." In: *Nucl. Phys. B* 864 (2012), pp. 341–381. DOI: 10.1016/j.nuclphysb.2012.07.009.

[55] A. Chisholm. "Measurements of the χ_c and χ_b Quarkonium States in pp Collisions with the ATLAS Experiment." PhD thesis. University of Birmingham, 2014.

[56] F. Jonas. "Measurement of ω and η mesons via their three pion decay with ALICE in pp collisions at $\sqrt{s} = 7$ TeV." MA thesis. University of Münster, 2018.

[57] W. Verkerke and D. Kirkby. "The RooFit toolkit for data modeling." In: *Statistical Problems in Particle Physics, Astrophysics and Cosmology*, pp. 186–189. DOI: 10.1142/9781860948985_0039.

[58] P. R. Bevington and D. K. Robinson. *Data Reduction and Error Analysis*. McGraw-Hill Education, 2002.

[59] FOCUS Collaboration (J.M. Link *et al.*) "Measurement of masses and widths of excited charm mesons D_2^* and evidence for broad states." In: *Phys. Lett. B* 586 (2004), pp. 11–20. DOI: 10.1016/j.physletb.2004.02.017.

[60] E791 Collaboration (E.M. Aitala *et al.*) "Dalitz Plot Analysis of the Decay $D^+ \to K^-\pi^+\pi^+$ and Indication of a Low-Mass Scalar $K\pi$ Resonance." In: *Phys. Rev. Lett.* 89 (2002), p. 121801. DOI: 10.1103/PhysRevLett.89.121801.

[61] F. James. "Minuit Function Minimization and Error Analysis: Reference Manual Version 94.1." CERN-D-506. 1994.

[62] G. I. Kopylov. "Like particle correlations as a tool to study the multiple production mechanism." In: *Phys. Lett. B* 50-4 (1974), pp. 472–474. DOI: 10.1016/0370-2693(74)90263-9.

[63] G. Ingelman *et al.* "Lepto 6.5 - A Monte Carlo generator for deep inelastic lepton-nucleon scattering." In: *Comp. Phys. Comm.* 101 (1997), pp. 108–134. DOI: 10.1016/S0010-4655(96)00157-9.

[64] L. Lönnblad. "Ariadne version 4 – A program for simulation of QCD cascades implementing the colour dipole model." In: *Comput. Phys. Commun.* 71 (1992), pp. 15–31. DOI: 10.1016/0010-4655(92)90068-A.

[65] J. Botts *et al.* "CTEQ parton distributions and flavor dependence of sea quarks." In: *Phys. Lett. B* 304 (1993), pp. 159–166. DOI: 10.1016/0370-2693(93)91416-K.

[66] R. Brun *et al.* "GEANT 3: user's guide GEANT 3.10, GEANT 3.11." CERN-DD-EE-84-01. 1987.

[67] H. Hakobyan. "The CLAS/EG2 target implementation in GSIM." CLAS-NOTE 2008-002. 2007.

[68] D. Jenkins. "A Comparison of Simple and Full Acceptance." CLAS-NOTE 2004-043. 2004.

[69] J. W. Cronin *et al.* "Production of hadrons at large transverse momentum at 200, 300, and 400 GeV." In: *Phys. Rev. D* 11 (1975), p. 3105. DOI: 10.1103/PhysRevD.11.3105.

[70] A. Aste *et al.* "Coulomb distortion of relativistic electrons in the nuclear electrostatic field." In: *Eur. Phys. J. A* 26 (2005), pp. 167–178. DOI: 10.1140/epja/i2005-10169-0.

[71] L. Mo and Y. Tsai. "Radiative corrections to elastic and inelastic ep and μp scattering." In: *Rev. Mod. Phys.* 41 (1969), pp. 205–235. DOI: 10.1103/RevModPhys.41.205.

[72] I. Akushevich *et al.* "Radiative effects in the processes of hadron electroproduction." In: *Eur. Phys. J. C* 10 (1999), pp. 681–687. DOI: 10.1007/s100529900172.

[73] CLAS Collaboration (V.D. Burkert *et al.*) "The CLAS12 spectrometer at Jefferson laboratory." In: *Nucl. Inst. and Meth. A* 959 (2020), p. 163419. DOI: 10.1016/j.nima.2020.163419.

[74] A. Accardi *et al.* "Electron-Ion Collider: The Next QCD Frontier." In: *Eur. Phys. J. A* 52 (2016), p. 268. DOI: 10.1140/epja/i2016-16268-9.

COLOPHON

This document was typeset using the typographical look-and-feel `classicthesis` developed by André Miede and Ivo Pletikosić. The style was inspired by Robert Bringhurst's seminal book on typography *"The Elements of Typographic Style"*. `classicthesis` is available for LaTeX :

https://bitbucket.org/amiede/classicthesis/